

POLITECNICO DI TORINO

Master of Science in Aerospace Engineering

Master's Degree Thesis

**Investigation of performance and
surge behavior of centrifugal
compressors through CFD
simulations**



Supervisors

prof. Henrik Alfredsson

prof. Lorenzo Casalino

Candidate

Francesco Tosto

Internship supervisor

Olle Bodin (Scania CV AB)

March 2018

Abstract

The use of turbocharged Diesel engines is nowadays a widespread practice in the automotive sector: heavy-duty vehicles like trucks or buses, in particular, are often equipped with turbocharged engines. An accurate study of the flow field developing inside both the main components of a turbocharger, i.e. compressor and turbine, is therefore necessary: the synergistic use of CFD simulations and experimental tests allows to fulfill this requirement.

The aim of this thesis is to investigate the performance and the flow field that develops inside a centrifugal compressor for automotive turbochargers. The study is carried out by means of numerical simulations, both steady-state and transient, based on RANS models (Reynolds Averaged Navier-Stokes equations). The code utilized for the numerical simulations is Ansys CFX.

The first part of the work is an engineering attempt to develop a CFD method for predicting the performance of a centrifugal compressor which is based solely on steady-state RANS models. The results obtained are then compared with experimental observations. The study continues with an analysis of the sensitivity of the developed CFD method to different parameters: influence of both position and model used for the rotor-stator interfaces and the axial tip-clearance on the global performances is studied and quantified.

In the second part, a design optimization study based on the Design of Experiments (DoE) approach is performed. In detail, transient RANS simulations are used to identify which geometry of the recirculation cavity hollowed inside the compressor shroud (ported shroud design) allows to mitigate the backflow that appears at low mass-flow rates. Backflow can be observed when the operational point of the compressor is suddenly moved from design to surge conditions. On actual heavy-duty vehicles, these conditions may arise when a rapid gear shift is performed.

Keywords: centrifugal compressor, Computational Fluid Dynamics (CFD), RANS, surge, compressible fluid dynamics, Design of Experiments (DoE).

Sommario

La sovralimentazione dei motori Diesel mediante turbocompressori è una pratica diffusa al giorno d'oggi in ambito automotive: veicoli pesanti quali autocarri o autobus, in particolare, sono spesso equipaggiati con motori turbocompressi. Un accurato studio del flusso che si sviluppa all'interno di entrambe le principali componenti di un turbocompressore, cioè compressore e turbina, è dunque necessario: l'utilizzo sinergico di simulazioni CFD e prove sperimentali consente di adempiere a questo requisito.

Lo scopo di questa tesi riguarda l'investigazione delle performance e del campo fluidodinamico che si sviluppa all'interno di un compressore centrifugo per turbocompressori automobilistici. Lo studio è stato condotto mediante simulazioni numeriche, sia steady-state che transienti, basate su modelli RANS (Reynolds Averaged Navier-Stokes equations). Il codice utilizzato per le simulazioni è Ansys CFX.

La prima parte del lavoro è incentrata sullo sviluppo di un modello CFD basato su modelli RANS steady-state per la predizione delle performance di un compressore centrifugo. I risultati ottenuti sono poi comparati con osservazioni sperimentali. Lo studio prosegue con un'analisi sulla sensibilità del modello CFD a diversi parametri: l'influenza della posizione e del modello utilizzato per le interfacce rotore-statore e della axial tip-clearance sulle performance globali è studiata e quantificata.

Nella seconda parte, invece, viene effettuato uno studio di ottimizzazione del design basato sull'approccio Design of Experiments (DoE). Nel dettaglio, simulazioni RANS transienti vengono adoperate per individuare quale geometria della cavità di ricircolazione ricavata all'interno dello shroud del compressore (ported shroud design) consente di mitigare gli effetti del riflusso che appare ogni qual volta il funzionamento del compressore viene spostato repentinamente da condizioni di progetto a condizioni di pompaggio. Tali condizioni possono insorgere quando si effettua un rapido cambio di marcia su veicoli pesanti dotati di motori turbocompressi.

Keywords: compressore centrifugo, Computational Fluid Dynamics (CFD), RANS, pompaggio, fluidodinamica compressibile, Design of Experiments (DoE).

Acknowledgements

First of all, I would like to thank my academic supervisor, prof. Henrik Alfredsson, for having given me the opportunity to carry on the thesis project in Scania CV AB and for the useful advices about the writing of the report.

A special thank goes to my industrial supervisor, Olle Bodin, for its availability and for having guided me during the five months of work. Thanks also to Thomas Svensson and Nicholas Anton for having shared with me their experience on Ansys CFX and turbochinery flows and for all the fruitful discussions.

To the NMGD and NXPS groups, for having included me and the enjoyable work environment.

Grazie di cuore Mamma, Papà ed Erica per aver sempre creduto in me ed avermi sostenuto anche nei momenti più difficili.

Torino, March 2018



Francesco Tosto

*In memory of
Giulio Regeni*

Contents

| | |
|--|------|
| Acknowledgements | VII |
| List of Figures | XV |
| List of Tables | XVII |
| List of Symbols | XIX |
| 1 Introduction | 1 |
| 1.1 Internal combustion engines | 2 |
| 1.1.1 Performance and turbochargers | 4 |
| 1.2 Computational Fluid Dynamics (CFD) | 6 |
| 1.3 Thesis objectives | 7 |
| 2 Centrifugal compressors | 9 |
| 2.1 Components | 10 |
| 2.1.1 Inlet | 11 |
| 2.1.2 Impeller | 11 |
| 2.1.3 Diffuser | 13 |
| 2.1.4 Volute | 14 |
| 2.2 Performance | 14 |
| 2.2.1 Compressor map | 17 |
| 2.3 Compressor aerodynamics | 18 |
| 2.3.1 Impeller flow field | 20 |
| 2.3.2 Vaneless diffuser flow field | 24 |
| 2.3.3 Volute flow field | 25 |
| 2.4 Losses | 25 |
| 2.4.1 Shear stress | 26 |
| 2.4.2 Flow mixing | 26 |
| 2.4.3 Blockage and separation | 27 |
| 2.4.4 Compressible flow | 27 |
| 2.5 Stall and surge | 28 |

| | | |
|----------|---|-----------|
| 2.5.1 | Rotating stall | 28 |
| 2.5.2 | Surge | 29 |
| 3 | Flow equations and models | 31 |
| 3.1 | Governing equations for compressible flows | 32 |
| 3.2 | Reynolds Averaged Navier-Stokes equations | 34 |
| 3.3 | Eddy-viscosity models | 35 |
| 3.3.1 | Menter SST $K - \omega$ model | 35 |
| 3.3.2 | Turbulent boundary layer | 36 |
| 3.4 | Ansys CFX | 38 |
| 3.4.1 | Finite Volume method (FVM) | 38 |
| 3.4.2 | Discretization errors | 42 |
| 3.4.3 | Courant number | 43 |
| 4 | Geometries and meshing strategies | 45 |
| 4.1 | Compressor geometries | 45 |
| 4.1.1 | HT compressor | 45 |
| 4.1.2 | STT "Scania" compressor | 49 |
| 4.2 | Mesh | 49 |
| 4.3 | Grid independence study | 53 |
| 4.3.1 | Definition of the grids | 54 |
| 4.3.2 | Extrapolation of the solution | 56 |
| 4.3.3 | Boundary layer resolution | 59 |
| 4.4 | Interfaces | 61 |
| 4.4.1 | Interface models | 62 |
| 5 | Steady-state simulations on the HT compressor | 65 |
| 5.1 | Simulation setup | 65 |
| 5.2 | Results | 67 |
| 5.2.1 | Nominal case | 67 |
| 5.2.2 | Summary | 75 |
| 5.2.3 | Effect of the axial tip-clearance | 76 |
| 5.2.4 | Position of the wheel-to-diffuser interface | 81 |
| 5.3 | Concluding remarks | 85 |
| 6 | Design optimization | 89 |
| 6.1 | Design of Experiments (DoE) | 89 |
| 6.1.1 | Design methods | 91 |
| 6.2 | Gear shift and surge | 93 |
| 6.2.1 | Blow-off valves | 94 |
| 6.2.2 | Ported shroud | 95 |
| 6.3 | Ported shroud design optimization | 95 |

| | | |
|----------|--|------------|
| 6.3.1 | Experimental setup | 96 |
| 6.3.2 | Experiment and results | 97 |
| 6.4 | Numerical DoE | 98 |
| 6.4.1 | Geometry | 98 |
| 6.4.2 | Steady state simulations | 99 |
| 6.4.3 | Numerical DoE setup | 103 |
| 6.4.4 | Transient simulations | 104 |
| 6.4.5 | Results | 106 |
| 6.4.6 | Fields | 111 |
| 6.5 | Concluding remarks | 115 |
| 7 | Final remarks | 117 |
| 8 | Limitations and future work | 119 |
| | Bibliography | 121 |
| A | Removal of the ported shroud cavity | 125 |
| A.1 | Flow visualizations | 126 |

List of Figures

| | | |
|------|---|----|
| 1.1 | Ideal cycle and indicator diagram for the Diesel cycle | 3 |
| 1.2 | Scheme of a turbocharged engine | 5 |
| 2.1 | Main components of a centrifugal compressor | 11 |
| 2.2 | Vaneless and vaned diffusers | 14 |
| 2.3 | Compression process on the $h - s$ diagram and compressor map | 17 |
| 2.4 | Velocity triangles at the impeller | 19 |
| 2.5 | Secondary flow at the impeller | 22 |
| 2.6 | Jet-wake model at the impeller exit | 23 |
| 2.7 | Volute flow field | 26 |
| 2.8 | Rotating stall | 29 |
| 3.1 | Law of the wall | 37 |
| 3.2 | Ansys CFX workflow | 38 |
| 3.3 | FVM control volume | 39 |
| 4.1 | HT compressor (1) | 46 |
| 4.2 | HT compressor (2) | 46 |
| 4.3 | Scania compressor (1) | 48 |
| 4.4 | Scania compressor (2) | 48 |
| 4.5 | Mesh of the HT compressor | 50 |
| 4.6 | Mesh of the Scania compressor | 50 |
| 4.7 | Residual plots | 52 |
| 4.8 | Grid independence study | 55 |
| 4.9 | Richardson extrapolation for Mach and pressure | 58 |
| 4.10 | Richardson extrapolation failure | 59 |
| 4.11 | y^+ distribution over the impeller | 60 |
| 4.12 | Nomenclature of the interfaces | 61 |
| 5.1 | Nominal case: compressor map | 67 |
| 5.2 | Nominal case: efficiency of each component | 69 |
| 5.3 | Position of the pressure probes | 70 |
| 5.4 | Nominal case: pressure measurements | 70 |

| | | |
|------|--|-----|
| 5.5 | Nominal case: Mach number over the impeller | 72 |
| 5.6 | Nominal case: pressure over the impeller | 72 |
| 5.7 | Nominal case: meridional velocity field | 73 |
| 5.8 | Nominal case: meridional pressure field | 73 |
| 5.9 | Nominal case: horizontal velocity field | 74 |
| 5.10 | Nominal case: horizontal pressure field | 74 |
| 5.11 | Axial tip-clearance: compressor map | 77 |
| 5.12 | Axial tip-clearance: efficiency variation and $C_{p,diff}$ | 78 |
| 5.13 | Axial tip-clearance: efficiency of the components | 78 |
| 5.14 | Axial tip-clearance: meridional velocity field | 79 |
| 5.15 | Axial tip-clearance: meridional pressure field | 80 |
| 5.16 | Position of the wheel-to-diffuser interface | 82 |
| 5.17 | Parametric interface: variations of pressure ratio and efficiency | 83 |
| 5.18 | Parametric interface: compressor map | 84 |
| 5.19 | Parametric interface: horizontal field | 85 |
| 5.20 | Parametric interface: velocity field at the impeller outlet | 86 |
| | | |
| 6.1 | One factor at-a-time <i>vs</i> Design of Experiments approach | 90 |
| 6.2 | Gear shift mechanism on a gasoline engine | 93 |
| 6.3 | Blow-off valves | 95 |
| 6.4 | Parametric ported shroud cavity | 99 |
| 6.5 | Temperature at the inlet-to-wheel interface | 100 |
| 6.6 | Temperature and Mach number field over the impeller | 101 |
| 6.7 | Location of the temperature probes | 102 |
| 6.8 | Evolution of T_{PS} , T_1 and T_{PS}/T_1 for different design points | 103 |
| 6.9 | DoE field | 104 |
| 6.10 | Wheel speed and $\dot{m}_{corr,out}$ variation | 105 |
| 6.11 | Results of the DoE study | 106 |
| 6.12 | Evolution of the surge indicators in time | 107 |
| 6.13 | Correlation between surge indicators and design parameters | 109 |
| 6.14 | Variation of compressor performance in time | 110 |
| 6.15 | Courant number distribution over the compressor | 112 |
| 6.16 | Temperature and velocity evolution for best and worst designs | 113 |
| 6.17 | Velocity evolution over the impeller for best and worst designs | 114 |
| | | |
| A.1 | HT compressor: designs with and without ported shroud cavity | 125 |
| A.2 | No ported shroud: compressor map | 126 |
| A.3 | No ported shroud: velocity and temperature fields over the meridional plane | 127 |

List of Tables

| | | |
|-----|--|-----|
| 2.1 | Nomenclature of pumps and compressors | 10 |
| 4.1 | Mesh quality parameters | 51 |
| 4.2 | Results of the grid independence study | 57 |
| 5.1 | Boundary conditions for steady-state simulations | 66 |
| 5.2 | Positions of the wheel-to-diffuser interface | 82 |
| 6.1 | Overview of the most used DoE methods | 92 |
| 6.2 | Boundary conditions for transient simulations | 100 |
| 7.1 | Computational time of each simulation | 118 |

List of Symbols

| Symbol | Description | Unit |
|----------------|--|----------|
| α | angle of the flow spiral | [rad] |
| b_2 | blade height at the exducer | [mm] |
| B | blockage factor | |
| β | upwind factor | |
| c_p | specific heat capacity at constant pressure | [J/kg·K] |
| c_s | slip velocity | [m/s] |
| c_v | specific heat capacity at constant volume | [J/kg·K] |
| c_r | radial velocity in the stationary reference frame | [m/s] |
| c_θ | tangential velocity in the stationary reference frame | [m/s] |
| \vec{c} | velocity in the stationary reference frame | [m/s] |
| $C_{p,diff}$ | pressure coefficient of the diffuser | |
| Co | Courant number | |
| γ | ratio of specific heats (c_p/c_v) | |
| Γ_{eff} | effective diffusivity | |
| D | diameter | [m] |
| δ | (1) p_1^0/p_{ref} ratio (2) boundary layer height | |
| δ_{ij} | Kronecker delta | |
| e | specific static energy | [J/kg] |
| e^0 | specific total energy | [J/kg] |
| e_a^{ij} | approximate relative error between different grids | |

| | | |
|-------------------|---|-----------------------------------|
| e_i^{ext} | extrapolated relative error to the i^{th} grid | |
| \hat{E}_S | relative error | |
| ϵ | turbulence dissipation | [m ² /s ³] |
| f | generic variable | |
| f_i | external forces | [N/kg] |
| \bar{f} | Reynolds average | |
| \tilde{f} | Favre average | |
| f' | Reynolds fluctuation | |
| f'' | Favre fluctuation | |
| \vec{F}_{Cor} | Coriolis force | [N] |
| ϕ | passive scalar | |
| ϕ_{ext} | extrapolated variable | |
| GCI_{fine}^{21} | fine-grid convergence index | |
| h | specific static enthalpy | [J/kg] |
| h^0 | specific total enthalpy | [J/kg] |
| i | (1) n° of cylinders generic index | |
| j | generic index | |
| K | turbulence kinetic energy | [J/kg] |
| κ | (1) thermal conductivity (2) von Karman constant | [W/m·K] |
| \dot{m} | mass flow rate | [kg/s] |
| \dot{m}_{corr} | corrected mass flow rate | [kg/s] |
| M | Mach number | |
| η_{Diesel} | efficiency of the Diesel cycle | |
| η_{ts} | isentropic stage efficiency (total-to-static) | |
| η_{tt} | isentropic stage efficiency (total-to-total) | |
| n | (1) n° of engine strokes (2) n° of observations | |
| n_j | outward normal surface vector | |
| N | (1) rotational speed (2) n° of impeller blades | [rev/min] |
| N_i | shape functions | |
| N_{corr} | corrected rotational speed | [rev/min] |
| $p_{mi,n}$ | net indicated mean effective pressure | [Pa] |

| | | |
|-------------------|--|-----------------------------------|
| p | (1) static pressure (2) apparent order of the discretization method | [Pa] |
| p^0 | total pressure | [Pa] |
| P | production of turbulent kinetic energy | [m ² /s ³] |
| P_{brake} | power available at the brake | [W] |
| PR_{ts} | total-to-static pressure ratio | |
| PR_{tt} | total-to-total pressure ratio | |
| q_i | heat flux | [W/m ²] |
| $rg(X_i)$ | rank of the variable X_i | |
| r_s | Spearman's rho | |
| \vec{r} | radius vector | [m] |
| R | degree of reaction | |
| Re | Reynolds number | |
| s | (1) specific entropy (2) surface of integration | [J/kg·K] [m ²] |
| S_{ij} | deformation rate tensor | [s ⁻¹] |
| S_{U_i}, S_ϕ | source terms | |
| σ | (1) slip factor (2) standard deviation | |
| σ_{ij} | stress tensor | |
| ρ | density | [kg/m ³] |
| t | time | [s] |
| t_2 | axial tip-clearance at the exducer | [mm] |
| T | static temperature | [K] |
| T_S | Sutherland constant | [K] |
| T^0 | total temperature | [K] |
| τ' | cut-off ratio | |
| τ_w | wall shear stress | [N/m ²] |
| τ_{ij} | Reynolds stress tensor | [N/m ²] |
| θ | (1) T_1^0/T_{ref} ratio (2) generic angle | [rad] |
| u_i, u_j | velocity components | [m/s] |
| u_τ | friction velocity | [m/s] |
| u^+ | dimensionless velocity | [m/s] |
| \vec{U} | tangential blade velocity | [m/s] |

| | | |
|--------------------------|---|---------------------|
| μ | dynamic viscosity | [Pa·s] |
| μ_0 | dynamic viscosity at reference conditions | [Pa·s] |
| μ_T | turbulent (dynamic) eddy viscosity | [Pa·s] |
| μ_{eff} | effective (dynamic) viscosity | [Pa·s] |
| \mathcal{V} | volume | [m ³] |
| \mathcal{V}_{disp} | volumetric engine displacement | [m ³] |
| ν | kinematic viscosity | [m ² /s] |
| ν_T | turbulent (kinematic) eddy viscosity | [m ² /s] |
| w_r | radial velocity in the moving reference frame | [m/s] |
| w_θ | tangential velocity in the relative reference frame | [m/s] |
| \vec{w} | velocity in the relative reference frame | [m/s] |
| ω | turbulent specific dissipation rate | [s ⁻¹] |
| $\overleftarrow{\omega}$ | rotational speed | [rad/s] |
| χ | backswEEP angle | [rad] |
| $(x, y, z), (X, Y, Z)$ | Cartesian coordinates | [m] |
| y^+ | wall y-plus | |

Abbreviations

| | |
|------|-----------------------------------|
| BMEP | Brake Mean Effective Pressure |
| BOV | Blow-off valve |
| CFD | Computational Fluid Dynamics |
| DoE | Design of Experiments |
| FVM | Finite Volume Method |
| HPC | High Pressure Cycle |
| IMEP | Indicated Mean Effective Pressure |
| LES | Large Eddy simulations |
| LPS | Low Pressure Cycle |
| LRN | Low Reynolds Number |
| OFAT | One Factor at-a-Time |
| RANS | Reynolds Averaged Navier Stokes |

Chapter 1

Introduction

For more than twenty years now, the effects of global warming have been alarming many scientists around the globe. The main responsible for global warming has been identified in the increasing concentration of carbon dioxide CO_2 in the atmosphere: it is proven, in fact, that carbon-cycle feedbacks can significantly lead to an acceleration of the climate change during the XXI century [1][2]. Furthermore, chemical species such as carbon monoxide (CO), nitrogen oxides (NO_x) and other combustion products contribute to further harm and poison the environment.

Internal combustion engines (ICE) play a big role in the emission of such species. UE polices report that light-duty vehicles are responsible for 15% of European Union's emissions of CO_2 ¹. Moreover, toxic emissions from heavy-duty vehicles like trucks have risen by over 30% between 1990 and 2007, mainly due to increasing road traffic². Nowadays, emissions have been measured to be around 19% above 1990 levels. In light of the above, reduction of fuel consumption, CO_2 and toxic emissions is important not only to achieve better engine efficiency but also to preserve the environment.

Although the usage of electric and hybrid engines is rapidly increasing, the internal combustion engine is still the most spread propulsion system installed on vehicles. In particular, among the approximately 14.5 millions cars registered in the European Union during the whole year 2016 [3], only 600 thousands resulted to be powered by an electric engine, i.e. approximately 4% of the total [4].

Thanks to the technological development of the past century, the internal combustion engine is today a mature technology: infrastructures and knowledge are nowadays consolidated in all automotive companies. New "green" technologies, however, are also studied and lots of research is on-going in this field. Most ICE systems run on either the Otto or the Diesel engine cycle. Both of them require fossil

¹<https://ec.europa.eu/clima/policies/transport/vehicles/>

²https://ec.europa.eu/clima/policies/transport/vehicles/heavy_en

fuel (gasoline or Diesel fuel, respectively) during the combustion: as a consequence, production of CO_2 and harmful chemical species always accompany this process.

European Commission's 2016 Low-emission mobility strategy [5] goal is to reduce transport greenhouse gas emissions by at least 60% by 2050 in relation to the 1990 levels. This regulation has been transposed by all European truck constructors: Scania, in particular, set a target of achieving a 25% reduction in CO_2 emissions by 2020. To achieve this goal, research is being done on electric/hybrid engines, alternative fuels, external aerodynamics, materials and turbocharging strategies.

1.1 Internal combustion engines

Most ICE are based on either Otto or Diesel thermodynamic cycles. The first one starts with an isentropic compression, and is then followed by a further isochoric compression and two subsequent expansions, the first isentropic, the second isochoric. Same description holds also for the Diesel cycle, but the second compression is now isobaric. The process just described is usually referred as high pressure cycle (HPC) in literature. Furthermore, both Diesel and Otto cycles require two additional strokes in order to exhaust the air mixture from the previous combustion and aspirate clean air into the combustion chamber. This second process is usually referred as low-pressure cycle (LPC).

Diesel and Otto cycles best represent the working cycle of the piston in an automotive engine. Each phase of the cycle corresponds, in fact, to actual processes of the piston, namely:

- isobaric expansion: the piston moves downwards and clean air is introduced in the combustion chamber through the intake valve;
- isentropic compression: the piston moves upwards and compresses the air/fuel mixture;
- isochoric/isobaric compression: combustion process takes place either at almost-constant volume through generation of an high-voltage spark (Otto engine) or at almost-constant pressure with spontaneous ignition due to the high temperature (Diesel engine);
- isentropic expansion: the ignited mixture expands and pushes the piston downwards. The high thermal energy contained in the gases is converted into kinetic energy which is provided to the crankshaft;
- isochoric expansion: the high-pressure cycle ends with an expansion whose main aim is to cool the air-fuel mixture;

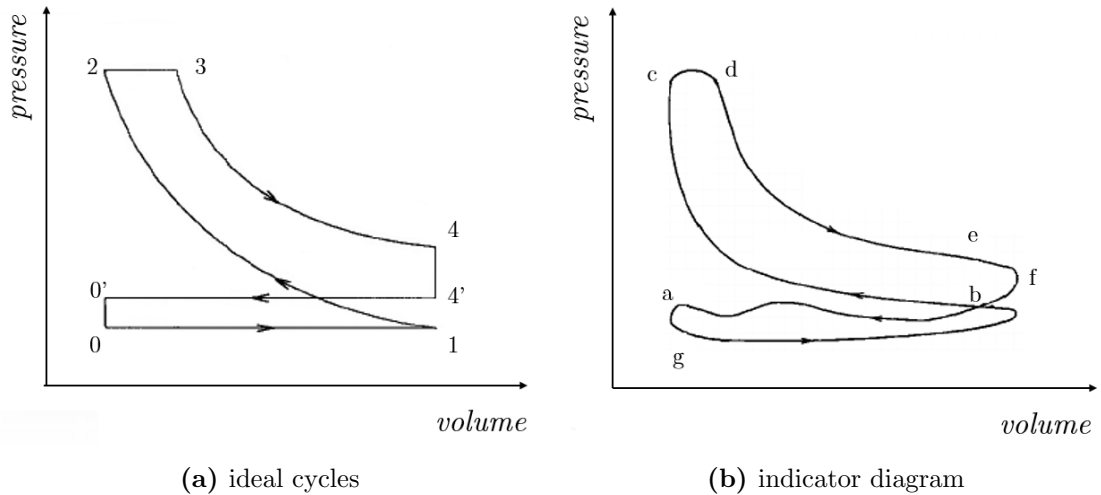


Figure 1.1: Comparison between ideal cycles and indicator diagrams for a 4-stroke Diesel engine.

- isobaric compression: the piston moves upwards and the exhaust gases exit the combustion chambers through the exhaust valve.

Figure 1.1a illustrates the Diesel cycles on a volume-pressure diagram: 12344' draws the high pressure cycle, 4'0'01 the low pressure one. The latter contributes negatively to the overall thermodynamic work. Pressure in the combustion chamber reaches its minimum when clean air is intaken: the positive pressure gradient which is established during the opening of the intake valve allows the introduction of new external air. Diesel cycle features will be investigated hereafter, but similar conclusions can be obtained for the Otto one as well.

Different losses contribute to lower the effective work produced by the engine. On the one hand, the air-fuel mixture undergoes across a huge variation of temperature, changing thus its physical properties (specific heat coefficients and adiabatic exponent) and reaching conditions, in the most dangerous cases, for dissociation. Furthermore, real case phenomena such as heat transfer between fluid and walls, non-ideal combustion process and complexity of the intake-exhaust phases drastically increase the divergence from the ideal cycles shown in Figure 1.1a. All these losses are accounted for the so called indicator diagram, an example of which is reported in Figure 1.1b. Here, the positive work, i.e. the area drawn by the high pressure cycle $bcdef$, is smaller than the corresponding one on the ideal cycle, i.e. the area $4'234$ on Figure 1.1a. On the other hand, the negative work produced by the low pressure cycle agb on the indicator diagram is higher than the corresponding ideal one, i.e. the area drawn by the ideal cycle $0'01$.

A common tool used to evaluate real engine performance is the net indicated mean effective pressure (IMEP_n or $p_{mi,n}$) which measures the work of the indicated

thermodynamic cycle per engine displacement \mathcal{V}_{disp} :

$$p_{mi,n} = \frac{\int_{cycle} p d\mathcal{V}}{\mathcal{V}_{disp}} \quad (1.1)$$

The output work, i.e. the work calculated from the available brake torque, must take into account also the losses due to friction and other mechanical losses. By subtracting friction/mechanical losses to the $p_{mi,n}$ it is possible to define another useful parameter, the brake mean effective pressure (BMEP or p_{me}). Usually, BMEP is directly calculated from the power available at the brake P_{brake} :

$$p_{me} = \frac{60iP_{brake}}{n\mathcal{V}_{disp}} \quad (1.2)$$

where i and n are respectively the number of revolutions per power stroke ($= 1$ for a 4-stroke engine, $= 2$ for a 2-stroke engine) and the rotational speed of the engine shaft. Both $IMEP_n$ and BMEP are used to compare performance of different internal reciprocating engines.

1.1.1 Performance and turbochargers

Along with $IMEP_n$ and BMEP, other used performance indicators are the volumetric compression ratio ρ and the efficiency of the thermodynamic cycle η . Referring to the ideal thermodynamic cycles represented in [Figure 1.1a](#), these two parameters are defined as:

$$\rho = \frac{\mathcal{V}_1}{\mathcal{V}_2} \quad (1.3)$$

$$\eta_{Diesel} = 1 - \frac{1}{\rho^{\gamma-1}} \left[\frac{\tau'^{\gamma} - 1}{\gamma(\tau' - 1)} \right] \quad (1.4)$$

where $\gamma = 1.4$ for ambient air and $\tau' = \mathcal{V}_3/\mathcal{V}_2$ is the so-called cut-off ratio of the Diesel cycle. Efficiency of the process can be increased by increasing the compression ratio, but the strength of the materials put a defined boundary for the maximum value. Nowadays, the maximum available compression ratio for a Diesel engine is about 24:1.

Efficiency is a measure of how well the introduced heat is converted into output work. For internal combustion engines, a good way of increasing both efficiency and work is the implementation of a turbocharger.

The working principle of a turbocharger can be summarized as follows: exhaust gases from the combustion process are used to drive a turbine which is connected by a common shaft to the compressor. The latter, instead, receives fresh ambient

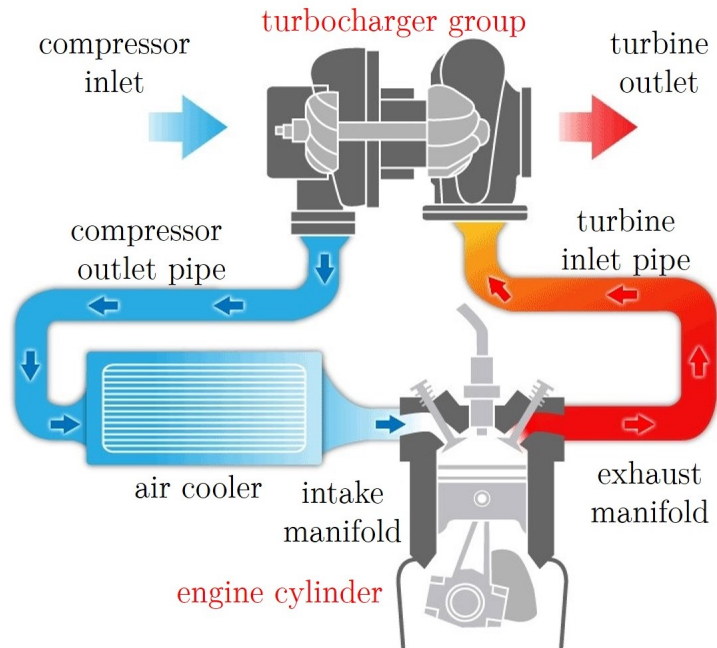


Figure 1.2: Scheme of a turbocharged engine. Adapted from hybridurbos.com

air, compresses it and introduces it into the cylinders. A scheme of the flow path inside a turbocharged engine is shown in [Figure 1.2](#).

Turbochargers add multiple benefits to an internal combustion engine: the most important ones are summarized in the following points.

- low-pressure cycle now contributes positively to the thermodynamic work: air is intaken into the cylinder at a higher pressure than the one characterizing the exhaust process. On the $p - V$ diagram of [Figure 1.1a](#), the intake process $0 - 1$ moves over the exhaust one $4' - 0'$, resulting in a positive work.
- in internal combustion engines, air is drawn inside the cylinder through the intake valves by the downward stroke of the piston which generates a low pressure zone. The addition of a turbine-driven compressor raises the pressure across the inlet manifold and forces a greater mass of air inside the combustion chamber, increasing the power and torque output of the engine. As a result, high-pressure cycles of [Figure 1.1](#) are shifted towards higher pressures, which results in an increase of both IMEP and output work.
- wasted energy from exhaust gas is recovered by the turbine which transforms it into power to operate the compressor. Turbocharged engines offer improved fuel economy, less CO_2 emissions and better performance than a conventional one.

- Compared to naturally aspirated engines, turbocharged ones require less cylinders and smaller swept volume to deliver the same output torque to the crankshaft. This results in downsized engines characterized by smaller swept volumes, if compared with naturally-aspirated engines delivering the same amount of power: friction losses are therefore decreased and, as a consequence, less emissions are produced. It has been estimated that a 40% downsizing achieved through turbocharging can lead to about 21% reduction in fuel consumption, see the literature (Refs. [6][7]).
- Regarding automotive engines, it has been proved that turbocharging strategies can increase the fuel economy by 30 – 50% [8].

Differently from gasoline engines, Diesel engines do not need an ignition system to ignite the air-fuel mixture. Ignition occurs spontaneously due to the high temperature and pressure reached in the combustion chamber. Diesel engines, therefore, allow higher compression ratios than gasoline engines. In addition, gasoline engines have severe limitations in the maximum pressures reached in the combustion chamber due to detonation that can seriously damage the engine components. In light of these aspects, the implementation of turbochargers is usually associated with Diesel engines. In addition, in these engines the exhaust gases reach a much lower temperature than the one achieved in the spark-ignition ones: turbine blades are therefore less stressed and less expensive technologies and materials can be used for their production.

The ability to deliver large power output in spite of low weight makes the turbocharged diesel engine the most widely used propulsion system for heavy duty trucks. One of the best example available on the market is given by the Scania R730, a turbocharged V8 engine capable of delivering up to 730 hp to the shaft while respecting the Euro 6 requirements in terms of emissions³.

1.2 Computational Fluid Dynamics (CFD)

Until few decades ago, the only method available in automotive companies to test the quality of products and, in particular, engine performance was the execution of experimental tests. As is well known, carrying out experiments takes time and requires a long post-processing phase aimed at analyzing the correctness of the assumptions initially made and to validating the results obtained.

³Örjan Åslund, *Scania's range of Euro 6 V8s completed with the 730*, press info available at https://www.scania.com/group/en/wp-content/uploads/sites/2/2015/09/P13X01EN_V8_range_tcm40-397279.pdf

Theoretical methods and equations can be used for the latter purpose, but these are often limited to simple cases and are not available for complex 3D real cases.

Computational fluid dynamics, which has undergone rapid development in recent decades, nowadays represents a further approach for the study of complex fluid dynamic phenomena. It acts as a complement to both experimental tests and theory and allows a more in-depth study of complex phenomena, such as, for example, the highly unsteady, compressible and turbulent flow developing inside each component of an automotive Diesel engine.

CFD synergistically complements both the theoretical and the experimental approaches, but does not replace either of the two [9]. Several commercial CFD codes have been developed for research and development purposes. The main difference among the codes involves the company which develops the software, but some of them present features which makes them more suitable to address a defined process (combustion, turbomachinery flows or conjugate heat transfer, for example). Examples of widely used software packages in automotive companies are Star CCM+, CFD++, Ansys Fluent/CFX, AVL Fire and OpenFOAM. The package used for this thesis work is Ansys CFX.

1.3 Thesis objectives

Scania works continuously to develop internal combustion engines which can achieve low pollutant emissions and high efficiency. This requires designing components with high performance and low weight while maintaining design constraints. Of high importance is also driver ergonomics, for example noise, and driving feel.

To ensure these requirements, adequate flow modeling through CFD is needed in order to be able to adequately predict the performance of each engine component. Although potential cost-effective gains over experimental testing could be remarkable, the setup of CFD simulations is not simple: in general, a simulation can not reproduce the actual phenomenon with 100% of accuracy. This is mainly due to the intrinsic nature of CFD simulations which aim at solving a set of discretized equations over a discretized domain. Numerous errors are thus introduced, decreasing the accuracy of the numerical solution.

In addition, numerical solutions may differ between each other depending on the turbulence model used to close the RANS equations, the meshing strategies used to create the computational grid, flow assumptions (incompressible or compressible, for example), etc. Moreover, uncertainties can be produced by boundary conditions: the definition of an appropriate set of boundary conditions aimed at reproducing actual 3D phenomena, for example, can represent a quite difficult task.

CFD engineers must therefore study the problem carefully in order to select the correct models and approximations to ensure the reliability of the solution.

This philosophy is used throughout the thesis to analyze an important component of modern turbocharged diesel engines: the compressor. The thesis work is divided in two parts. The first part can be described as an engineering attempt to develop a CFD method for predicting compressor performance which resorts only to steady-state RANS simulations. The model must exhibit a high level of reliability at a reasonable computational cost, in order to be usable in product development. Results provided by the computational model are compared with experimental observations from gas-stand tests performed in Scania.

The second part, instead, involves the investigation of transient surge. In detail, the aim is to answer at the following questions:

- Which indicators can be used to predict the onset of surge when running transient RANS simulations?
- Is there an optimal design of the ported shroud cover which delays considerably (deep) surge and back-flow?

A theoretical overview about centrifugal compressor is provided in [chapter 2](#). Here, all the important performance parameters utilized throughout the thesis and fundamentals of compressor aerodynamics are introduced and discussed.

Governing equations, RANS equations, turbulence and fundamentals of CFD are the main focus of [chapter 3](#). The two compressors used for this Master’s thesis work are reported in [chapter 4](#). The chapter proceeds with the description of the procedure followed for the determination of the optimal mesh size for both compressors. In [chapter 5](#), the results of the first part of the thesis work involving compressor performance analysis through steady-state RANS simulations are reported and discussed. The following [chapter 6](#), instead, is aimed at presenting the results for the second part of the thesis work which involves transient surge analysis and DoE optimization. Finally, concluding remarks and a discussion about limitations and future work are done respectively in [chapter 7](#) and [chapter 8](#).

Chapter 2

Centrifugal compressors

By definition, compressors are fluid-dynamic based machines which increase the pressure of a fluid through conversion of mechanical energy in potential energy. They differ from pumps since they increase the static pressure by first accelerating the flow through moving blades and then decelerating it in a diffuser. The pressure rise in pumps, on the contrary, is obtained through displacement of a piston, for example: the fluid is at rest during the entire operation of the device.

A further distinction regards the operating mode of the machine: one refers to positive displacement compressors when pressure is increased by means of a displacement of the fluid; otherwise, if the increase in pressure is caused by the action of rotating blades, one refers to dynamic compressors or, when mechanical energy is supplied by a turbine, turbomachinery. [Table 2.1](#) summarizes the differences between the different types of pumps and compressors. Dynamic compressors are often implemented on automotive engines to increase performance. Unlike volumetric compressors, which require space and heavy weights to operate, dynamic ones allow a considerable increase in pressure with limited increase of weight and dimensions. This is primarily due to the high speeds reached by the flow as a result of the interaction with the rotating components. Secondly, at a given flow rate, the fraction of the internal volume dedicated to the flow is much higher than the one available inside volumetric compressors.

It is possible to divide dynamic compressors into two categories: axial and centrifugal. In axial compressors, the air flows parallel to the axis of rotation of the rotor; the pressure increase is due to the passage of the flow through different stages of high-speed spinning rotor blades and statoric blades fixed to the external case. The centrifugal (or radial) compressors, on the other hand, is generally equipped with one stage of blades: the flow is accelerated by a spinning rotor at high wheel speeds, deviated by about 90 degrees and conveyed into a diffuser through which the pressure is further increased; finally, the flow is collected in a volute.

Modern turbochargers implemented on automotive engine are equipped exclusively with radial compressors: although characterized by a wider frontal section,

Table 2.1: Classification of the various types of pumps and compressors.

| | incompressible fluid | compressible fluid |
|-----------------------|--|--|
| positive displacement | piston pump vane pump gear pump | piston compressor screw compressor vane compressor |
| turbomachines | centrifugal pump propeller pump jet pump | ventilator fan centrifugal compressor |

they can develop higher compression ratios than a single stage of an axial compressor. Axial compressors, on the other hand, are widely used for aeronautical propulsion where a small front area is necessary for the reduction of the aerodynamic drag. It has been estimated that the overall sectional-area of the axial machine can be half or one-third as much as the one of centrifugal machine [10].

The thesis focuses solely on the analysis of radial compressors: in the following sections the main components, the operating principle, the performance and the main characteristics of the flow field will be described.

2.1 Components

The centrifugal compressor consists of four main elements, namely inlet, impeller, diffuser and volute. All of them are essential to assure a defined level of pressure increase. Each compressor differs from the others depending mainly on configuration, size and shape of the components: the general scheme, however, may be reduced to the these four components. Qualitative structure of the centrifugal compressor is shown in [Figure 2.1](#). The picture reports also the convention adopted for each important location and will be used as a reference throughout the whole thesis.

In automotive applications, radial compressors are usually coupled with radial turbines to form turbochargers: in this configuration the rotation of the turbine transforms the thermal energy of the exhaust gases from the combustion into mechanical one and generates a torque; the latter is transferred to the compressor by a spinning shaft. Both turbine and compressor are thus spinning at the same rotational speed.

The next paragraphs focus on in-depth description of each component of the radial compressor.

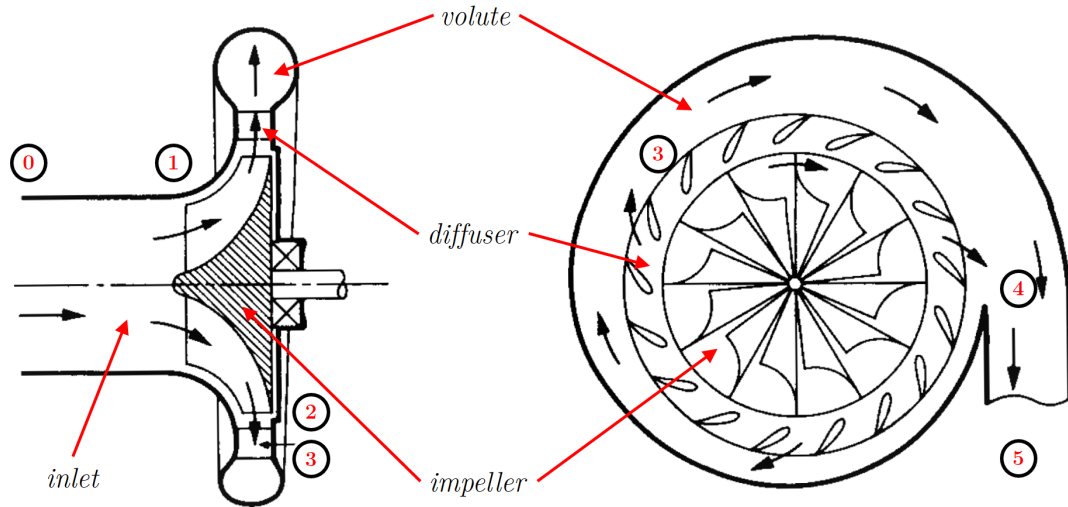


Figure 2.1: Components of a centrifugal compressor. Solid lines on the left figure identify the fluid domain. Important locations are identified by different numbers: 0) upstream flow; 1) impeller inlet (inducer); 2) impeller exit (exducer); 3) diffuser exit; 4) volute exit; 5) outlet. Adapted from Hill & Peterson (Ref. [10]).

2.1.1 Inlet

The purpose of the inlet section is to convey the flow from the air intake zone to the compressor wheel. In general, it consists of a cylindrical tube which conveys the flow towards the inlet section of the impeller. Flow speed and mass flow rate are approximately constant at each operational condition. This section is kept as straight as possible in order to decrease as much as possible the change in linear momentum due to the presence of bends. Due to geometrical restrictions imposed by the shape of the engine casing, it is however not possible to create a perfectly straight inlet section: manufacturers are thus focusing their efforts in moving the bends upstream as much as possible.

Wall surfaces are kept as smooth as possible to avoid flow separation: separated flow could, in fact, seriously affect the stability of the flow and worsen the overall performance. If a compressor is set to operate near surge condition, it is usual to equip the inlet section with a ported shroud, i.e. a recirculating vane for the reverted flow: more details will be given in [subsection 2.5.2](#).

2.1.2 Impeller

The scope of the impeller is to turn the axial flow towards a radial direction: this flow deviation process starts from the inducer, i.e. the impeller entrance, whose aim is to start turning the flow by conveying it across the vanes drawn by the blades. After

being diverted from axial to radial direction, the flow leaves the impeller through the exducer and enters the diffuser.

Impellers spin about their own axes at high rotational speeds: the wheel rotation is necessary to develop a pressure increase from inducer to exducer. Contrary to the axial rotor, in the centrifugal one the pressure rises not only because of the deceleration within the flow passage but also because of displacement in the centrifugal force field, as it will extensively be discussed in [section 2.3](#).

In the unshrouded configuration, the compressor wheel consists in a set of odd number of blades homogeneously distributed around an axial shaft. The reason behind the use of odd number of blades is to avoid coupling effects due to resonance and aeroelastic instabilities.

The main function of these blades, whose shape reminds the one of wing profiles, is to convey the flow across the impeller and increase its pressure. Velocity and pressure variations are dictated by the pressure gradient developing on both sides of each blade: in particular, one can define a suction side (SS) where a favourable pressure gradient is developing ($dp/ds < 0$) and a pressure side (PS) where adverse pressure gradients can be encountered ($dp/ds > 0$).

It is common to insert smaller splitter blades around the shaft: although geometrically similar to the main ones, they span the impeller region only from a section downstream the inducer to the exducer. It has been proven that their addition increases both the static pressure at the impeller exit and the range of operating flow rates between the surge and the choking lines, see the work by Pavesi *et al.* [11]. In addition, they represent the best expedient to both lower the structural loading at the impeller exit and to avoid huge blockage effects at the inducer [12]. The latter effect would appear, in fact, if a larger number of full blades is used. More details about choke, surge and compressor map will be given in the following sections.

Often, especially in automotive applications, the impeller is covered with a shroud which acts as a protective "roof" for the blades. Along with protection from external pollutants which could damage the blades, the shroud can consistently affect the flow field around the impeller: in particular, the small gap between shroud and blade tip is important for the evaluation of the compressor performance, as extensively discussed in [chapter 5](#).

There is also another configuration, the so-called shrouded impeller: in this case, the flow passages are directly scooped inside the shroud; the latter rotates about the axis. No blade-tip clearance appears in this configuration: however, the high inertia of the impeller does not allow a high rotational speed. Shrouded compressors are quite uncommon in turbochargers applications where high rotational speeds are required: these chapter will thus focus only on unshrouded compressors.

Modern turbochargers often have blades that are gradually sloped backwards from the inducer towards the exducer. The degree of blade inclination over the horizontal plane of the compressor can be expressed by means of the backsweep

angle χ : higher backsweep angles allow a reduction of the flow absolute velocity at the exducer and a consequent increase in static enthalpy and static pressure across the impeller.

2.1.3 Diffuser

The diffuser accomodates the flow coming from the impeller. The radius increases across the entire diffuser span, as well as the cross-section area: the flow thus decelerate and increase its static pressure. The simplest type of diffuser for turbocharger applications is the vaneless. Its geometry is very simple: it consists of parallel or almost parallel walls which form a radial annular passage from the exducer to an established outlet radius of the diffuser. The other option is the vaned diffuser: its shape is similar to the vaneless one but some inner wedges (Figure 2.2) are introduced to guide the flow towards the volute.

One important parameter useful to analyze the contribution of the diffuser is the degree of reaction:

$$R = \frac{h_2 - h_1}{h_3 - h_1} \quad (2.1)$$

where h is the specific static enthalpy evaluated at the i^{th} location over the compressor (ref. Figure 2.1). Ordinary values assumed by this parameter ranges between 0.55 – 0.55. When backsweep impellers are introduced, the degree of reaction increases: in other words the pressure rise across the diffuser decreases, as well as the static enthalpy.

The reason why higher values of R are preferable is that the flow field in the diffuser is strongly non-uniform and losses in total pressure are introduced by mixing processes. Backswept blades, in particular, can increase the pressure rise contribution given by the impeller: here, compression occurs more efficiently than in the diffuser and higher efficiency and performance can thus be achieved.

Another good performance indicator of the diffuser is the pressure coefficient:

$$C_p = \frac{p_3 - p_2}{p_2^0 - p_2} \quad (2.2)$$

where p^0 identifies the total pressure; the subscripts refer to the locations defined in Figure 2.1. This parameter accounts of the amount of compression happening in the diffuser. Typical values of C_p are 0.7 for vaned diffusers and 0.5 for vaneless ones. The geometrical simplicity makes the vaneless the most used solution for turbochargers: low cost is in fact required for its production. Moreover, the absence of vanes avoids the creation of both throat sections that can choke and separation at the leading edge due to the angle of attack between flow and wedges. On the other hand, when maximization of the pressure rise is required, vaned diffusers represent a better solution.

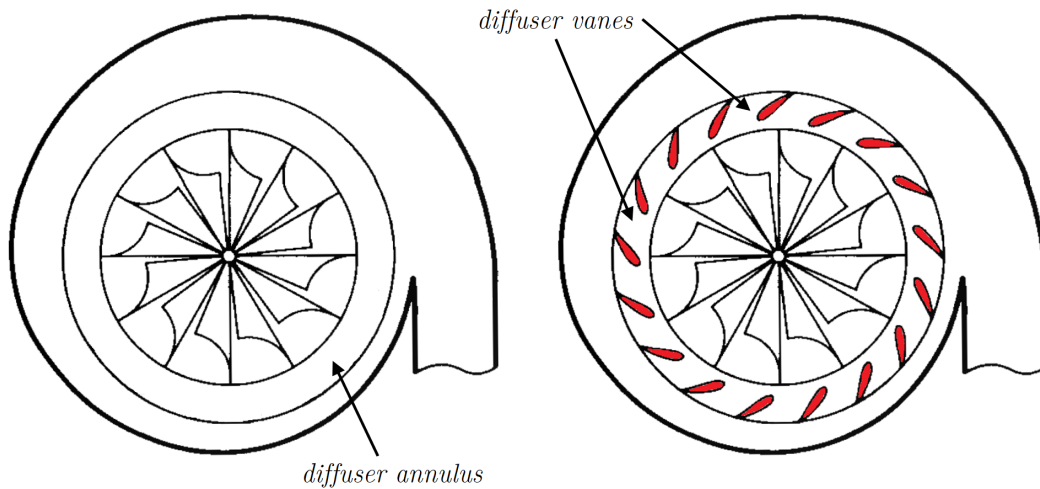


Figure 2.2: Different configurations of diffusers: vaneless (left), vaned (right). Adapted from Hill & Peterson (Ref. [10]).

2.1.4 Volute

Once the flow has crossed the diffuser, it enters the volute. The latter is nothing more than a tube of circular section which spans along the outer circumference of the diffuser: its function consists in guiding the flow in such a way to make it parallel to the walls of the outlet pipe. Moreover, at well-defined conditions (see subsection 2.3.3), it contributes to further raise the pressure level of the flow by converting dynamic pressure into static one. One important feature to consider when designing a compressor volute is the tongue: it is simply the edge that results where the annular tube surrounding the diffuser intersects with the outlet pipe. The volute tongue can be a source of separation due to the high angle of attack that the flow forms with the tongue leading edge. It also affects the flow development in the diffuser, leading to an uneven pressure and velocity distribution along the tangential direction.

2.2 Performance

In this section, the most important parameters used to define compressor performance will be introduced and discussed. For this section only, the subscripts 1 and 2 will indicate respectively the inlet and the outlet sections of the compressor.

When dealing with performance, one mainly refers to the behavior of both air flow, i.e. change in pressure, temperature, mass flow, and compressor parameters like pressure ratio or efficiency when different compressor speeds are considered.

Due to the various geometries of centrifugal compressors available on the market, it is hard to compare their performance by only looking, for example, at the difference in mass flow or outlet pressure. Phenomena such as surge, flow separation, choke, mixing or turbulence can affect in different ways the flow field and it is thus not possible for the customer to decide which compressor could better fit their requirements.

The easiest way to neglect the influence given by both geometry and flow aerodynamics would be the adoption of non-dimensional parameters. This solution lead to the definition of one important parameter, the pressure ratio of the compressor. Depending on whether static or total conditions are considered at the outlet section, one can define the total-to-total pressure ratio:

$$PR_{tt} = \frac{p_2^0}{p_1^0} \quad (2.3)$$

or the total-to-static one, where the stagnation pressure at the outlet is now replaced by the static one:

$$PR_{ts} = \frac{p_2}{p_1^0} \quad (2.4)$$

Use of total-to-total quantities is usually preferred, especially in literature. However, experimental limitations often lead to the adoption of total-to-static ones, since it is not always possible to retrieve total pressure measurement at the outlet: static pressure measurements are easier to perform.

Another important non-dimensional parameter is the Reynolds number. This quantity is used to predict the relative importance of inertial and viscous forces and helps predicting transition from laminar to turbulent regime in different situations. Due to the complexity of the flow structure around the impeller, it is very hard to identify which characteristic length and velocity should be used for its definition. When dealing with similar centrifugal compressor geometries, a very common formulation of Reynolds number is the following:

$$Re = \frac{ND^2}{\nu} \quad (2.5)$$

where N , ν and D represent respectively impeller rotational speed, kinematic viscosity and impeller outlet diameter. By assuming ambient air, a rotational speed of 90000 rev/min and a impeller outlet diameter of 98 mm (approximately design conditions on a conventional centrifugal compressor for automotive turbocharger), one can obtain a Reynolds number of $\sim 6 \times 10^6$. More accurate formulations which weigh the important of each viscous loss source have been developed. Generally speaking, the most serious source is located in proximity of the impeller outlet, as suggested by Cumpsty (Ref. [12]).

Nevertheless, what engineers prefer is to use, whenever possible, dimensional values and scale them in such a way to decorrelate performance from both machine and flow aerodynamics rather than use dimensionless ones. This procedure is used for scaling two important quantities: wheel speed and mass flow rate.

Wheel speed is corrected by means of a temperature-based parameter δ which tries to mimic the dependence of Mach number to temperature, i.e. $M \propto 1/\sqrt{T}$. The resulting corrected wheel speed is defined as follows:

$$N_{corr} = \frac{N}{\sqrt{\theta}} \quad (2.6)$$

where $\theta = T_1^0/T_{ref}^0$. Reference conditions usually refer to sea-level conditions for the standard atmosphere: in particular, generally adopted values are $T_{ref}^0 = 298$ K and $p_{ref}^0 = 101325$ Pa. Also in this case, inlet conditions are defined through total variables since static ones are unknown and depend on the local velocity of the gas.

A convenient way to scale mass flow rates would be the formulation of a dimensional parameter which relates the actual mass flow rate to the choking one passing through the streamtube when $M = 1$. As the speed increases, in fact, the density of the flow could not be considered constant any more and it changes considerably, affecting also the machine performance. One way to address the problem is the formulation of the corrected mass flow rate, which is defined as:

$$\dot{m}_{corr} = \dot{m} \frac{\sqrt{\theta}}{\delta} \quad (2.7)$$

with $\delta = p^0/p_{ref}^0$. This type of correction for the mass flow rate has found wide applications in the turbomachinery field and it is very convenient for drawing compressor maps.

The last performance indicator introduced in this section is the stage efficiency. Given the same compressor, the stage efficiency is defined as the ratio between the work introduced to an ideal compressor where no losses are generated and the work introduced to the actual one. The difference between the two cases is illustrated in [Figure 2.3a](#). Actual compression differs from the ideal one due to the entropy increase of the flow generated by losses. Moreover, compared to the ideal case, flow complexity results in lower pressure at the compressor outlet section. The sum of these losses results in higher mechanical work required to compress the flow, as clearly visible from the difference in total enthalpy in [Figure 2.3a](#). Also for stage efficiency it is possible to define total-to-total or total-to-static quantities; by assuming a calorically perfect gas, one can derive:

$$\eta_{c,ts} = \frac{h_{2,is} - h_1^0}{h_2^0 - h_1^0} = \frac{(p_2/p_1^0)^{\frac{\gamma-1}{\gamma}} - 1}{T_2^0/T_1^0 - 1} \quad (2.8)$$

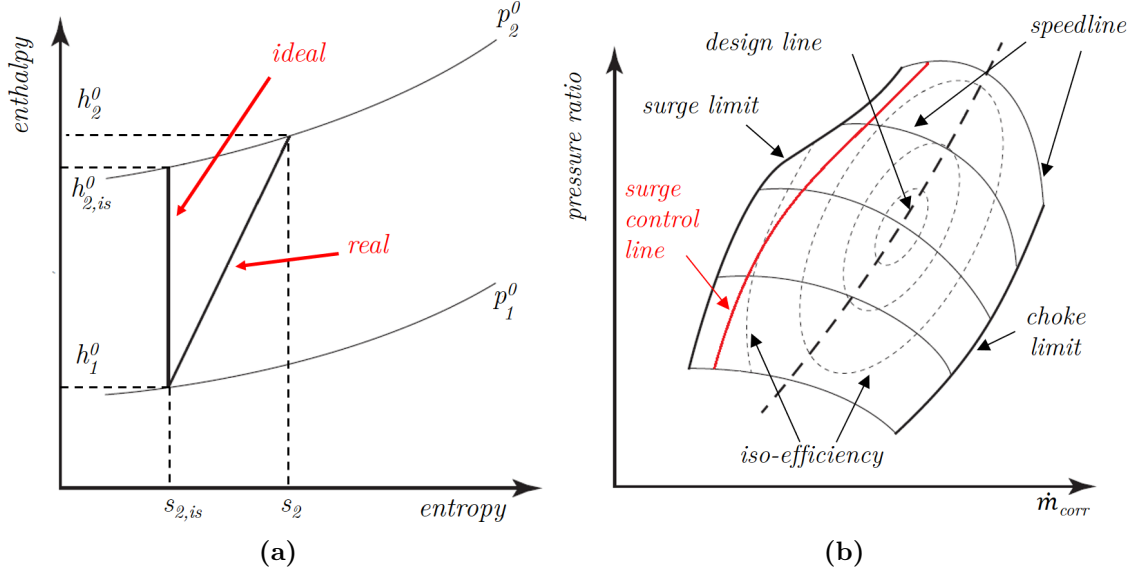


Figure 2.3: Compressor performance on different diagrams. **a)**: ideal and real compression processes on enthalpy-entropy diagrams. **b)**: compressor map. Adapted from Kerres (Ref. [13]).

$$\eta_{c,tt} = \frac{h_{2,is}^0 - h_1^0}{h_2^0 - h_1^0} = \frac{(p_2^0/p_1^0)^{\frac{\gamma-1}{\gamma}} - 1}{T_2^0/T_1^0 - 1} \quad (2.9)$$

where the subscripts *ts* and *tt* identify total-to-static and total-to-total conditions, respectively. Most of the compressors operate at moderate temperature, so that the assumption of calorically perfect gas, i.e. constant c_v and c_p , is reasonable for the purpose of this thesis. The use of either the total-to-total stage efficiency or the total-to-static one depends both on the problem under analysis and the availability of measurements for the stagnation quantities at the outlet.

2.2.1 Compressor map

Compressor performance is defined through relations between the parameters introduced in the previous paragraph. The most common one relates the pressure ratio to both corrected mass flow rate and corrected wheel speed, as follows:

$$PR = f\left(\dot{m} \frac{\sqrt{\theta}}{\delta}, \frac{N}{\sqrt{\theta}}\right) = f(\dot{m}_{corr}, N_{corr}) \quad (2.10)$$

Instead of defining pure analytical relations, what designers prefer is to provide a diagram which relate each parameter to the other ones. This type of approach lies behind the most utilized diagram in turbomachinery, the so-called compressor map. A schematic example of a compressor map is given in [Figure 2.3b](#).

Compressor maps are a common tool used to show the operational range and the design points of a compressor. Usually, the variable on the horizontal axis is the corrected mass flow rate, while the one on the vertical axis is the pressure ratio, either total-to-static or total-to-total. Wheel speed and efficiency lines are drawn by means of iso-lines: in the first case, one can talk of speedlines.

Shown on the map is also a typical steady state design working line. It represents the locus of the operating points of the engine, as it is throttled at different wheel speeds.

Two limits on the operational range can be identified from [Figure 2.3b](#). The first limitation, choked flow, appears at high mass flow rates. At lower mass flow, instead, the compressor encounters surge. Predicting the surge limit is still a hard task to perform with good accuracy. What engineers prefer to do is to provide a surge control line: this line can be calculated from empirical formulas (see Ref. [\[12\]](#) for more details) and add a further limitation to the compressor operational range but is able to avoid the onset of surge on the device. More details on choke and surge will be given in [section 2.5.1](#) and [section 2.5.2](#).

2.3 Compressor aerodynamics

Flow developing along vanes and blade passages is extremely hard to be studied due to its unsteadiness. Unsteadiness is mainly created by the presence of rotating and stationary devices in close interaction one with the other: its effects could be ignored if reference systems fixed to the component under analysis (impeller, for example) are introduced. By changing frame of reference, for example, it is possible to define the so-called velocity triangles of the flow which highlight both absolute and relative flow velocity vectors in proximity of the wheel. Analysis of velocity triangles is very important in order to study compressor performance and to retrieve its operating range. In the following, two different reference frame will be introduced. The first one is a stationary frame whose Z-axis coincides with the impeller longitudinal axis of rotation; the second one is identical to the stationary one but rotates about the Z-axis at a given wheel speed. Cylindrical coordinates are used to describe the evolution of the velocity components along the radial and the tangential directions.

[Figure 2.4](#) shows the typical flow velocity triangles in proximity of the blade tip at both inducer and exducer sections. In particular, three different velocity vectors could be identified:

- absolute velocity \vec{c} : it identifies the flow velocity with reference to the stationary frame;
- relative wheel velocity \vec{w} : it identifies the velocity vector on the relative coordinate system spinning with the impeller;

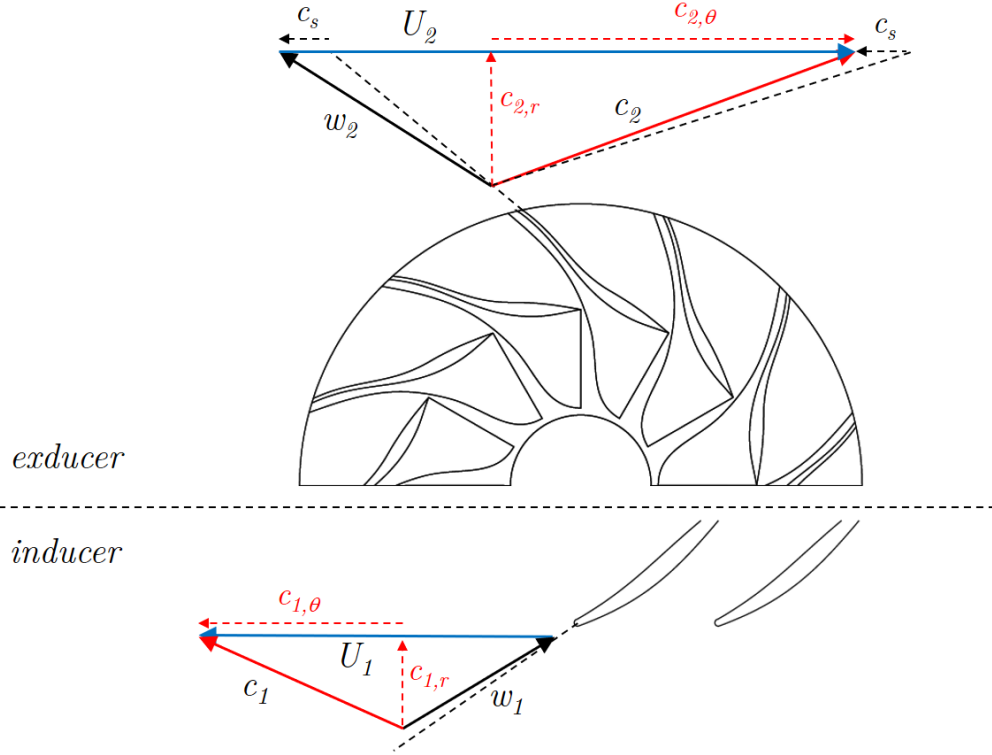


Figure 2.4: Velocity triangles at both inducer and exducer. Adapted from Sundström (Ref. [14])

- tangential blade velocity \vec{U} : it identifies the local velocity of the wheel at a given location. Given the impeller wheel speed $\vec{\omega}$, the tangential blade velocity at location \vec{r} can be written as $\vec{U} = \vec{\omega} \wedge \vec{r}$.

Each of these velocities is defined by their components along the axial (subscript z), radial (subscript r) and tangential (θ subscript) directions. Work input in the compressor is defined by the Euler's turbomachinery equation for adiabatic and steady-state flows:

$$W_{1,2} = U_2 c_{\theta,2} - U_1 c_{\theta,1} \quad (2.11)$$

The aim of the compressor is to increase the static pressure and, thus, the static enthalpy. With reference to the rotating frame, it is possible to re-write [Equation 2.11](#) in a different way:

$$h_2 - h_1 = \int_{p_1}^{p_2} \frac{dp}{\rho} + \int_{T_1}^{T_2} T ds = \frac{1}{2} (U_2^2 - U_1^2) - \frac{1}{2} (w_2^2 - w_1^2) \quad (2.12)$$

where h and p are static enthalpy and static pressure. This equation, known also as conservation of rothalpy, is only valid for steady flows in the impeller rotating frame; in addition, heat exchange to and from the flow is neglected and no work must be

done on the fluid. If the assumption of isentropic flow is introduced, i.e. losses mainly due to shear work and flow mixing are neglected, the entropy-based integral cancels out and Equation 2.12 becomes a good tool for evaluating each contribution to the pressure rise across the impeller.

The compression process is driven not only by the flow deceleration from w_1 to w_2 , but also by the increase of the tangential velocity at the blade tip from U_1 to U_2 : it must be emphasized that this contribution depends only on the wheel design and it does not introduce any loss or irreversibility in the flow. This peculiarity distinguishes centrifugal compressors from axial ones, where in the latter case the variation in magnitude of the peripheral velocity U is negligible and compression is obtained mainly through flow deceleration. Moreover, since the term $\frac{1}{2}(U_2^2 - U_1^2)$ depends only on wheel speed and is independent of irreversible processes like flow separation, centrifugal machines are characterized by higher efficiency and wider operating range than axial ones. In other words, if most of the static enthalpy rise is attributable to the change in blade speed between inlet and outlet, the flow will be less liable to boundary layer separation and flow reversal; the main limitation on pressure rise becomes thus the structural robustness of the wheel components. Manufacturers are today improving blade design to raise as much as possible the difference in tangential blade velocities at inducer and exducer: one immediate solution is the increase of the ratio R_2/R_1 between the blade radius at each of the two locations.

2.3.1 Impeller flow field

The flow field over the impeller is complex. Due to both high velocities developing along the blade vanes, interaction with walls and presence of swirls and vorticity, a 1D theoretical approach may not be accurate enough to predict compressor performance. One must also remember that shock waves can appear at high rotational speeds whenever the local Mach number exceeds the unit. To analyze such complex flow fields is hard not only due to the weaknesses shown by 1D models, but also because the variation of pressure, velocity, temperature and density can not accurately be measured through experiments: the flow is strongly unsteady, averaged quantities can thus only be captured with good accuracy.

The impeller flow field can be divided into two components which allow the problem to be split in two parts and gain a better understanding of the aerodynamics. These components are:

- primary flow: it represents the flow passing through each vane and flowing from the inducer to the exducer.
- secondary flow: it represents the flow at right angles to the primary one. In other words, it can be depicted as the flow perpendicular to the primary direction of the streamlines.

The main aspects of each of these two flow components will be discussed in the following paragraphs.

Secondary flow

As already discussed in [subsection 2.1.1](#), suction and pressure sides (SS and PS) can be identified on each blade. On straight blade designs ($\chi = 0$), suction appears on the advancing side in the direction of the wheel rotation; the pressure is thus higher on the opposite one.

Due to this difference in pressure at each side of the vane, the flow tends to move from pressure to suction side.

On the other hand, being the relative impeller frame rotating at constant wheel speed, the flow is also subjected to inertial accelerations. Among these, an important role is played by the Coriolis acceleration which generates an inertial force \vec{F}_{Cor} on the flow. The latter can be defined as follows:

$$\vec{F}_{Cor} = -2\rho\mathcal{V}(\vec{\omega} \wedge \vec{w}) \quad (2.13)$$

where \mathcal{V} indicates the control volume. This inertial force has a circumferential component which pushes the flow towards the pressure side of the blade with a magnitude proportional to the radial velocity w_r .

Coriolis force and blade pressure force act thus in opposite directions. As a first approximation, the pressure distribution across the blade span can be considered constant. This does not hold, instead, for the Coriolis force, whose intensity is strictly dependent on w_r .

The interaction between pressure and Coriolis forces can be better understood in terms of secondary flow. The resultant secondary flow pattern is displayed on [Figure 2.5](#).

The Coriolis force mainly affects the core flow, while the boundary layer evolution and the flow near the walls is driven only by the pressure force. This is due to the no-slip condition and the low-magnitude of \vec{w} in proximity of the walls. The balance between the two forces generates recirculation and whirls of huge intensity along each impeller vane.

Primary flow and jet-wake model

The complexity of the flow is exacerbated by the presence of boundary layer separation. In unshrouded impellers, there is a small portion of fluid which flows through the tip clearances between shroud and blades, moving thus from one vane to the adjacent one. This flow can be approximated as a Couette-type flow: the shroud wall, in fact, is stationary while the blade-tip one is moving at $v = \omega r$. In this small region, the shear stress is high and the flow tends to separate once it has reached the suction side of the blade. This leads to the formation of a low total pressure

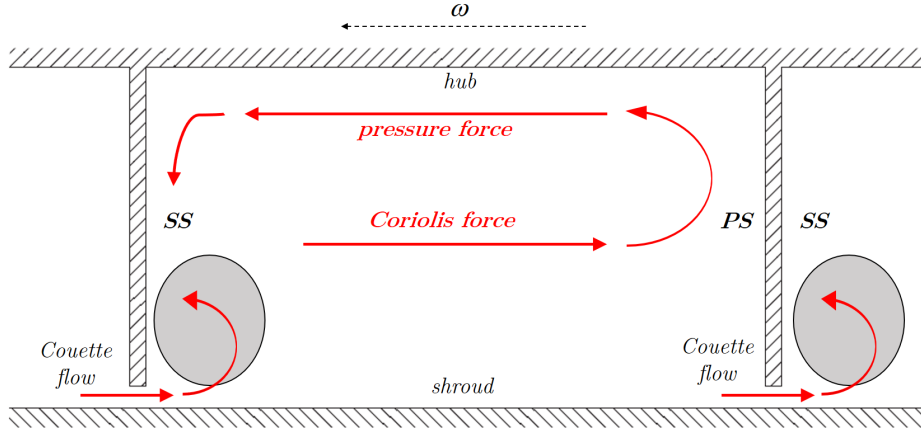


Figure 2.5: Secondary flow.

zone in proximity of the suction side: the nearer the flow is to the blade tip, the higher the total pressure decrease will be.

The resulting flow field at the impeller exit is of course affected by all the unsteady phenomena occurring due to separation and recirculation. The best 1D model available now to understand in a qualitative way the velocity profile at the impeller exit is the so-called jet-wake model, proposed for the first time by Dean and Senoo [15]. A qualitative scheme is shown in Figure 2.6: due to blockage induced by the separation occurring on the suction side, the portion of flow in proximity of the pressure side is accelerated and increases its linear momentum, generating thus a jet-type flow. The separated low-momentum flow exits instead the impeller generating a wake with low velocity and total pressure.

Impeller curvature

In order to increase the static pressure, the flow is bent along the blade vanes: both impeller hub and outer shroud are thus curved to fulfill this requirement. In general, the radius of curvature of the shroud is lower than the one measured at the impeller hub. This difference generates a strong velocity gradient in the radial direction: in particular, the speed near the shroud and in proximity of the blade tip is much higher than that at the hub. While moving downstream towards the diffuser, the deceleration of the flow near the shroud (necessary to guarantee the adequate recovery of static pressure) is so strong that it can cause boundary layer separation. Moreover, the increase in speed and the consequent decrease in pressure along the vanes blades leads to a further decrease density: the flow can easily become supersonic with consequent losses due to the onset of undesired shock waves.

A good design of the inducer can substantially mitigate these problems: in addition to gently guide the flow along the blade vanes, it can also increase gradually

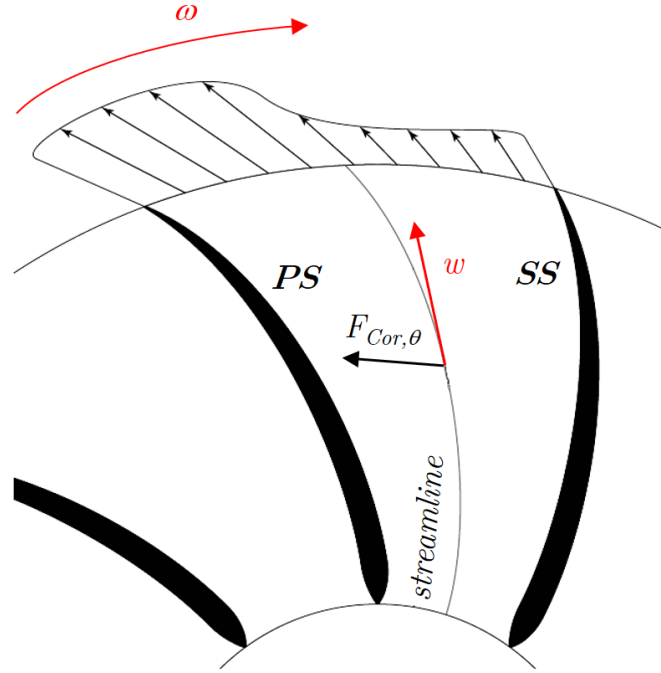


Figure 2.6: Qualitative 1D jet-wake model for the primary flow. The curved line identifies a flow streamline. Adapted from Kerres [13].

the static pressure at the inducer section in order to avoid the rapid compression caused by the high curvature of the shroud. Nowadays, most of the blades of centrifugal compressors are swept backwards at the inducer: in particular, the blade is gradually swept along the radial direction, from the hub to the tip.

Slip factor

The slip factor is defined as the ratio between the actual absolute circumferential velocity of the flow and the ideal one:

$$\sigma = \frac{c_{\theta,2}}{c_{\theta,2,id}} \quad (2.14)$$

It is also possible to define a slip velocity as the difference between the idealized and the actual relative velocity of the flow at the exducer. Being the impeller peripheral velocity U_2 unaffected by the flow evolution, one can write:

$$c_s = w_{\theta,2} - w_{\theta,2,id} = c_{\theta,2} - c_{\theta,2,id} \quad (2.15)$$

The origin of the slip factor lies in the gradual decrease of blade loading at the trailing edge. It is required by the Kutta condition, in fact, that the pressure difference between pressure and suction sides must be zero at the trailing edge. Due

to this reduction in pressure force, the flow does not follow the suction side of the blade any more and tends to turn towards the pressure one as soon as it approaches the exducer; separation may also occur due to the interaction with the secondary flow coming from the tip-clearance. As a result, a slip velocity component in the opposite direction to the impeller rotation arises, decreasing the relative flow velocity at the impeller outlet. The qualitative effect of the slip-factor is shown in [Figure 2.4](#).

Different empirical formulas have been developed during the second half of the 20th century to estimate the magnitude of the slip factor, see Cumpsty, section 6.4 [12]. Among these, one of the most used is the Stodola expression, which assumes irrotational inlet flow and inviscid flow on the impeller:

$$\sigma = 1 - \frac{\pi}{N} \frac{\cos \chi_2}{1 - c_{r,2}/U_2 \tan \chi_2} \quad (2.16)$$

where N is the number of blades, χ_2 is the blade outlet angle with respect to the radial direction, $c_{r,2}$ and U_2 are respectively the radial flow velocity and the tangential blade velocity at the impeller outlet.

2.3.2 Vaneless diffuser flow field

Although the diffuser has a very simple geometry, the aerodynamics of a vaneless diffuser is complicated due to the non-uniformity of the flow coming out from the impeller and the consequences of irreversible processes such as mixing and shear stress. The hybrid jet-wake velocity profile at the inlet strongly affects the flow evolution throughout the entire diffuser: estimation of the losses in the diffuser becomes thus quite complicated.

Assuming inviscid and incompressible flow, one can approximate the diffuser flow as axisymmetric. In this case, the axial angular momentum of the flow rc_θ remains constant, i.e. $c_\theta \propto 1/r$. In other words, the streamlines follow a logarithmic spiral whose direction, given by the following expression, is constant:

$$\alpha = \arctan \frac{c_r}{c_\theta} \quad (2.17)$$

This expression holds true only when the axial width of the diffuser is constant.

As a rule of thumb, one can assume that the shorter the flow path in the diffuser (and the smaller the angle α), the lower the losses will be. If the flow path is long in relation to the axial width, diffusion of viscous effects is amplified and losses associated to mixing and shear stress increase.

Inviscid analysis is a useful tool to give a qualitative understanding of the flow field inside the vaneless diffuser. When coming to performance estimations, however, results obtained through the inviscid approach are not satisfactory and must not be trusted.

2.3.3 Volute flow field

The flow field developing inside the volute is strongly affected by the compressor operating conditions. The description presented in this paragraph is based on the work of Kerres [13].

Differently from what happens inside the diffuser, the tangential component of the velocity is the one that plays the most important role in defining the flow direction and the pressure rise across the volute. In the majority of the cases, the centerline radius of the volute pipe increases in the radial direction along the entire compressor circumference, from the tongue to the outlet pipe: tangential velocity is thus slightly reduced due to the conservation of angular momentum. The radial component, instead, is deflected by the outer wall of the volute and creates a swirl which propagates along the entire length of the outlet tube. A schematic visualization of the volute flow field on a meridional plane is shown in [Figure 2.7](#).

The volute pipe cross-section constantly increases from the volute to the outlet; the section is then usually kept constant along the entire outlet pipe. The cross-sectional area is increased in such a way that it matches the amount of fluid passing through the volute at design conditions: this control of the geometry allows to keep both density and tangential velocity approximately constant.

The situation changes at off-design conditions since additional effects arise. In such cases, the volute behaves differently depending on the mass flow:

- At lower mass flows than design conditions, the cross-sectional area increases faster than the amount of fluid passing through the volute. The volute pipe acts thus as a diffuser: the tangential flow velocity decreases and dynamic pressure is converted into static one. The highest values of tangential velocity can be found in proximity of the volute tongue.
- At higher mass flows than design conditions, opposite results can be observed: the cross-sectional area increases slower than the amount of fluid and the volute acts as a nozzle. In this case it is possible to measure the lowest tangential velocity near the tongue.

2.4 Losses

As already assessed in the previous sections, several losses affect the operation of centrifugal compressors. The most important of them are: shear stress, mixing, blockage and separation, compressible flow effects. The following subsections will be used to give a brief introduction about each of these sources of losses.

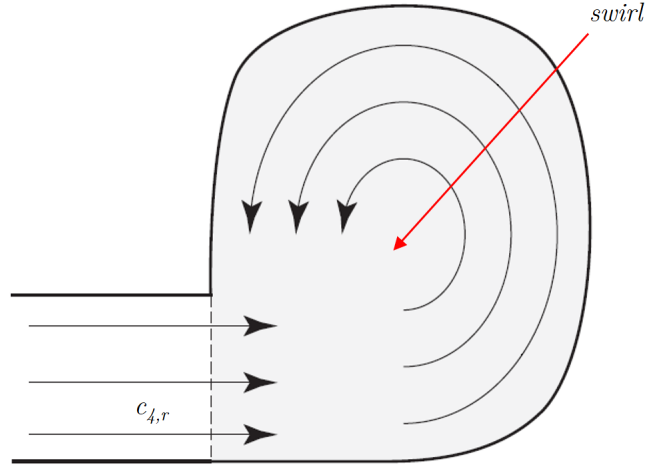


Figure 2.7: Schematic representation of the meridional fluid in the volute. Adapted from Kerres [13].

2.4.1 Shear stress

Shear stress is one of the main sources of losses on the impeller. Compared to axial compressors, centrifugal blades are characterized by long blades with small aspect ratio: the wet area swept by the flow is thus high. In proximity of solid walls, very steep velocity gradients arise due to the no-slip condition, creating high losses due to friction. The wall shear stress is, in fact, directly proportional to the velocity gradient at the wall:

$$\tau_w = \mu \left. \frac{\partial u}{\partial y} \right|_{y=0} \quad (2.18)$$

where y is the direction perpendicular to the wall. The higher the velocity gradient, the higher the shear stress at wall.

It must also be reminded that the Reynolds number is quite high in turbomachines: the boundary layers at both hub, blades and shroud are thus transitional. When a boundary layer becomes turbulent, skin friction increases due to steeper velocity profile at wall. On the other hand, free-stream flow within both impeller and diffuser is highly non-uniform and turbulent: huge pressure and velocity gradients arise, affecting therefore the boundary layer profile and the shear stress.

2.4.2 Flow mixing

Flow mixing always accompanies compressor aerodynamics. Mixing can be encountered in several zones of the compressor: the most important ones are the tip clearances between impeller blades and shroud and the impeller exit characterized by a

jet-wake type of flow. Mixing is likely to appear in case of boundary layer separation: when the flow separates, after having been previously accelerated or decelerated, it is no longer capable of recovering the initial conditions through a thermodynamically reversible process. Mixing is thus the only process which can return the flow to uniform, but losses are introduced in the system.

2.4.3 Blockage and separation

According to Cumpsty [12], blockage can be treated as a reduction of the effective section within which the flow can pass with respect to the actual geometric section available. It is also possible to define a blockage factor, as follows:

$$B = 1 - \frac{\text{effective flow area}}{\text{geometric flow area}} \quad (2.19)$$

The main cause of blockage in compressor aerodynamics is flow separation. Once separated, the flow does not follow the wall surface any more and creates zones of recirculation which restrict the volume at disposal of the upstream flow. Separation and blockage can thus change locally the flow distribution, creating "virtual" zones of convergent or divergent flow which drastically change the pressure levels developing across the entire compressor. A good prediction of separation zones and blockage effects is important during both geometry design, experiments and test validation. Due to its high complexity, blockage becomes of fundamental importance when analyzing the impeller flow field.

2.4.4 Compressible flow

An impeller flow field is often characterized by the presence of transonic flow: velocity can cross the limit $M = 1$, where M indicates the Mach number, in certain zones leading to the creation of huge dissipative zones known as shock waves. Across shock waves, the flow encounters a sudden increase in pressure and a decrease in velocity. Transonic flow appears at high rotational speed and in proximity of choke conditions. At choke, in particular, the amount of flow through the compressor cannot be further increased, in similarity to what happens for a choked de Laval nozzle: the compressor map is thus limited at high mass flow rates.

As the local Mach number increases, the losses due to compressible flow effects (shock waves) increase very rapidly: it can be proven that they are proportional to $(M - 1)^3$ [12]. It is known, in fact, that boundary layer tends to separate once it passes through a shock and blockage effects become very hard to predict.

Shock waves and their consequences are very hard to capture during experiments and its evolution cannot accurately be caught by CFD simulations (RANS models, in particular).

2.5 Stall and surge

Stall and surge are the two problems that most affect the operation of centrifugal compressors. The consequences of stall can be different, and its severity can range from a low power drop to a complete loss of compression with flow reversal (deep surge) towards the inlet of the compressor. Surge, in particular, can lead to a drastic reduction in performance, causing also irrecoverable damage to the engine components.

An introduction to stall, surge and their effect on compressor performance is given in the next subsections.

2.5.1 Rotating stall

On a wing profile, stall occurs when the separation point of the flow on the upper surface has reached the leading edge. Once stall conditions are overcome, the lift generated by the flow surrounding the profile decreases at the expense of an increase in aerodynamic drag. An adverse pressure gradient is mainly responsible for stall: when the positive pressure gradient becomes too strong to be overcome, the flow separates.

This definition of stall holds for external flows. When dealing with internal flows, such turbocharger ones, new parameters must be taken under consideration. At very low mass flows, the amount of fluid flowing over the impeller is not sufficient for the correct operation of the machine: instead of having the flow distributed along the whole circular section of the compressor, the flow is not uniformly distributed, i.e. some vanes receive more fluid than others. Regions of separated flows can be identified along the circular section of the inducer: these stall cells, as commonly referred to literature, arise on the blade vanes characterized by a lower mass flow than the surrounding regions and rotate together with the impeller, see [Figure 2.8a](#).

The phenomenon just described is known as rotating stall and can be potentially dangerous since can lead to catastrophic events if not properly controlled. It is possible to define two different types of rotating stall:

- progressive stall: the drop in performance (pressure ratio, in particular) is quite small but the amount of noise and vibrations produced by the device increase. In this case, it is possible to identify several small stall cells extending across part of the impeller annulus;
- abrupt stall: vibrations and noise couple with a large drop in pressure ratio and performance. The impeller flow field is characterized by the presence of a unique stall cell which spans from the hub to the shroud.

Which of the two types of rotating stall can occur depends on different parameters: the most important ones have been found to be the compressor design and the

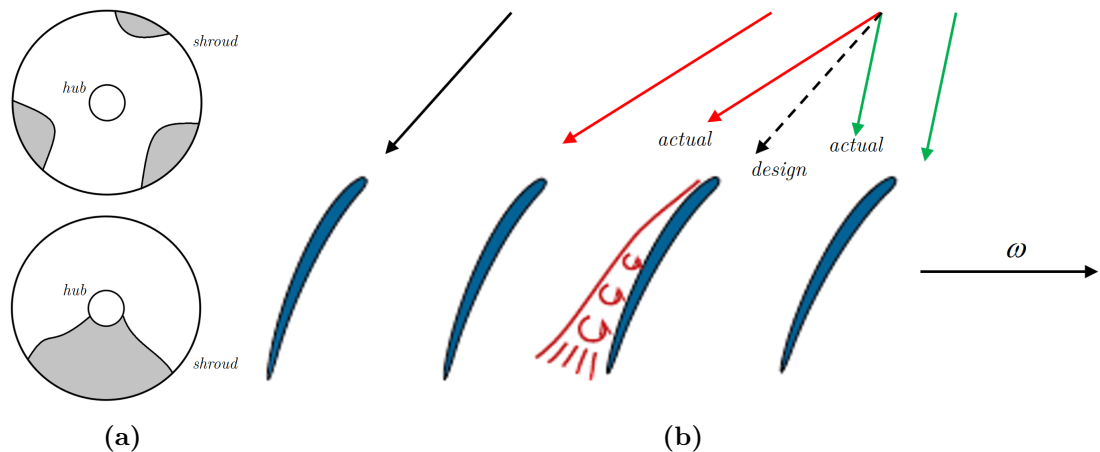


Figure 2.8: **a)** different configurations for the rotating stall cells: progressive stall (above) and abrupt stall (below). **b)** mechanism of stall propagation within the stall cells during rotating stall.

mass flow. In both cases, the overall time-averaged mass flow remains constant, but the stalled cells rotate in the direction of the rotor at lower rotational speed than the impeller (20 – 40% for abrupt stall, 50% for progressive stall).

Figure 2.8b shows the inception of rotating stall cells in a compressor. The stall first affects only one blade and flow separates over its suction surface. The blockage caused by the separated flow generates an increase of incidence on the following blade in the sense of rotation of the impeller and a decrease on the preceding one. Due to the higher incidence, the following blade stalls and the mechanism propagates to the subsequent blades, creating eventually a stall cell. The stall cells grows thus in the opposite direction relative to the impeller rotation.

2.5.2 Surge

Surge denotes an instability which affects compressors at low mass flow regimes. Surge prediction and control is challenging and lots of research today is focusing on such topics: it is known, in fact, that surge is strongly dependent not only on the compressor but also on the other components of the turbocharger [16]. In general, surge can be described as the onset of mass flow variations with time at a defined frequency. These mass flow variations are also accompanied by pulsating pressure and vibration in the system. Due to the unsteadiness of the process, it is not possible to identify separation cells like in the case of rotating stall since the flow pattern inside the compressor changes continuously from being stalled to unstalled.

Depending on the severity of the oscillations, it is possible to distinguish two different types of surge:

- mild surge: pressure and mass flow oscillate with a frequency that matches

the natural one of the system. The operating point of the compressor does not vary a lot on the compressor map, but tends to orbit around the nearest point to the surge line at a given wheel speed. Mild surge can usually be tolerated due to the relatively low level of oscillation. In small turbochargers mild surge usually precedes the onset of deep surge;

- deep surge: oscillations are characterized by lower frequencies than the natural one of the system. Mass flow and pressure variation are however so huge to destabilize the compressor. During part of the surge cycle, the amount of fluid entering the compressor is not sufficient to overcome the high pressure area downstream of the impeller; in this case the flow, after a partial compression, is reversed and re-emerges out of the inlet. This can cause serious damage to both compressor blades and components upstream of the turbocharger unit.

Delaying the onset of surge at lower mass flow represents the easiest way possible to avoid instabilities and surge during operations. There are mainly two methods to accomplish this task: they consist in using either active flow control techniques or passive ones. In addition to preventing the onset of surge, they also allow to extend the width of the compressor map: in other words, more operational points are available along each speedline.

Active flow control techniques include the implementation of variable inlet guide vanes: these devices allow to direct the air onto the inducer at the optimal angle of attack in such a way to delay separation and stall for all the operational points on the compressor map. Passive flow control techniques include casing treatment (like ported shroud), inducer casing bleed system and internal flow recirculation methods, see work by Semlitsch *et al.* [17] for more details and further references. Although very effective, active methods imply a penalization in terms of efficiency: devices such as variable inlet guide vanes require energy for their operation. Moreover, they add complexity to the system, increasing the production costs.

On the other hand, passive methods do not imply loss in efficiency and are easy to implement on compact devices like turbochargers. The most used solution today is the ported shroud and has been found to be very effective to mitigate the effects of deep surge: in this configuration, a part of the reversed flow moving in direction of the inlet is conveyed into a slot hollowed on the shroud casing and then recirculated back to the compressor intake. More details on ported shroud will be given in the following chapters.

Chapter 3

Flow equations and models

Fluid dynamics deals with the description of the flow of fluids. The microscopic behavior of the fluid is described by a set of non-linear partial differential equations which allows to evaluate variations of important flow variables, like pressure, temperature, density and velocity, over the entire domain. The complexity of a fluid-dynamic problem is high since it is often characterized by complex and strongly non-linear phenomena. It should also be remembered that nowadays no analytical solutions are available for the complete Navier-Stokes.

The birth of Computational Fluid Dynamics (CFD), which involves the solution of a discretized form of the governing equations with the help of supercomputers, has made it possible to study flows in complex 3D geometries which are characterized by a high degree of complexity. Computational resources are however limited: it is always necessary, therefore, to make assumptions on the flow in order to reduce the number of variables and the computational time required for the calculations.

The flow inside a radial compressor, as described in [chapter 2](#), is extremely complex. The high velocity reached by the flow near the impeller blades does not allow the assumption of incompressible flow: the condition $M < 0.3$, in fact, is violated in a large part of the domain (the flow is also transonic at high rotational speed). This is the reason why density variations cannot be considered negligible. Furthermore, both viscosity and turbulence play an extremely important role when estimating the losses: assuming inviscid and fully laminar flow would thus lead to erroneous results.

In the following sections the compressible Navier-Stokes equations will be introduced. The discussion will then move to RANS equations and eddy viscosity models. Finally, some elements about Computational Fluid Dynamics will be given.

3.1 Governing equations for compressible flows

The governing equations are used to derive the flow evolution once initial and boundary conditions have been specified. These are, namely: conservation of mass, balance of momentum and balance of energy. These equations can be written either in the integral (conservative) or in the differential form.

Integral formulations are defined within a control volume. A control volume is a region of constant size and shape that appears fixed in space to an external observer. In other words, it can be imagined as a region of space enclosed by an invisible, rigid and massless surface, called the control surface. Mass, energy and heat can be exchanged through the control surface.

Differential formulations can be directly obtained from the integral ones by decreasing the size of the control volume so that it reaches the dimensions of an infinitesimal fluid particle. The Gauss theorem¹ can be used to switch from the integral formulation to the differential one. In this section, only the differential formulation will be adopted. The compressible form of the governing equations, in tensor notation, is reported hereafter:

$$\frac{\partial \rho}{\partial t} + \frac{\partial}{\partial x_i}(\rho u_i) = 0 \quad (3.1)$$

$$\frac{\partial(\rho u_i)}{\partial t} + \frac{\partial(\rho u_i u_j)}{\partial x_j} = -\frac{\partial p}{\partial x_i} + \frac{\partial \sigma_{ij}}{\partial x_j} + \rho f_i \quad (3.2)$$

$$\frac{\partial(\rho e^0)}{\partial t} + \frac{\partial(\rho u_i e^0)}{\partial x_i} = -\frac{\partial(p u_i)}{\partial x_i} - \frac{\partial q_i}{\partial x_i} + \frac{\partial(u_j \sigma_{ij})}{\partial x_i} \quad (3.3)$$

where $i, j = 1, 2, 3$ are the indices of the Cartesian coordinates, u_i, u_j = velocity components, σ_{ij} = stress tensor, f_i = external force, $e^0 = e + 1/2 u_i u_j$ = specific total energy, e = specific inner energy, q_i = heat flux. The first equation describes the conservation of mass, the second one (also known as Navier-Stokes equations) the balance of momentum and the third one the balance of (total) energy. The second term in equation [Equation 3.2](#) is the so-called advection term: it is highly non-linear and describes the force exerted on a fluid particle by the other fluid particles surrounding it.

For our analysis, we will assume $f_i = 0$, i.e. no body or other external forces act on the system. Moreover, the only fluid investigated throughout the thesis is air,

¹The Gauss theorem, known also as the *divergence* theorem, states that the flux of a vector field directed outwards of a closed surface is equal to the volume integral of the divergence over the region inside the surface.

which belongs to the category of the Newtonian fluids. The constitutive relation for Newtonian fluid is described by the following equation:

$$\sigma_{ij} = 2\mu S_{ij} - \frac{2}{3}\mu S_{kk}\delta_{ij} \quad (3.4)$$

where μ identifies the dynamic viscosity of the fluid and δ_{ij} is the Kronecker delta which is equal to 1 when $i = j$, zero otherwise. The deformation rate tensor S_{ij} is defined as:

$$S_{ij} = \frac{1}{2} \left(\frac{\partial u_i}{\partial x_j} - \frac{\partial u_j}{\partial x_i} \right) \quad (3.5)$$

Further assumptions involve viscosity: in particular, the dynamic viscosity is temperature dependant. The formula adopted to describe its evolution is the Sutherland's equation:

$$\frac{\mu}{\mu_0} = \left(\frac{T}{T_0} \right)^{\frac{2}{3}} \left(\frac{T_0 + T_S}{T + T_S} \right) \quad (3.6)$$

where $\mu_0 = 1.736 \cdot 10^{-5}$ Pa · s (ambient air) identifies the dynamic viscosity at $T_0 = 273.15$ K and $T_S = 111$ K is the Sutherland constant.

Heat flux is modelled with the Fourier's law which relates the heat to the temperature gradient, as follows:

$$q_i = -\kappa \frac{\partial T}{\partial x_i} \quad (3.7)$$

where κ is the thermal conductivity of the fluid. The rise in pressure observed inside the compressor is also accompanied by an increase in temperature. The maximum temperature that can be measured, however, is not high enough to allow dissociation or chemical reaction ($T \ll 1000$ K). It is therefore reasonable to assume a calorically perfect gas where specific heat coefficients at constant volume (c_v) and at constant pressure (c_p) are constant. The following relations hold for calorically perfect gases:

$$e = c_v T \quad (3.8)$$

$$h = c_p T \quad (3.9)$$

In order to close the system of equations and solve the compressible flow field, the ideal gas law is introduced:

$$p = \rho R T \quad (3.10)$$

where R identifies the specific gas constant; for air, this constant is equal to $R = 287.05$ J/kgK. In conclusion, given some assumptions, equations (3.1) to (3.10) describe the evolution of compressible flow fields in function of the six unknowns of the problem, i.e. ρ , u_i , p , T .

3.2 Reynolds Averaged Navier-Stokes equations

Turbulence flows involve unsteady variations in the flow variables: velocity, for instance, changes randomly in time. In order to facilitate the study of such complex flows, the so-called Reynolds decomposition can be introduced. By denoting with \bar{f} the time-averaged value of the variable f and with f' its fluctuating component, one can write:

$$f = \bar{f} + f' \quad (3.11)$$

When compressible flows are considered, density variations are taken into account by the so-called Favre decomposition, which represent a generalization of the Reynolds decomposition. By indicating with \tilde{f} the Favre time-average of f and with f'' the fluctuating component, it is possible to write:

$$f = \tilde{f} + f'' \quad (3.12)$$

where $\tilde{f} = \overline{\rho f} / \bar{\rho}$ and $f'' = -\overline{\rho' f'} / \bar{\rho}$. Both Reynolds and Favre decomposition can be applied to the set of governing equations of [section 3.1](#). The latter are obtained through decomposition of all variables in [Equation 3.1](#), [Equation 3.2](#) and [Equation 3.3](#) (Reynolds decomposition for p and ρ , Favre decomposition for all remaining quantities) and further averaging of both left and right-hand sides. The resulting set of equations is:

$$\frac{\partial \bar{\rho}}{\partial t} + \frac{\partial}{\partial x_i} (\bar{\rho} \tilde{u}_i) = 0 \quad (3.13)$$

$$\frac{\partial (\bar{\rho} \tilde{u}_i)}{\partial t} + \frac{\partial (\bar{\rho} \tilde{u}_i \tilde{u}_j)}{\partial x_j} = -\frac{\partial \bar{p}}{\partial x_i} + \frac{\partial \bar{\sigma}_{ij}}{\partial x_j} + \frac{\partial \tau_{ij}}{\partial x_j} \quad (3.14)$$

$$\begin{aligned} & \frac{\partial}{\partial t} \left(\bar{\rho} \left(\tilde{e} + \frac{\tilde{u}_i \tilde{u}_j}{2} \right) + \frac{\overline{\rho u_i'' u_i''}}{2} \right) + \frac{\partial}{\partial x_j} \left(\bar{\rho} \tilde{u}_j \left(\tilde{h} + \frac{\tilde{u}_i \tilde{u}_i}{2} + \tilde{u}_j \frac{\overline{\rho u_i'' u_i''}}{2} \right) \right) = \\ & = \frac{\partial}{\partial x_j} (\tilde{u}_i (\tilde{\sigma}_{ij} - \overline{\rho u_i'' u_i''})) + \frac{\partial}{\partial x_j} \left(-\bar{q}_j - \overline{\rho u_j'' h''} + \overline{\sigma_{ij} u_i''} - \overline{\rho u_j'' \frac{u_i'' u_j''}{2}} \right) \end{aligned} \quad (3.15)$$

where all assumptions done in [section 3.1](#) are still valid. The averaged version of the momentum equations ([Equation 3.14](#)) take the name of Reynolds Averaged Navier-Stokes equations (RANS) with Favre averaging. It is immediately noticeable that the averaging introduces the new term τ_{ij} , defined as follows:

$$\tau_{ij} = -\overline{\rho u_i'' u_j''} \quad (3.16)$$

This expression takes the name of Reynolds stress tensor: it consists of a symmetric matrix defined by six independant components which account for the macroscopic

transport of momentum at the turbulent scales. The Reynolds stress tensor introduces six new unknowns to the problem: modelling strategies should thus be implemented to close the system of equations.

3.3 Eddy-viscosity models

Eddy-viscosity model can be used for modelling the Reynolds stress tensor. The formulation is due to Boussinesq and it relates the Reynolds stress tensor to the time-averaged velocity gradients, as defined by the eddy-viscosity closure model:

$$-\overline{\rho u_i'' u_j''} = 2\mu_T S_{ij} - \frac{2}{3}\mu_T S_{kk}\delta_{ij} \quad (3.17)$$

where μ_T is the turbulent eddy viscosity and represents a local quantity of the flow (and not of the fluid) since it takes into account the transfer of momentum caused by turbulent eddies. The Boussinesq eddy-viscosity assumption is analogous to the Stokes hypothesis for laminar flow. Although of simple formulation, it involves assumptions which can limit the accuracy of the results provided by this turbulence model. As stated by Wallin and Johansson [18], eddy-viscosity models are good for modelling attached thin boundary layers and two-dimensional flows, while they show several limitations when either non-equilibrium flows, boundary layer separation or effects due to swirl, rotation and curvature are considered. The applicability of this simple model therefore seems to be limited to simple wall-bounded flows: highly swirling flows, like the ones developing inside centrifugal compressors, could not be predicted with good accuracy. For this reason, the fluid dynamics community has developed a number of advanced turbulence models for aeronautical and turbomachinery flows: these models account for the deficiencies in the standard methods by adding terms for correcting the governing equations. Such models, in detail, have been developed to improve the accuracy of the prediction of separation.

3.3.1 Menter SST $K - \omega$ model

Amongst all choices available for solving RANS equations with eddy-viscosity models, the most popular one involves the solution of two transport equations for computation of the turbulence. Among these, the $K - \omega$ turbulence model, developed for the first time by Wilcox, represents nowadays one of the most used turbulence models in industrial research. In principle, it models the turbulence by means of transport equations for the turbulence kinetic energy $K = \overline{u_i'' u_i''}/2$ and the specific dissipation rate ω . The resulting $K - \omega$ model takes the following form:

$$\left(\frac{\partial}{\partial t} + \bar{u}_i \frac{\partial}{\partial x_j} \right) K = P - C_\mu K \omega + \frac{\partial}{\partial x_j} \left[\left(\nu + \frac{\nu_T}{\sigma_K} \right) \frac{\partial K}{\partial x_j} \right] \quad (3.18)$$

$$\left(\frac{\partial}{\partial t} + \bar{u}_i \frac{\partial}{\partial x_j}\right) \omega = \left((C_{\epsilon 1} - 1) \frac{\omega}{K}\right) P - (C_{\omega 2} - 1) C_{\mu} \omega^2 + \frac{\partial}{\partial x_j} \left[\left(\nu + \frac{\nu_T}{\sigma_{\omega}}\right) \frac{\partial \omega}{\partial x_j} \right] \quad (3.19)$$

where C_{μ} , σ_K , $C_{\epsilon 1}$ and $C_{\omega 2}$ are modelling coefficients calibrated experimentally whose values are reported in [18]. Turbulent viscosity is here defined as $\nu_T = K/\omega$, while production of turbulent kinetic energy P and specific dissipation rate ω are defined as follows:

$$P = -\overline{u'_i u'_j} \frac{\partial \bar{u}_i}{\partial x_j} = 2\nu_T S_{ij} S_{ij} \quad (3.20)$$

$$\omega = \frac{\nu}{C_{\mu} K} \overline{\frac{\partial u'_i}{\partial x_j} \frac{\partial u'_i}{\partial x_j}} \quad (3.21)$$

Compared to other two-equations turbulence models such as the $K - \epsilon$ one, the $K - \omega$ model shows some advantages. First of all, it provides better predictions of the boundary layer flows with pressure gradients. Furthermore, unlike $K - \epsilon$ equations which become singular at the wall and are not valid in the very near-wall region unless computationally expensive low- Re formulations are introduced, $K - \omega$ ones can be integrated to the wall also with small grid spacing ($y^+ \sim 1$). The main problem of this method is the treatment of turbulent interfaces, and in particular of the boundary layer edge, which results in an unphysical sensitivity to the free-stream values of K and ω . In addition, the onset and the amount of flow separation under adverse pressure gradients is not well predicted.

To solve these problem, Menter [19] developed the Shear-Stress-Transport (SST) $K - \omega$ model, which corrects the deficiencies of the standard $K - \omega$ model through the addition of cross-diffusion terms and production limiters into the formulation of the eddy-viscosity. Furthermore, the SST formulation allows to switch to a $K - \epsilon$ formulation in the free-stream: the latter, in fact, is proved to be less sensitive to inlet free-stream turbulence properties; $K - \omega$ model is instead used to solve the boundary layer. Due to its ability to catch flow separation, this model has been adopted for this thesis work.

3.3.2 Turbulent boundary layer

As discussed in section 2.2, Reynolds number for flows inside automotive centrifugal compressors is of the order of $10^6 \div 10^7$. This implies highly turbulent flows with the developement of turbulent boundary layers over the walls. Due to the higher slope of the velocity profile at the wall, turbulent boundary layers are accompanied by higher values of wall shear stress τ_w than laminar ones. Nevertheless, the structure of the turbulent boundary layer shows a high degree of complexity. In order to study it, a set of non-dimensional parameters is introduced: these are, namely,

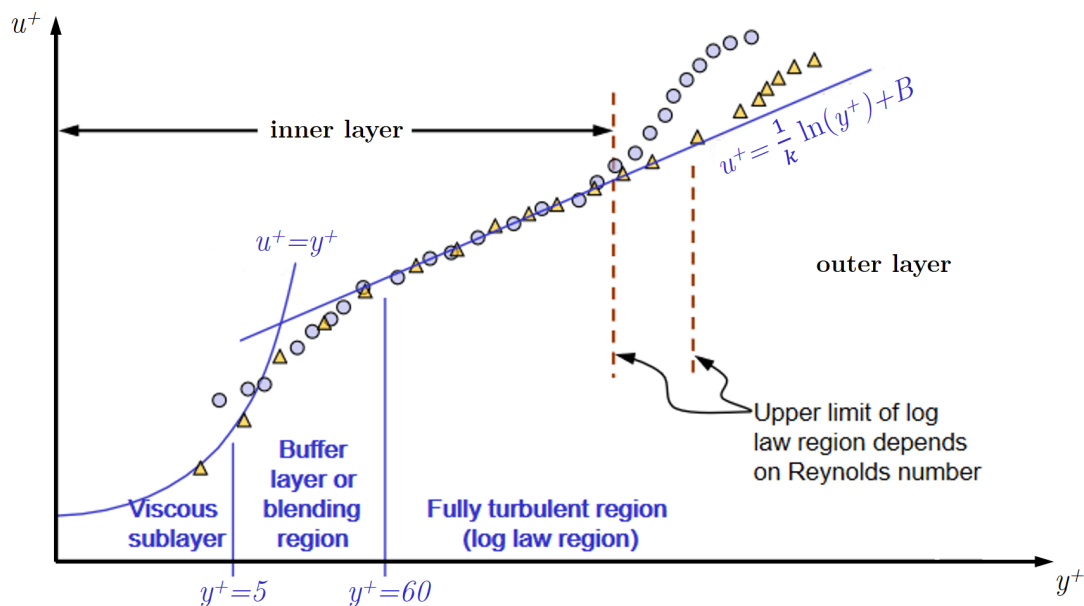


Figure 3.1: Law of the wall for turbulent boundary layers. Adapted from Ref.[20].

the non-dimensional length scale $y^+ = yu_\tau/\nu$, where y identifies the coordinate normal to the wall and $u_\tau = \sqrt{\tau_w/\rho}$, and the non-dimensional velocity scale $u^+ = u/u_\tau$. The graph of Figure 3.1 shows the dependency between u^+ and y^+ along the normal to the wall. Different regions can be identified. The closest layer to the no-slip wall is called viscous sublayer and it extends within the range $0 \leq y^+ < 5$. In this region, the absolute magnitude of the turbulent fluctuations is small while viscosity is predominant. Moreover, the relation $u^+ = y^+$ holds in this region. Flow characteristics in this region are very hard to capture both experimentally and from a numerical point since a very fine near-wall grid is required.

Between $y^+ \sim 50$ and $y/\delta < 0.15$ (where δ identifies the height of the boundary layer), the log-law region can be found. In this region, the law-of-the-wall holds:

$$u^+ = \frac{1}{\kappa} \log y^+ + B \quad (3.22)$$

where κ is the von Karman constant and B is an empirical coefficient.

The region extending between the viscous sublayer and the log-law region is the buffer layer. In this region, the maximum streamwise turbulent intensity and the maximum turbulence production can be measured.

Outside the log-law region, i.e. for $y/\delta > 0.15$, any streamwise velocity is mixed out with the free-stream velocity. This area is the so-called wake-region and it extends from 15% of the boundary layer thickness to the edge with the bulk flow.

3.4 Ansys CFX

Ansys CFX is used in this thesis to perform both steady-state and transient CFD simulations. The choice fell on this CFD package since it is suitable to model turbomachinery flows and can easily deal with rotating domains. The entire process, from the definition of the geometry to the data post-processing, can be directly managed from Ansys Workbench. In particular, the Parameter set window of Ansys Workbench allows to set up all simulations by easily changing the boundary condition: this tool becomes particularly useful when running steady-state simulations for calculation of the compressor map.

The typical workflow followed in Ansys CFX is depicted in [Figure 3.2](#). The first step involves the generation of the geometry in Design Modeler: CAD geometries are here imported and modified. The final design is then sent to Ansys Meshing for the generation of the computational grid. Once the mesh has been generated, the simulation can be set up in CFX-Pre: boundary/initial conditions, flow characteristics and all parameters affecting the outcome of the simulation can be here defined. CFX-Pre produces a `.def` file as output, which is then used by CFX Solver for the calculations. The latter performs all calculations and solves the flow field numerically: residuals and specific physical quantities defined in CFX-Pre can be monitored during the progress of the simulation. Finally, results can be visualized and analyzed in CFD-Post: basic post-processing tools are also available.



Figure 3.2: Workflow and software packages utilized for a CFD simulation in Ansys CFX.

Ansys CFX solver uses a finite volume method for spatial discretization: the definition of a computational mesh is thus required. The grid is used to construct finite volumes, which are used to conserve relevant quantities such as mass, momentum, and energy. For the following discussion we will refer to Ansys CFX documentation (Ref. [\[21\]](#)).

3.4.1 Finite Volume method (FVM)

Analytical solutions to the Navier-Stokes equations exist for only the simplest of flows under ideal conditions. To obtain solutions for real flows, a numerical approach must be adopted whereby the equations are replaced by algebraic approximations that can be solved using a numerical method. For simplicity, the following discussion will be limited to the two-dimensional case, but the drawn conclusions can be extended also to the 3D case.

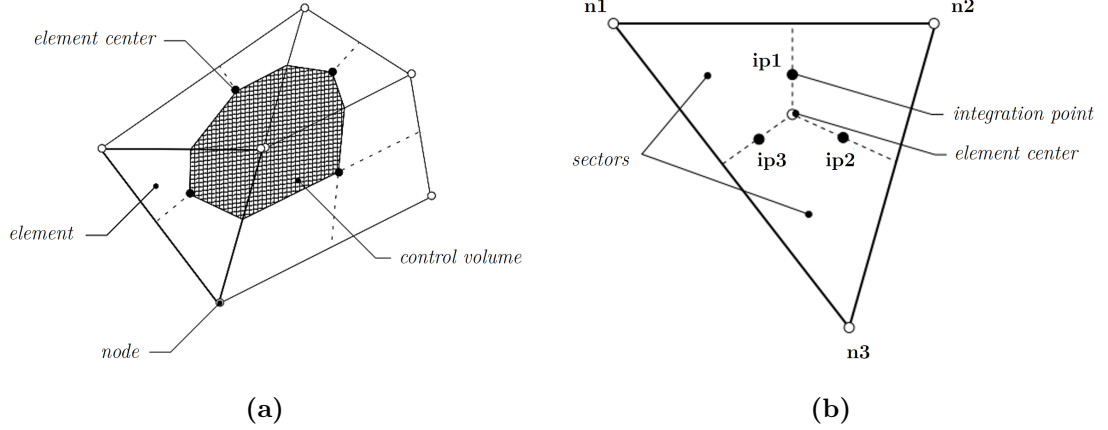


Figure 3.3: (a): structure of a 2D control volume; (b): nomenclature of important locations within a mesh cell. Adapted from Ansys CFX documentation (Ref. [21]).

Figure 3.3a shows a typical two-dimensional mesh. All solution variables and fluid properties are stored at the nodes (mesh vertices). A control volume (the shaded area) is constructed around each mesh node using the median dual (defined by lines joining the centers of the edges and element centers surrounding the node).

Governing equations of section 3.1 are integrated over each control volume, and Gauss' Divergence theorem is applied to convert volume integrals involving divergence and gradient operators to surface integrals. If control volumes do not deform in time, then the time derivatives can be moved outside of the volume integrals and the integrated equations become:

$$\frac{d}{dt} \int_V \rho dV + \int_s \rho u_j dn_j = 0 \quad (3.23)$$

$$\frac{d}{dt} \int_V \rho u_i dV + \int_s \rho u_i u_j dn_j = - \int_s p dn_j + \int_s \mu_{eff} \left(\frac{\partial u_i}{\partial x_j} + \frac{\partial u_j}{\partial x_i} \right) dn_j + \int_V S_{u_i} dV \quad (3.24)$$

$$\frac{d}{dt} \int_V \rho \phi dV + \int_s \rho u_j \phi dn_j = \int_s \Gamma_{eff} \left(\frac{\partial \phi}{\partial x_j} \right) dn_j + \int_V S_\phi dV \quad (3.25)$$

where V and s respectively denote volume and surface regions of integration, dn_j are the differential Cartesian components of the outward normal surface vector, S_{u_i} and S_ϕ are the source terms. μ_{eff} and Γ_{eff} are the so-called effective viscosity and diffusivity: in principle, they can be seen as a correction of the coefficients μ and Γ for turbulent flows. Equation 3.25 defines the conservation of a passive scalar, i.e. a scalar quantity whose variation does not produce any change in flow density, and replaces the energy equation. The volume integrals represent source or accumulation terms, and the surface integrals represent the summation of the fluxes.

The next step in the numerical algorithm is to discretize the volume and surface integrals. To illustrate this step, consider a single element like the one shown below. Volume integrals are discretized within each element sector and accumulated to the control volume to which the sector belongs. Surface integrals are discretized at the integration points (ipn) located at the center of each surface segment within an element and then distributed to the adjacent control volumes. Because the surface integrals are equal and opposite for control volumes adjacent to the integration points, the surface integrals are guaranteed to be locally conservative. After discretizing the volume and surface integrals, the integral equations become:

$$V \left(\frac{\rho - \rho^0}{\Delta t} \right) + \sum_{ip} \dot{m}_{ip} = 0 \quad (3.26)$$

$$V \left(\frac{\rho u_i - \rho^0 u_i^0}{\Delta t} \right) + \sum_{ip} \dot{m}_{ip} (u_i)_{ip} = \sum_{ip} (p \Delta n_i)_{ip} + \sum_{ip} \left(\mu_{eff} \left(\frac{\partial u_i}{\partial x_j} + \frac{\partial u_j}{\partial x_i} \right) \Delta n_j \right)_{ip} + \overline{S}_{u_i} V \quad (3.27)$$

$$V \left(\frac{\rho \phi - \rho^{n-1} \phi^{n-1}}{\Delta t} \right) + \sum_{ip} \dot{m}_{ip} \phi_{ip} = \sum_{ip} \left(\Gamma_{eff} \frac{\partial \phi}{\partial x_j} \Delta n_j \right)_{ip} + \overline{S}_{\phi} V \quad (3.28)$$

where $\dot{m}_{ip} = (\rho u_j \Delta n_j)_{ip}$, V is the control volume, Δt is the time step, Δn_j is the discrete outward surface vector, the subscript ip denotes evaluation at an integration point, summations are over all the integration points of the control volume, and the superscript $n - 1$ refers to the old time level. Even though second order schemes are preferable, a First Order Backward Euler scheme has been implemented in these equations.

Solution fields and other properties are stored at the mesh nodes. However, to evaluate many of the terms, the solution field or solution gradients must be approximated at integration points. Ansys CFX uses finite-element shape functions to perform these approximations. Finite-element shape functions describe the variation of a variable ϕ varies within an element as follows:

$$\phi = \sum_{i=1}^{N_{node}} N_i \phi_i \quad (3.29)$$

where N_i is the shape function for node i , N_{node} is the total number of nodes within the element and ϕ_i is the value of ϕ at node i . The sum of all N_i at each node must be equal to zero. Furthermore, at each node j , the relation $N_i = 1$ if $i = j$, $N_i = 0$ otherwise must hold. Depending on the type of mesh element, the shape functions can be defined in different ways. For this thesis work, only tetrahedral elements (4 nodes, 3 faces) will be utilized.

Discretization of the advection terms

The advection term requires the integration point values of ϕ to be approximated in terms of the nodal values of ϕ . The advection schemes implemented in Ansys CFX can be described by the following expression:

$$\phi_{ip} = \phi_{up} + \beta \nabla \phi \cdot \Delta \vec{r} \quad (3.30)$$

where ϕ_{up} is the value at the upwind node, and \vec{r} is the vector from the upwind node to the ip . Control volume gradients $\nabla \phi$ are discretized through the following formula:

$$\nabla \phi = \frac{1}{V} \sum_{ip} (\phi \Delta \vec{n})_{ip} \quad (3.31)$$

where $\Delta \vec{n}$ is the outward surface vector at ip and ϕ are evaluated at integration points by means of [Equation 3.29](#).

For $\beta = 0$, the first-order upwind scheme is obtained. Although very robust, this scheme introduces diffusive discretization errors that tend to smear steep spatial gradients. In light of this, the quantity $\beta \nabla \phi \cdot \Delta \vec{r}$ is the so-called numerical advection correction and it can be seen as a correction for the excessive diffusivity of the upwind scheme. By choosing a value for β between 0 and 1, and by setting $\nabla \phi$ equal to the average of the adjacent nodal gradients, the discretization errors associated with the upwind scheme are reduced. The choice $\beta = 1$ is formally second-order-accurate in space, and the resulting discretization will more accurately reproduce steep spatial gradients than first-order upwind schemes. Nevertheless, it may introduce dispersive discretization errors that tend to cause non-physical oscillations in regions of rapid solution variation.

In order to reduce as much as possible diffusive and dispersive errors, a high-resolution scheme is implemented in Ansys CFX. This scheme uses a special non-linear recipe for β at each node, computed to be as close to 1 as possible without introducing new extrema. The advective flux is then evaluated using the values of β and $\nabla \phi$ from the upwind node. The methodology for β involves first computing a ϕ_{min} and ϕ_{max} at each node using a stencil involving adjacent nodes (including the node itself). Next, for each integration point around the node, the following equation is solved for β to ensure that it does not undershoot ϕ_{min} or overshoot ϕ_{max} . The nodal value for β is taken to be the minimum value of all integration point values surrounding the node. The maximum value of β should not exceed 1.

Discretization of transient terms

First order backward Euler schemes for time discretization have already been used for defining [Equation 3.4.1](#) and [Equation 3.28](#). This scheme is implicit and does not show any limitation in the time step size Δt , but it is only first-order accurate.

In addition, discretization errors lead to an increase in numerical diffusion. Due to these limitations, the use of second order backward Euler schemes is usually suggested. With regards to the first term of Equation 3.28, the resulting implicit-time discretization is:

$$\frac{\partial}{\partial t} \int_V \rho \phi dV \approx V \frac{1}{\Delta t} \left[\frac{3}{2} (\rho \phi)^n - 2 (\rho \phi)^{n-1} + \frac{1}{2} (\rho \phi)^{n-2} \right] \quad (3.32)$$

where n identifies the current time step and $n - 1$, $n - 2$ the preceding ones. Compared to the first order scheme, this one is second-order accurate in time. Nonphysical oscillations, however, can be noticed in the solution for some cases: corrections to the scheme are however available in Ansys CFX.

3.4.2 Discretization errors

Discretization errors give an indication of the mismatch between the exact analytical solution of the governing equations and the one provided by their discretized approximations. The sources of errors can be different and will be analyzed extensively in the following paragraphs.

Solution errors

Solution errors are a measure of the difference between the exact mathematical solution and the one provided by the numerical simulation. In terms of relative error \hat{E}_S , these can be defined as follows:

$$\hat{E}_S = \frac{\|f_{exact} - f_{numeric}\|}{\|f_{exact}\|} \quad (3.33)$$

where f is used in this section to identify the solution. Low values of \hat{E}_S assure a more accurate numerical solution.

Reducing solution errors is not a straightforward task because, apart for some very simple cases, the exact solution cannot be calculated and the computation of \hat{E}_S becomes very complex. The exact solution can be linked to the numerical one through a Taylor expansion, as here reported:

$$f_{numeric} = f_{exact} + c\Delta x^p + d\Delta t^q + h.o.t. \quad (3.34)$$

where Δx and Δt are respectively the grid and time spacing, p and q are the truncation error orders of the methods adopted for both space and time discretization and the abbreviation *h.o.t* stands for higher order terms. In other words, the numerical solution converges to the exact solution with the power of Δx and Δt .

Errors are also introduced when analytical derivatives or integrals in space and time are replaced by numerical approximations. For these cases, the truncation error

can be calculated by means of a Taylor series expansion: the order of the discretization scheme is then determined by the lowest order of the truncation error after all terms have been discretized. For example, with regards to a central-difference discretization for spatial derivatives, one can obtain:

$$\left. \frac{\partial f}{\partial x} \right|_{\text{numerical}} = \left. \frac{\partial f}{\partial x} \right|_{\text{exact}} + o(\Delta x^2) \quad (3.35)$$

which results in a second order scheme in space. The lowest order term in $o(\Delta x^2)$ is proportional to $f^{(3)}\Delta x^2$ and contributes to numerical diffusion.

Iteration errors

Iterative convergence errors are a consequence of the stopping of the numerical iterations to reduce the computational effort done by the solver. The errors are supposed to decrease progressively throughout the duration of the simulation and fall below a well-defined boundary.

Iteration errors are usually quantified by the root-mean square (RMS) of the residuals. In Ansys CFX, residual are nondimensionalized to enable a comparison amongst the different governing equations and plotted as an output result of the simulation.

Round-off errors

Round-off errors result from the fact that a computer utilizes floating-point arithmetic for calculations. In addition, due to the limited number of digits used for the numerical representation of the numbers, the computer cannot differentiate between numbers that are different by an amount below the available accuracy. For flow simulations with large-scale differences this can lead to problems for single-precision (8-digits) simulations. Round-off errors are often characterized by a random behavior of the numerical solution [22].

3.4.3 Courant number

The Courant number is of fundamental importance for transient flows. For a one-dimensional grid, it is defined by:

$$Co = \frac{u\Delta t}{\Delta x} \quad (3.36)$$

where u is the local fluid speed, Δt is the timestep and Δx is the mesh size. On commercial CFD codes, the implemented Courant number is a multidimensional generalization of Equation 3.36 where the velocity and length scale are based on the mass flow into the control volume and the dimension of the control volume.

For explicit CFD methods, the timestep must be chosen such that the Courant number is sufficiently small ($Co \sim 1$), otherwise the method would be unstable and the numerical solution would diverge. Implicit schemes, like the ones available in Ansys CFX, do not require the Courant number to be small for stability. However, for some transient calculations, one may need the Courant number to be small in order to accurately resolve transient details.

Chapter 4

Geometries and meshing strategies

The two compressors utilized throughout the thesis are introduced and analyzed in this chapter. The differences between each design and their peculiarities are extensively discussed. The chapter then proceeds with the analysis of the meshes implemented on both compressors. A grid independence study was conducted in order to identify the optimal mesh size. Finally, domains and interfaces of the compressors are introduced: the differences among the interface models available in Ansys CFX is also explained.

4.1 Compressor geometries

The thesis work is divided in two parts. For the first part, focused on performance analysis in terms of compressor map and efficiency, a reference CAD geometry for the compressor is used; the latter will be referred as HT compressor in the following sections, where the abbreviation HT stands for "heavy-truck". The STT "Scania" compressor is instead used for the analysis of the transient surge response. Both geometries are analyzed in the following paragraphs.

4.1.1 HT compressor

The isometric view of the HT compressor is shown in [Figure 4.1](#). The illustrated rendering refers to the CAD geometry utilized for the CFD analysis: it differs from the actual one with regards to the inlet and outlet pipes which, in the actual configuration, are bent in order to facilitate the housing inside the engine compartment. The most important locations, i.e. inlet, outlet and the components introduced in [chapter 2](#), are indicated with labels. Additional views on the XZ and XY plane are also shown in [Figure 4.2](#). In the following, the XZ plane will be referred to as the meridional plane of the compressor. The convention for the angular tangential direction θ is also shown in [Figure 4.2b](#).

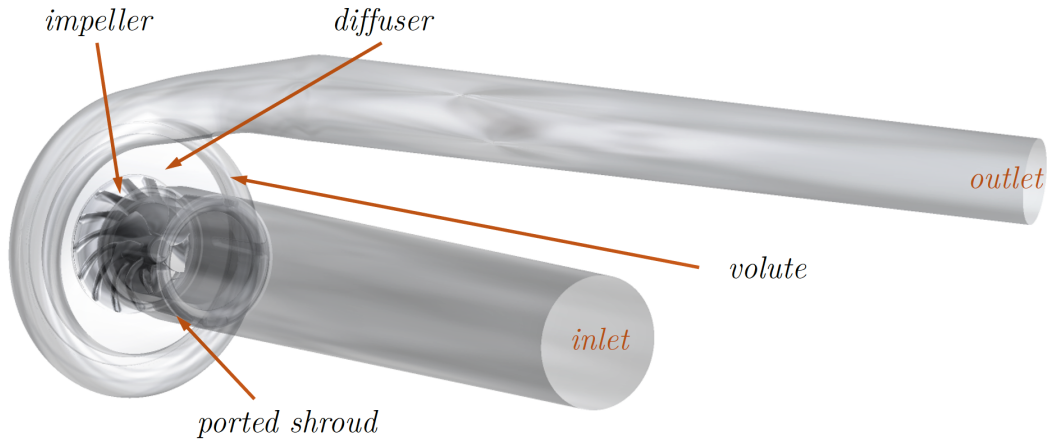


Figure 4.1: View of the HT compressor.

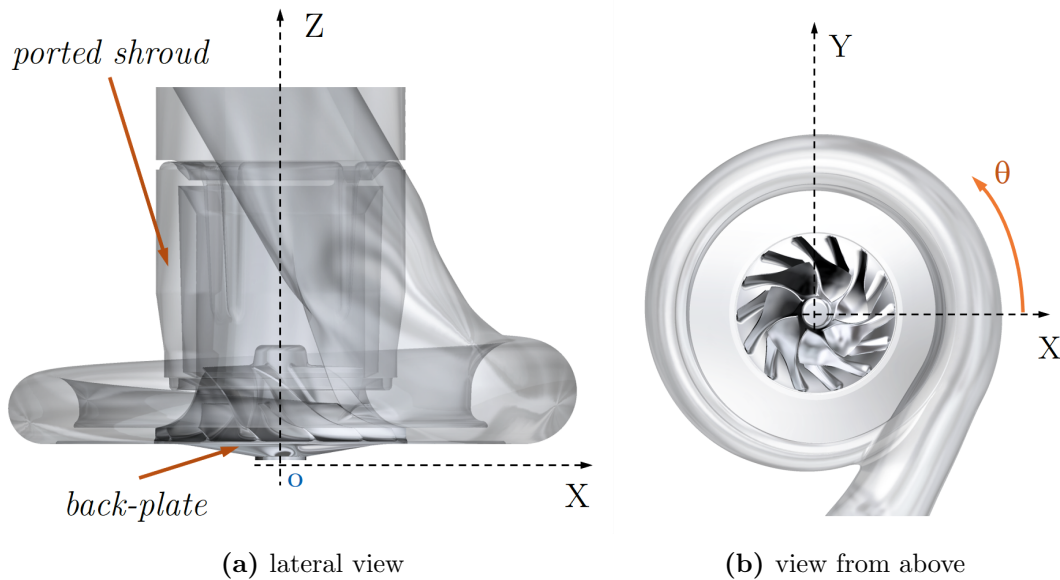


Figure 4.2: Views of the HT compressor and conventions for axes and angular distances.

In order to both avoid boundary effects, inlet and outlet have been extruded of 8 pipe diameters. With these extrusions, it is possible to run simulations at deep surge regimes because the backflow does not reach the inlet section.

The impeller consists of 7 main backswept blades equally distributed along the circumference of the hub; 7 smaller splitter blades are inserted between each blade vane. The leading edge of each blade is backswept in order to better guide the flow along the vanes.

The height of the diffuser is kept constant along its radius. The radius of the

volute pipe increases almost linearly from the tongue to the volute outlet, i.e. in proximity of the slight bend of the outlet pipe.

Figure 4.2a highlights the presence of the so-called back-plate. The back-plate is the stationary wall underneath the impeller; it extends from the wheel hub to the lower wall of the diffuser. The cavity between the lower face of the impeller and the back-plate allows recirculation of a small amount of fluid. This cavity therefore represents a huge source of friction losses due to the high velocity gradient that the flow encounters (no-slip condition at both stationary and rotating walls and high rotational speed of the impeller): it is therefore possible to measure the highest values of temperature in proximity of the back-plate.

Ported shroud

The HT compressor is equipped with a ported shroud cavity, as highlighted in Figure 4.2a. The implementation of a ported shroud cavity for flow-recirculation, already introduced in subsection 2.5.2, is widely used on turbochargers to improve compressor performance at low mass-flow rates and mitigate the effects of surge. This improvement is achieved by means of an enhancement of the aerodynamic stability of the compressor.

The ported shroud design has been proposed for the first time by Fisher [23] in 1988. The design is quite simple: a small cavity is hollowed out in the compressor shroud in proximity of the blade leading edge; the cavity proceeds upstream for several centimeters and it then reunites with the inlet pipe. The benefits of such configuration are multiple:

- the flow separated from the blade surfaces is recirculated into the ported shroud cavity. The blockage over the blade vanes induced by the separated flow is thus reduced;
- at deep surge regimes, the ported shroud cavity allows the recirculation of the backflow in the inlet pipe along the mainstream direction. The recirculation is driven by the favorable pressure gradient encountered by the flow along the cavity.
- compressor performance are enhanced also in proximity of the choke line. The ported shroud cavity, in fact, allows part of the flow to bypass the aerodynamic throat arising in proximity of the inducer [24];

The overall result is an extension of the operational field of the compressor: according to Semlitsch *et al* [17] which used LES simulations for their analysis, both surge and choke lines are shifted towards lower and higher mass flows respectively. A qualitative study of the removal of the ported shroud cavity in the HT compressor can be found in Appendix A.

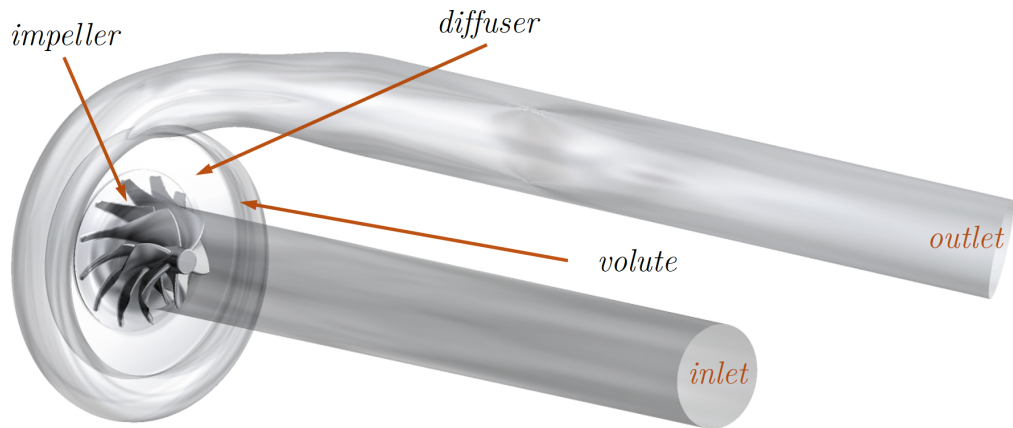


Figure 4.3: View of the Scania compressor.

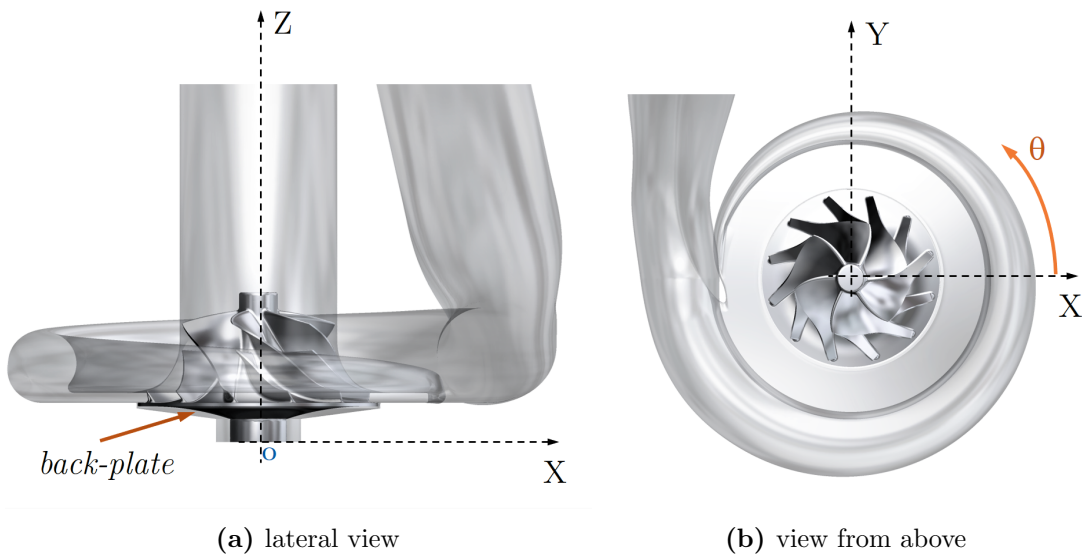


Figure 4.4: Views of the Scania compressor and conventions for axes and angular distances.

Although representing a very simple design, ported shroud compressor covers show some drawbacks that have limited their application: many of the automotive compressors, in fact, typically operate outside of the region where ported shroud benefits can be appreciated. In addition, they can cause a slight efficiency penalization and an increased noise when surge is approaching, as reported by Dehner *et al* [25].

4.1.2 STT ”Scania” compressor

The STT compressor (nicknamed ”Scania” compressor in the following) is shown in [Figure 4.3](#). Different views of the compressor are shown in [Figure 4.4](#). The geometry is quite similar to the HT one: also for this geometry both inlet and outlet have been extruded of 8 pipe diameters.

The impeller consists of 6 main blades and 6 splitter blades: each blade is back-swept at the inducer to better guide the flow along the blade vanes. The blades are also backswept in proximity of the exducer.

The Scania compressor is not provided with a ported shroud in its original configuration. This design will be modified in [chapter 6](#) with the addition of a parametric ported shroud cavity in order to find the best design in terms of surge response.

4.2 Mesh

The computational grids developed for both compressors are shown in [Figure 4.5](#) (HT compressor) and [Figure 4.6](#) (Scania compressor). In both cases, an unstructured mesh is implemented for the numerical discretization of the computational domain. Tetrahedrons are used for discretizing the domain: the implementation of such element shape is recommended when dealing with complex 3D geometries because it assures better mesh quality and easier transitioning between coarser and finer grid resolutions. Aligned prism elements, instead, are utilized to build the boundary layer mesh in proximity of the walls. The boundary layer evolution is monitored by five layers of aligned prism cells whose height increases gradually from the wall to the free-stream mesh; the height of the first cell is set to 10^{-5} m on both compressors.

In order to fulfill mesh quality requirements, local refinements are introduced in complex geometrical areas such as sharp corners at the blade tips. Mesh quality parameters [\[26\]](#) for both the two computational grids are reported in [Table 4.1](#). These are, respectively:

- aspect ratio (AR): it takes into account the stretching of the mesh elements. It is computed as the ratio of the maximum to minimum integration point surface areas in all elements. Nodal values are calculated as the maximum of all element aspect ratios that are adjacent to the node. According to Ansys documentation [\[26\]](#), acceptable values of aspect ratio fall in the range $1 \div 100$.
- skewness: it is an indicator of how close to ideal (i.e. equilateral or cubic cells) a face or cell is. It is computed as the maximum between the Equilateral-Volume-Based Skewness (*EVBS*):

$$EVBS = \frac{\text{optimal cell size} - \text{cell size}}{\text{optimal cell size}} \quad (4.1)$$

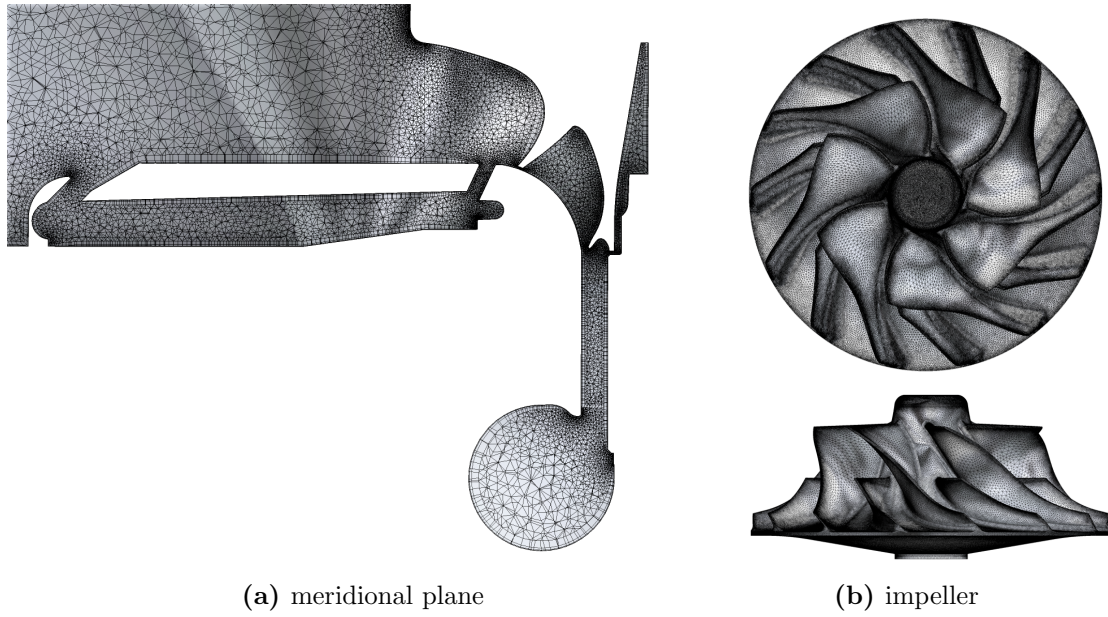


Figure 4.5: Computational grid developed for the HT compressor. On the right, detail of the impeller mesh.

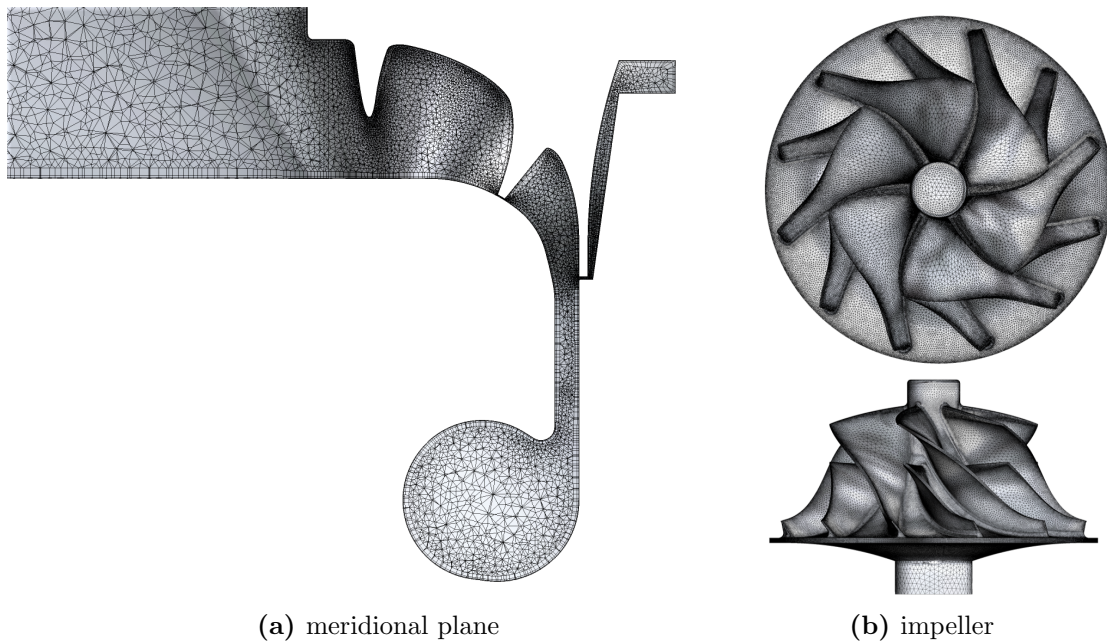


Figure 4.6: Computational grid developed for the Scania compressor. On the right, detail of the impeller mesh.

where the optimal cell size represents the size of an equilateral cell with the same characteristic length, and the Normalized Equiangular Skewness (NES):

$$NES = \max \left[\frac{\theta_{max} - \theta_e}{180^\circ - \theta_e}, \frac{\theta_e - \theta_{min}}{\theta_e} \right] \quad (4.2)$$

where θ_{max} , θ_{min} and θ_e are respectively the largest and the smallest angle in the cell and the angle of the corresponding equiangular cell.

In general, acceptable values for the 3D cells fall in the range $0 \div 0.5$, but higher local values (< 0.95) can be accepted over few cells .

Concerning the Scania compressor mesh, all quality indicators fall below the reported boundaries for the majority of cells. Due to the high geometrical complexity and the presence of a boundary layer inflation, some highly skewed cells are noticeable: the maximum skewness is, however, lower than 0.95. The latter parameter is slightly higher on the HT compressor due to the higher complexity introduced by the ported shroud. All elements whose skewness is > 0.9 , in fact, are located in proximity of the small protrusion located on the lowest part of the ported shroud cavity: very little flow, however, recirculates in this area and its contribution to the final results is totally negligible. All these considerations lead to a mesh size of approximately 43 millions cells for the HT compressor and 14 millions for the Scania one. A further drop of the cell count could be possible with a structured mesh: Scania CV AB tradition and experience, however, suggest that excellent results can be obtained within reasonable computational time also with the adoption of unstructured grids.

Table 4.1: Aspect ratio and skewness values for the Scania compressor mesh

| | HT compressor | | Scania compressor | |
|---------------|---------------|---------------------|-------------------|------------------------|
| | aspect ratio | skewness | aspect ratio | skewness |
| minimum | 1,16 | 2×10^{-11} | 1,16 | $2,634 \times 10^{-7}$ |
| maximum | 1482,9 | 0,93 | 992,5 | 0,8864 |
| average | 7,73 | 0,22 | 11,27 | 0,2142 |
| std deviation | 21,05 | 0,13 | 28,08 | 0,1251 |

Iterative convergence for both compressors is also analyzed: experience says that a four orders of magnitude decrease in the normalized residuals for each balance equation should at least be fulfilled [27]. For time-dependent problems, iterative convergence at every time step should also be checked, and sample convergence trends should be documented for selected, critically important, variables.

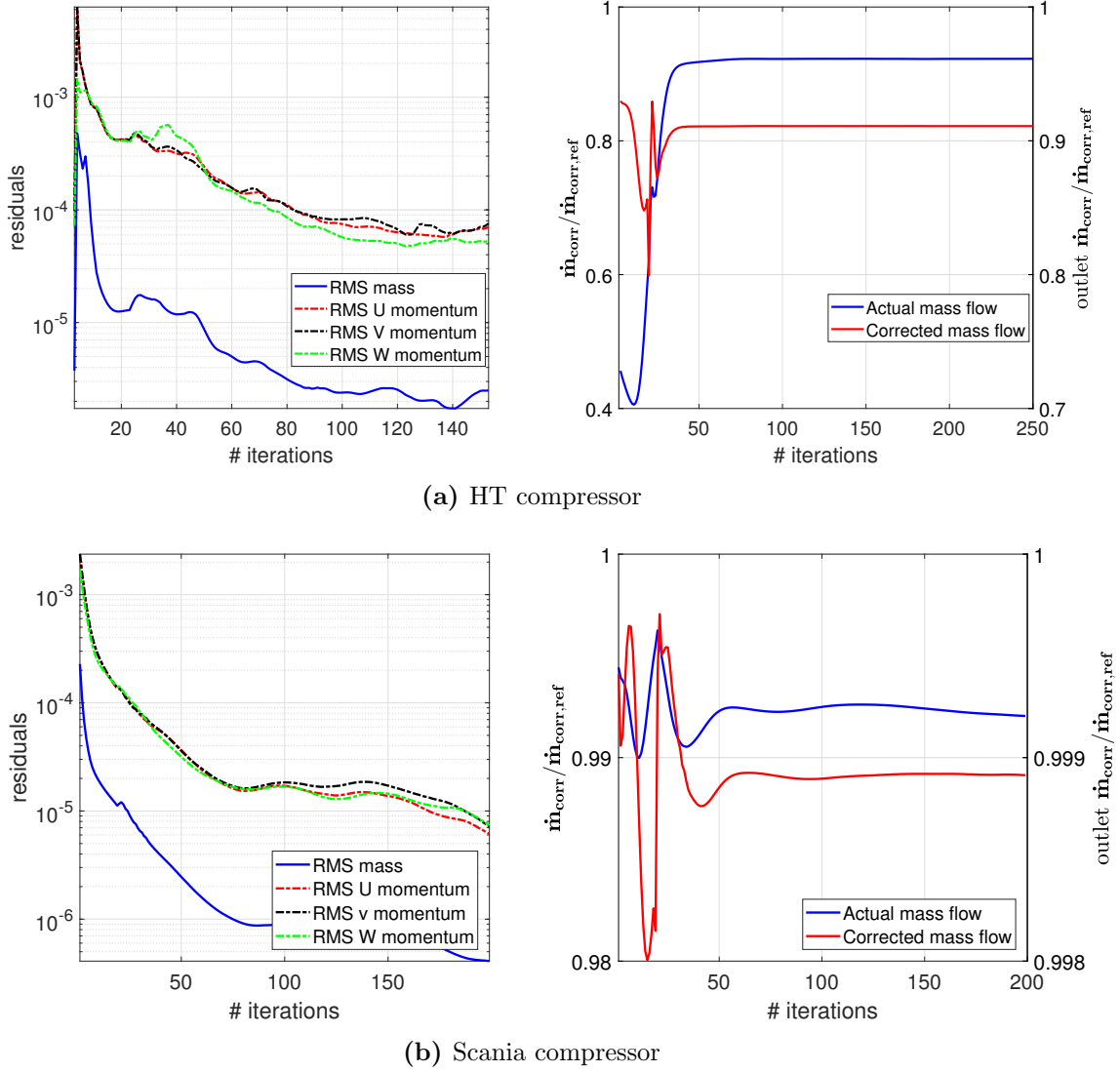


Figure 4.7: Residuals and variables evolution during the simulation.

Residuals of a steady state simulation run for both grids are shown in Figure 4.7, together with plots of corrected mass flow and outlet corrected mass flow¹. For both geometries, simulations are run at design conditions, i.e. 90000 RPM and

¹The outlet corrected mass flow is defined as:

$$\dot{m}_{corr,out} = \dot{m} \frac{\sqrt{T_{out}^0/T_{ref}}}{p_{out}^0/p_{ref}} \quad (4.3)$$

See chapter 5 for mor details.

$\dot{m}_{corr} = 0.2$ kg/s. RMS residuals drop below the tolerance limit of 10^{-4} with less than 100 iterations for both designs: convergence is particularly fast for the Scania compressor.

4.3 Grid independence study

In order to assess the correctness of the results that come out from the simulation, a mesh independence study is conducted on both compressors. The Scania compressor is not provided with a ported shroud: the original configuration is modified in [chapter 6](#) with the insertion of a parametric design of the ported shroud cavity. For sake of simplicity, however, the mesh independence study on this geometry will not take into account the ported shroud.

The strategy developed in this section starts with a comparison among the results provided by a set of meshes built over the same geometry but differing from each other with respect to the characteristic cell length and the overall grid size. The optimal compromise, in fact, requires meshes fine enough to accurately integrate the PDE over the whole domain, but also coarse enough to avoid an intolerable increase in computational resources required for the solution of the problem. See the literature for more details, e.g. [\[28\]\[29\]](#). Further investigations involve an assessment on the grid ability to capture the most relevant features in the flow and a comparison with relevant experimental data. This analysis will be the focus of the following [chapter 5](#).

Secondly, all the results produced by the different meshes are collected and analyzed in order to estimate an extrapolated "theoretical" solution in which $\Delta x \rightarrow 0$. The extrapolated solution is then compared with the numerical ones for evaluating the relative error and obtaining an approximation of the discretization error.

The adopted method for discretization error estimation is the Richardson extrapolation (RE) method. This method, after its first formulation, has been deeply investigated by mathematicians and engineers; its relevance for CFD makes it currently the most reliable method available for the prediction of numerical uncertainty.

For this analysis, the focus is only on steady state simulations. When dealing with transient simulations, instead, a change in cell size implies a change in the local Courant number: an appropriate time step should thus be selected to fulfill the CFL condition. This latter, however, becomes very strict only when explicit time discretizations are implemented ($Co < 1$ for 1D problems). On the other hand, Courant numbers higher than unity ensure numerical convergence for all implicit time discretizations [\[9\]](#).

4.3.1 Definition of the grids

The computational grid described in [section 4.2](#) is the result of a mesh convergence study. Three different meshes of different size are considered to extrapolate the "theoretical" solution with the Richardson methodology:

- medium mesh:
43 millions cells, $\Delta x_{av} = 5.768 \cdot 10^{-4}$ m for the HT compressor,
14 millions cells, $\Delta x_{av} = 6.476 \cdot 10^{-4}$ m for the Scania compressor
- coarse mesh:
17 millions cells, $\Delta x_{av} = 7.651 \cdot 10^{-4}$ m for the HT compressor,
4 millions cells, $\Delta x_{av} = 9.787 \cdot 10^{-4}$ m for the Scania compressor
- fine mesh:
63 millions cells, $\Delta x_{av} = 4.693 \cdot 10^{-4}$ m for the HT compressor,
40 millions cells, $\Delta x_{av} = 4.546 \cdot 10^{-4}$ m for the Scania compressor

where Δx_{av} indicates the characteristic cell length of the mesh and can be estimated through the following formula:

$$\Delta x_{av} = \left[\frac{1}{N} \sum_{i=1}^N (\Delta V_i) \right]^{\frac{1}{3}} \quad (4.4)$$

where ΔV_i is the volume of the i^{th} cell and N is the total number of cells used for the computations.

The higher mesh resolution for the HT compressor is mainly due to the presence of the ported shroud and the higher complexity of the impeller design. The experience suggests that the ratio between the representative cell size of coarse and fine mesh should be greater than 1.3 [30]: this condition is fully fulfilled by the setup here investigated ($\Delta x_{coarse} / \Delta x_{fine} = 2.15$). The different refinements are obtained by playing with both "Relevance Center" and "Relevance" options in Ansys Mesher. Boundary layer inflation settings and face sizings are the same for all three grids.

Different performance indicators are monitored in order to evaluate both robustness and accuracy of the results. In particular, the chosen parameters are: mass flow, total-to-static pressure ratio, total-to-static efficiency, total-to-total efficiency. The convergence of these variables to a stable value is a symptom of the decrease of the discretization error, i.e. more accurate results.

Together with the grids described in [subsection 4.3.1](#), additional meshes are considered: in particular, grids of 25 and 38 millions cells for the HT compressor and grids of 7 and 23 millions cells for the Scania compressor are also taken into account. Steady state simulations at near-design conditions, i.e. 90000 RPM and $\dot{m}_{corr} = 0.2$, are run for each mesh. Results are reported in [Figure 4.8](#) in function of the number of cells.

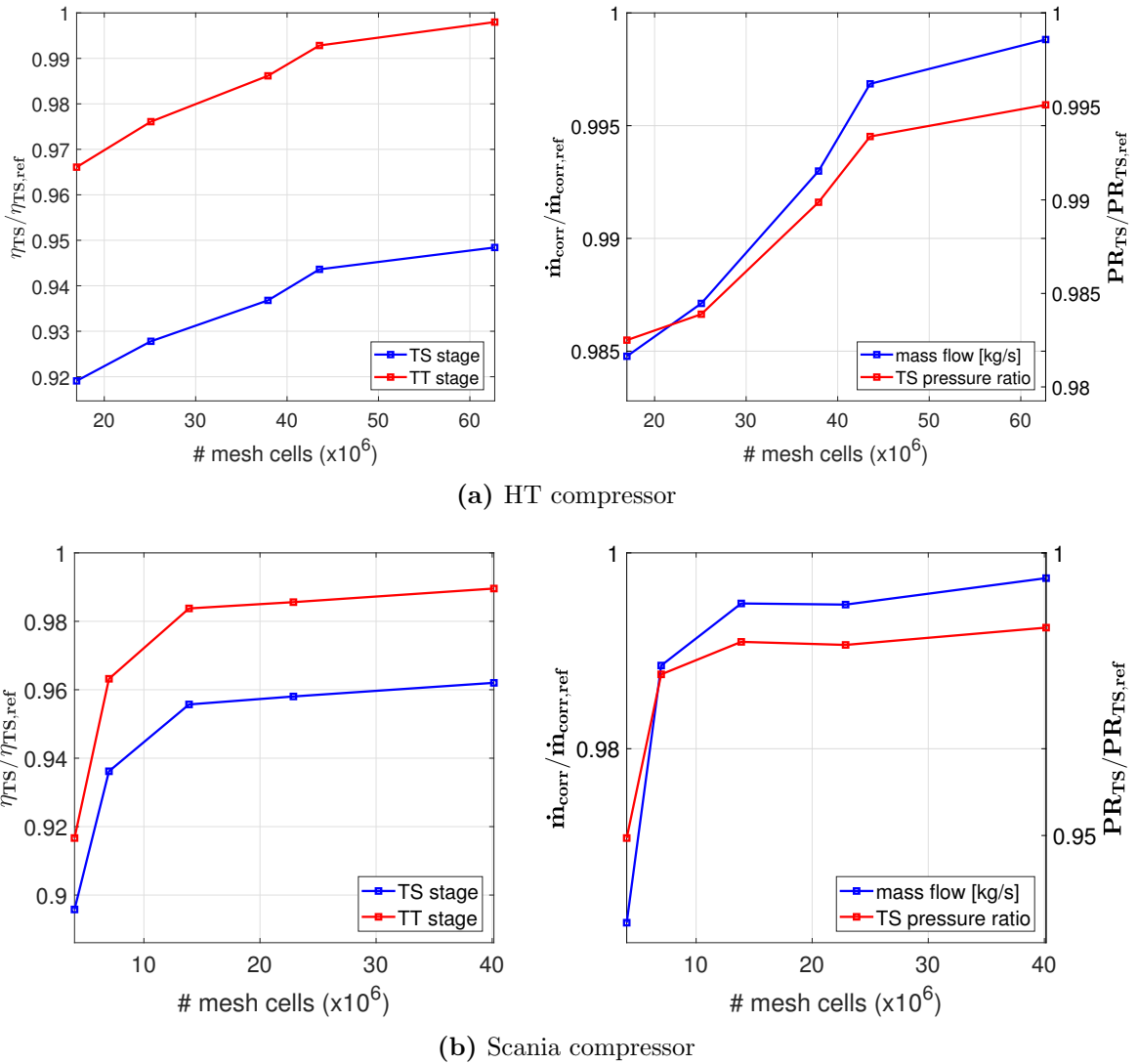


Figure 4.8: Mass flow and efficiency convergence with different grid refinements.

Both mass flow, pressure ratios and efficiencies reach an almost constant value with 43 million cells for the HT compressor mesh and 14 millions cells for the Scania one: such grid densities allow to correctly capture the flow evolution in the domain without drastically increase the amount of required computational resources. Variations at higher refinements are negligible (relative error $< 1\%$). The two meshes just obtained are the same ones introduced in [section 4.2](#) and the results that they provided will be compared in the following with the extrapolated "theoretical" ones.

4.3.2 Extrapolation of the solution

The Richardson extrapolation (RE) method is utilized for extrapolating a "correct" solution with the average length of the mesh cells equal to zero. The formal implementation of Richardson RE method to the CFD cases investigated here has been described by Celik *et al* [30]. The procedure is reported hereafter.

Let us denote with ϕ a critical variable for the problem under analysis. For a compressor device, ϕ could be either an integrated variable, like efficiency or pressure ratio, or a local variable, like Mach number or pressure. In the following paragraphs, subscripts 1,2 and 3 will denote respectively the fine, the medium and the coarse mesh. One can introduce the grid ratios $r_{21} = \Delta x_2/\Delta x_1$, $r_{32} = \Delta x_3/\Delta x_2$ and the relative errors $\epsilon_{32} = \phi_3 - \phi_2$, $\epsilon_{21} = \phi_2 - \phi_1$. The apparent order of the method can be calculated with the following fixed point iterative procedure:

$$p = \frac{1}{\ln(r_{21})} \left| \ln \left| \frac{\epsilon_{32}}{\epsilon_{21}} \right| + q(p) \right| \quad (4.5)$$

$$q(p) = \ln \left(\frac{r_{21}^p - s}{r_{32}^p - s} \right) \quad (4.6)$$

$$s = 1 \cdot \text{sign} \left(\frac{\epsilon_{32}}{\epsilon_{21}} \right) \quad (4.7)$$

where the initial guess is equal to the first term with $q(p) = 0$. The output value of p can be compared with the theoretical order of the mathematical method implemented in the solver. Absolute values are used to guarantee $p > 0$. Notice that negative values of $\epsilon_{32}/\epsilon_{21}$ are an indicator of oscillatory convergence, i.e. convergence plots of the ϕ functions like the ones reported in Figure 4.8 are not monotonic: when this happens, or when either ϵ_{32} or ϵ_{21} are very close to zero, the procedure fails. Once the apparent order p is obtained, the extrapolated values can be calculated as follows:

$$\phi_{ext} = \frac{r_{21}^p \phi_1 - \phi_2}{r_{21}^p - 1} \quad (4.8)$$

Error estimates can be calculated as well. The approximate relative error between two different grids is given by:

$$e_a^{ij} = \left| \frac{\phi_j - \phi_i}{\phi_j} \right| \quad (4.9)$$

The extrapolated relative error to the i^{th} grid is:

$$e_{ext}^i = \left| \frac{\phi_{ext} - \phi_i}{\phi_{ext}} \right| \quad (4.10)$$

where $i = 1,2,3$. Finally, the fine-grid convergence index GCI , used to estimate the uncertainty of the extrapolated results, can be computed through the following expression:

$$GCI_{fine}^{21} = \frac{1.25e_a^{21}}{r_{21}^p - 1} \quad (4.11)$$

where 1.25 is a safety factor on the error.

Table 4.2 shows the results of the extrapolation for corrected mass flow, pressure ratios and efficiencies, both total-to-static and total-to-total. Relative errors between different meshes drop proportionally to Δx^2 : doubling the grid size leads to a four-times decrease in the truncation error. Furthermore, Table 4.2 highlights that results computed through the "medium" mesh can be considered trustworthy ($e_a^{21} < 1\%$). e_{ext}^2 values, in fact, are below 1% for all the parameters under analysis. Reliability of both method and extrapolated solution is well assured by GCI indices. For both compressors, the highest GCI s are calculated for the total-to-static efficiency: these values, however, are smaller than the maximum extrapolated relative error evaluated on the same variable.

With regards to the Scania compressor only, Richardson extrapolation is performed also on local quantities. For this analysis, both pressure and Mach number are probed along a circumference positioned at 10% of the diffuser radius, i.e. in proximity of the impeller exit.

Measurements are plotted in Figure 4.9 for grid refinements. Extrapolated velocity and pressure profiles are reported as well, together with error bars: these latter report an indication of the local grid-convergence index GCI and provide a good feedback of the numerical uncertainty connected to the calculated solution.

Table 4.2: Relative errors and fine-grid convergence indices for the main performance parameters of the compressor. Efficiencies are calculated for the whole flow domain.

| HT compressor | | | | | |
|-------------------|------------------------|-----------|-----------|-------------|-------------|
| | \dot{m}_{out} [kg/s] | PR_{TS} | PR_{TT} | η_{TS} | η_{TT} |
| e_a^{21} | 0,20 % | 0,17 % | 0,16 % | 0,51 % | 0,52 % |
| e_a^{32} | 1,21 % | 1,10 % | 1,05 % | 2,60 % | 2,69 % |
| e_{ext}^2 | 0,28 % | 0,24 % | 0,23 % | 0,77 % | 0,77 % |
| GCI_{fine}^{21} | 0,10 % | 0,08 % | 0,08 % | 0,33 % | 0,33 % |
| Scania compressor | | | | | |
| | \dot{m}_{out} [kg/s] | PR_{TS} | PR_{TT} | η_{TS} | η_{TT} |
| e_a^{21} | 0,30 % | 0,32 % | 0,26 % | 0,69 % | 0,68 % |
| e_a^{32} | 3,23 % | 3,47 % | 2,91 % | 6,24 % | 6,73 % |
| e_{ext}^2 | 0,35 % | 0,36 % | 0,30 % | 0,82 % | 0,79 % |
| GCI_{fine}^{21} | 0,06 % | 0,06 % | 0,05 % | 0,16 % | 0,15 % |

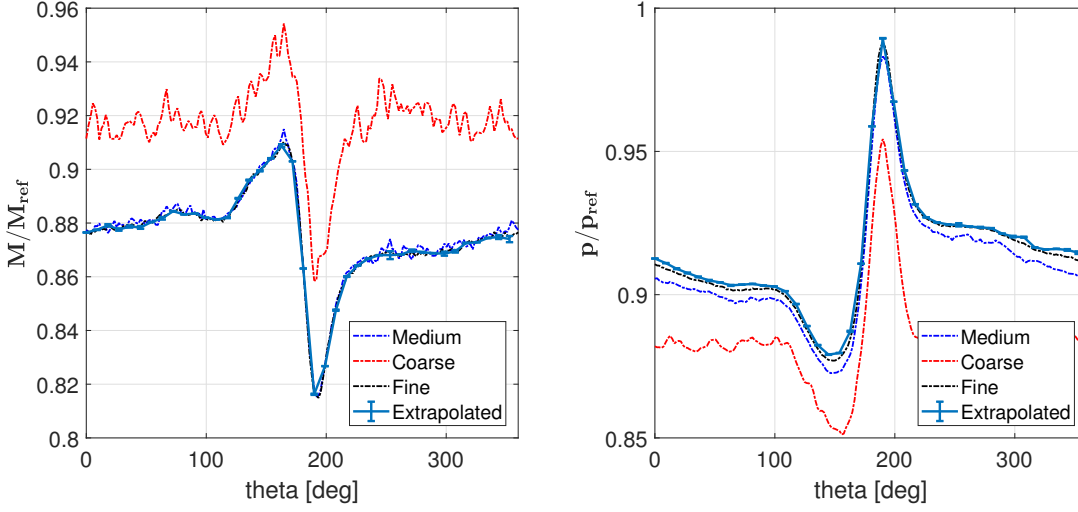


Figure 4.9: Mach and pressure profiles along the circumference at the diffuser exit. Results for grid at different refinement levels are plotted, together with the extrapolated solution and relative error bars.

Coarser meshes with less than 6 millions elements can not provide reliable results. Highly sparse grids, indeed, are not able to properly catch the flow evolution: the pressure recovery over the domain is consistently underestimated. The overall effect of this underestimation leads to lower efficiency and pressure ratio, as stated in [Table 4.2](#). On the other hand, coarser meshes could be used during the initial phases of the project for predicting worst case scenarios with low computational effort: performance predictions are underestimated and can thus be interpreted as conservative.

Not-excessive refinement, however, lead to reliable results: regarding medium and fine meshes, in fact, differences in both velocity and pressure profiles are so small that they can be neglected. It is also good to notice that the 14 millions elements grid is able to catch velocity fluctuations along the circumference with acceptable precision.

Richardson extrapolation procedure works only with monotonic ϕ functions. In addition, convergence must not show oscillations every time different grid refinements are considered. Conditions like these are usually fulfilled by integrated quantities, like efficiency or power, while local variables are more vulnerable to oscillations. The plots in [Figure 4.9](#) are examples of monotonic convergence: profiles converge asymptotically to the theoretical extrapolated solution with successive refinements. This is not, however, the usual case. When CFD simulations involve complex cases such as 3D turbochargers, local variables can show important oscillations at different grid refinements. An example of oscillatory convergence is shown in [Figure 4.10](#). Mach and pressure profiles are now evaluated at constant $\theta = 0^\circ$

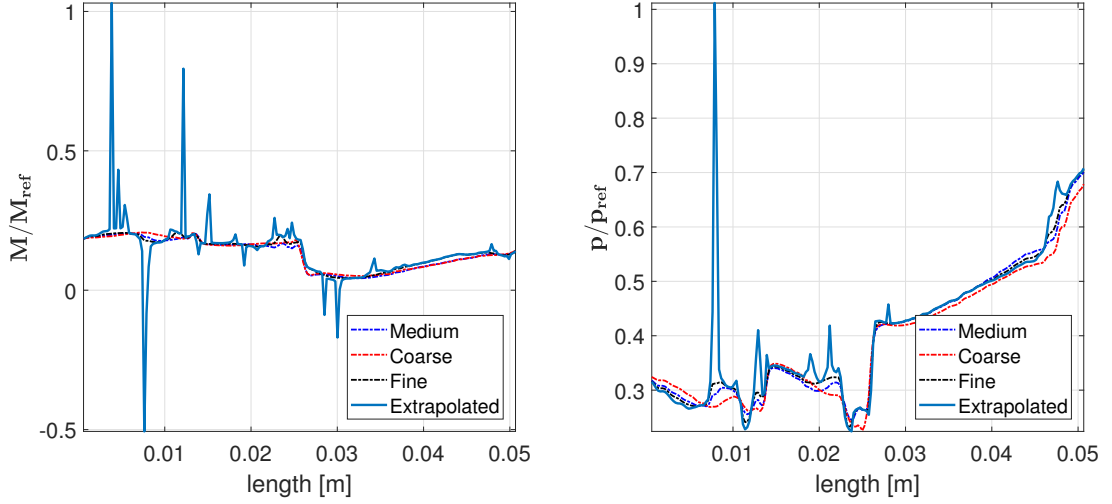


Figure 4.10: Mach and pressure profiles along across the wheel domain on a line at constant $\theta = 0$. RE method fails in the prediction of the extrapolated theoretical solution.

along a line crossing the wheel domain from the inducer to the exducer; this line follows the shroud surface with an offset 0.2 mm, far enough from the wall to avoid velocity to be influenced by the presence of the boundary layer. Jabbed peaks in the extrapolated solution are a clear evidence of a failure on the RE method: one can also notice that between 0 mm and 0.03 mm convergence is not monotonic, but shows a different trend depending on the considered location.

4.3.3 Boundary layer resolution

For the SST Menter $k - \omega$ turbulence model, Ansys CFX allows the application of an Automatic Near-Wall treatment (AWT) based on both wall functions and Low-Reynolds-Number methods (LRN). Note that the addressed Re number is the turbulent Reynolds number: the latter is defined through characteristic variables of the smaller turbulent scales and assumes low values in the viscous sublayer.

LRN methods directly integrate the $k - \omega$ equations over the near-wall mesh. In general, they are more accurate than wall-function treatments since no assumptions concerning the variation of the variables near the wall is required. On the other hand, most low-Re extensions of turbulence models are quite complex and can reduce the numerical performance or even destabilize the numerical method. Moreover, very small mesh length scales in the direction normal to the wall are required to ensure accurate resolution of the boundary layer details. This requirement can be also transferred to a limitation on the wall coordinate y^+ : low values ($y^+ < 2$ for $k - \omega$ models [31]) usually ensure good quality resolution across the boundary layer. Although this requirement can be easily implemented in simple 2D cases, 3D

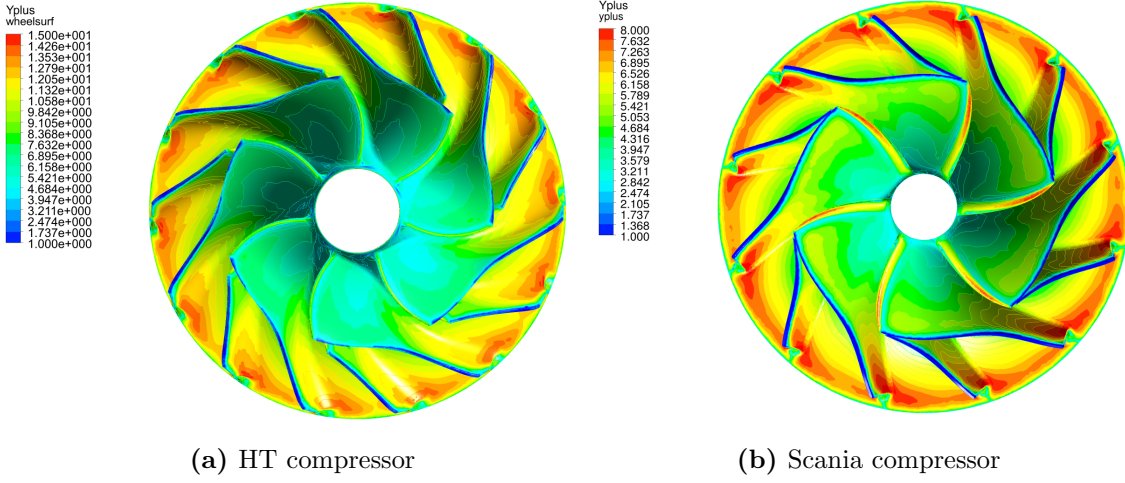


Figure 4.11: y^+ distribution over the impeller surface for both HT and Scania compressors.

complex industrial geometries require high computational resources to solve highly inflated grids: y^+ can thus be one order of magnitude greater than the suggested limit on actual cases.

Automatic Near-Wall Treatment is the most used method to overcome this grid resolution requirement: a gradual switch between wall functions and LRN method is performed across the boundary layer, without a loss in accuracy. Equations are integrated to the wall for low y^+ values ($y^+ \sim 1$), while wall functions are utilized for higher ones ($y^+ \sim 30$); within this range, a blending between the two formulations is adopted. The switch between the two formulations is controlled by Ansys CFX solver and drastically softens the restriction on the grid refinement: meshes with at least 10 cells layers in the boundary layer mesh can now accurately catch the evolution on velocity and temperature profiles.

Figure 4.11 shows the values of y^+ over the impeller surface for both HT and Scania compressors. The boundary layer is directly solved through Low-Reynolds-Number methods over the blade tips ($y^+ < 1$ on both cases), while a blended LRN-wall function formulation is adopted over the remaining surfaces of the impeller ($y^+ < 15$ for the HT compressor, $y^+ < 10$ for the Scania one).

For both Scania and HT compressors, the boundary layer is resolved on a five-layers near-wall mesh. Although not fulfilling suggestions reported in Ansys documentation, Scania experience has proven that 5 layers are enough for correctly modeling boundary layer profiles. Furthermore, a high number of boundary layer cells would drastically increase the computational time of the CFD simulation.

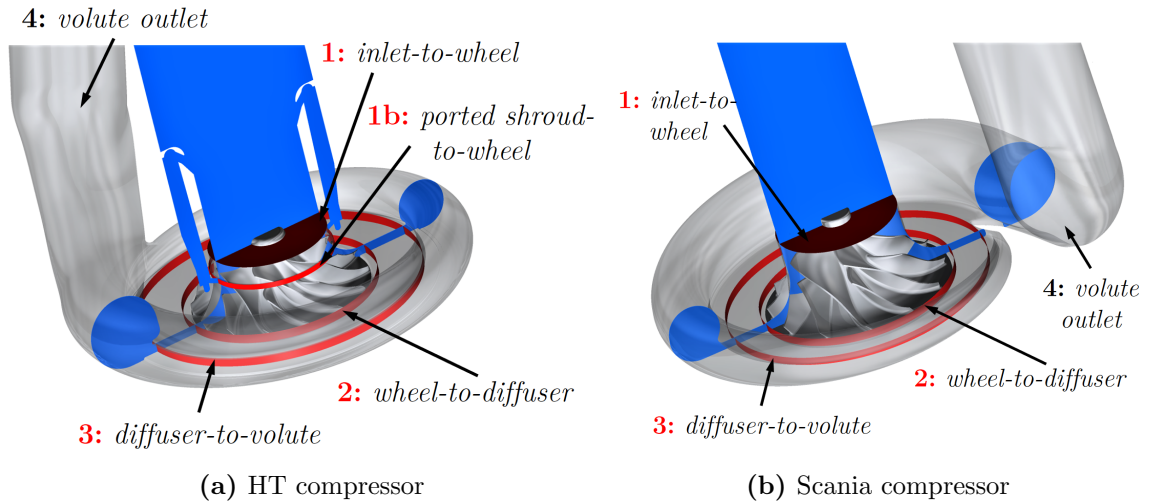


Figure 4.12: Nomenclature of the interfaces for the CFD model. Ported shroud-to-wheel interface is defined only for the HT compressor.

4.4 Interfaces

In agreement with the definitions given in [chapter 2](#), the computational domain is divided in four areas: inlet (it includes the ported shroud cavity in the HT compressor), wheel, diffuser and volute. All domains are stationary with the exception of the wheel one which rotates at the same angular speed of the impeller.

The interfaces between two adjacent domains are illustrated in [Figure 4.12](#). In ordering order, it is possible to identify:

1. inlet-to-wheel interface: connects the stationary inlet domain to the rotating wheel one;
2. wheel-to-diffuser interface: connects the rotating wheel domain to the stationary diffuser one;
3. diffuser-to-volute interface: connects the stationary diffuser domain to the stationary volute one.

For the HT compressor, it is also possible to define the ported shroud-to-wheel interface (1b) between the stationary ported shroud and the rotating wheel domain. [Figure 4.12](#) reports also the presence of a location named "volute outlet" (4): although not representing an interface, this location will be used for further evaluations in the following chapters. Compressor inlet (0) and outlet (5), not visible in the pictures, close the computational domain and are utilized to define boundary conditions.

4.4.1 Interface models

Consider the diffuser-to-volute interface: it connects the stationary domains of diffuser and volute. Ansys CFX solver can easily handle the connection between the two regions with the so-called general-connection interface: all quantities calculated over the interface are directly transferred downstream and the problems due to the eventual mismatch in grid topology between the two domains are directly handled by the solver.

When rotating and stationary domains are interfaced, i.e. when there is a change in reference frame between the two sides of the interface, the situation becomes more complex. For the case under analysis, the critical interfaces are the one which connect the impeller with the stationary inlet and diffuser, i.e. inlet-to-wheel, wheel-to-diffuser and ported shroud-to-wheel.

Three methods are available on Ansys CFX for handling these kind of interface: frozen rotor interface, stage/mixing-plane and transient rotor-stator (Ref. [32]).

Frozen Rotor

Consider transient simulations, i.e. simulations whose evolution is evaluated over a well defined time interval. When the frozen rotor model is implemented, the frame of reference changes across the interface but the relative orientation of the components is fixed: the position of the mesh cells is fixed over the whole computational domain and no mesh-sliding takes place at any interface. The two frames of reference connect in such a way that each of them maintains a fixed relative position during the whole transient simulation. If the frame changes, for example the wheel domain rotates, the appropriate equation transformations are made to take into account the change in relative position of the components.

The frozen rotor model (known also as Multiple Reference Frame MRF² model) therefore produces a steady-state solution at each time instant with some account of the interaction between the two frames (quasi-steady approach).

Although it allows to save a considerable amount of computational time, this model cannot catch the transient effects at the interface. In addition, the losses incurred in the real situation due to flow mixing are not correctly modeled.

When dealing with steady state simulations, all time-marching phenomena are neglected: all quantities evaluated over a rotating or stationary domain are transferred to the component downstream without any operation. All flow structures are thus preserved: considering the wheel-to-diffuser interface, the jet-wake pattern at the impeller outlet is preserved across the interface.

²This alternative nomenclature refers to the interface models available in Ansys Fluent.

Stage/Mixing-Plane

The stage/mixing-plane model (known also as Mixing plane MRF method) is an alternative to the frozen rotor model for modeling a change in the frame of reference. Instead of assuming a fixed relative position of the components, the Stage model performs a circumferential averaging of the fluxes over the interface. Steady-state solutions are then obtained in each reference frame.

Stage averaging neglects transient interaction effects between the components but assumes perfect flow mixing across the interface. The Stage model usually requires more computational effort than the Frozen Rotor model to converge.

Transient Rotor-Stator

Transient rotor-stator interfaces are available only for transient simulations. This model, known also as Sliding Mesh method, the most advanced one available on Ansys CFX, takes into account transient interactions at the interface: in other words, the cells of each component slide along the interface to mimic the rotation of the impeller. On centrifugal compressors, this model predicts the true transient interaction of the flow between impeller and diffuser.

The interface position is updated each timestep, leading thus to higher requirements in terms of computational resources and quantitative postprocessing of the data than the two models introduced before. In the following, all transient simulations will be run with the stage/mixing-plane model in order to reduce the computational time.

Chapter 5

Steady-state simulations on the HT compressor

This chapter is entirely devoted to the analysis of the results obtained by steady-state simulations on the HT compressor. These results are compared with those provided by an experiment carried out in a gas stand: this test allowed to estimate the compressor map in terms of total-to-static performance starting from static pressure measurements given by pressure probes positioned at several important positions of the compressor.

The next discussion will be mainly focused on the first question introduced in [chapter 1](#): is it possible to obtain reliable predictions of the compressor performance by means of RANS steady-state simulations? If not, is it possible to improve the CFD model currently in use to both achieve better agreement with experimental results and avoid the implementation of transient simulations or, even worse, Large Eddy simulations?

In an attempt to answer these questions, several performance indicators (pressure ratio and efficiency, above all) will be analyzed. Afterwards, the fields computed by Ansys CFX will be analyzed to investigate the complex flow field inside the compressor at design point and in proximity of surge.

Finally, different setups are analyzed and compared in the quest for an optimization of the pre-existing model.

5.1 Simulation setup

The setup of the steady-state simulations is initially based on the knowledge and experience developed in the engine CFD group of Scania CV AB during the past years.

Boundary conditions implemented for the simulations are summarized in [Table 5.1](#). Boundary conditions at the inlet, in particular, match the reference ones

(25 °C and 100 kPa): in this way, the corrected quantities introduced in [section 2.2](#) and the real ones are characterized by the same value.

The outlet corrected mass flow is instead varied between two extremes in order to cover all the operational points along the same speed line. The outlet corrected mass flow boundary condition is widely used in turbomachinery: it enables to sweep through the complete machine operational range, including operating points at choke and surge conditions. It is defined as follows:

$$\dot{m}_{corr,out} = \dot{m} \frac{\sqrt{T_{out}^0/T_{ref}}}{p_{out}^0/p_{ref}} \quad (5.1)$$

and allows to estimate speed lines also at choke conditions where a very small change in the actual mass flow can lead to huge variations in both pressure ratio and efficiency.

Table 5.1: Boundary conditions for steady-state simulations.

| | |
|----------------------------|-------------------|
| inlet total temperature | 298,15 K |
| inlet total pressure | 100 kPa |
| outlet corrected mass flow | 0.06 to 0.33 kg/s |

The flow is set as subsonic at the inlet. It must be however reminded that the local Mach number over the impeller blades can exceed unity at high rotational speeds: flow regime is thus transonic over a large part of the compressor map.

Wall are assumed to be adiabatic and the no-slip condition, i.e. $\vec{u}|_{wall} = \vec{0}$, is valid on all walls throughout the domain. The change in frame of reference at the interfaces between stationary and rotating domains is modeled with the stage/mixing-plane model for this initial investigation.

The turbulence model used for the closure of the RANS equations is the Menter SST $k - \omega$. A high resolution scheme is used to calculate the advection terms in the discrete finite volume equations, while the advection scheme adopted for the equations of the turbulence model is a first-order type one.

The maximum number of iterations used for each design point is 250, and the 10^{-4} target for the convergence of the residuals is always met for all speedlines at the near-design point. Anyway, when the convergence criteria are not met, residuals do not exceed 5×10^{-3} : this usually happens when moving away from design conditions and approaching surge or choke where the unsteady flow character does not permit convergence to a steady state.

A total of 30 simulations is used to retrieve the compressor map. Three rotational speeds of the impeller were considered: 51100, 90400 and 110000 rev/min. For each of these angular velocities, a sequence of 10 simulations whose $\dot{m}_{corr,out}$ boundary condition is incremented gradually from 0.06 kg/s to 0.33 kg/s by steps of 0.03 kg/s

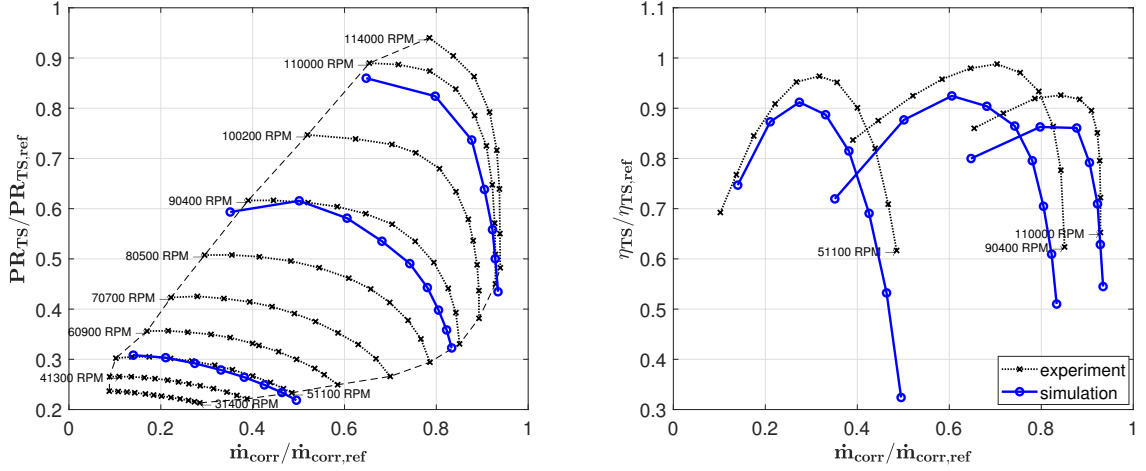


Figure 5.1: Compressor map and total-to-static efficiency for three different speedlines. Experimental results are also plotted in dashed lines.

has been utilized to define each speed line. Initialization was performed by means of a steady-state simulation at conditions close to those of design: for this simulation $\dot{m}_{corr,out} = 0.24$ kg/s and $\omega = 90400$ rev/min are chosen. The setup of the various boundary conditions and the definition of all 30 simulations has been facilitated by the use of the "Parameters set" window of Ansys Workbench.

5.2 Results

The results of the various simulations are reported and discussed in the following paragraphs. Due to data sensitivity reasons, all results are normalized. Regarding the flow field contour plots, all legends have been removed. In any case, all variables range from the lowest value (blue) to the highest one (red): the same scale, i.e. the same minimum and maximum values, is adopted when different cases are compared (for example, [Figure 5.9](#)).

5.2.1 Nominal case

For the nominal case, the actual CAD geometry of the HT compressor is adopted; the interfaces between rotating and stationary components are modeled with the stage/mixing-plane, according to the results of Davy [33]. The three speed lines calculated via CFD simulations are reported in [Figure 5.1](#); a comparison with the compressor map (left) and the total-to-static efficiencies (right) obtained experimentally is also provided.

The first thing that catches the eye is that the pressure ratio is predicted with

good accuracy at 51100 rev/min. At increasing rotational speeds, however, this performance parameter becomes gradually underestimated in the CFD calculation: close to design conditions, which occur approximately at $m_{corr} = 0.42$ kg/s, a 8% decrease compared to the experimental case.

The situation worsens when looking at the total-to-static efficiency: this performance parameter is in fact considerably underestimated at all the operational points. In particular, efficiency at design conditions is underestimated by a 12% error. Moreover, the point of maximum efficiency along the speed line at 90400 rev/min, i.e. the theoretical design point of the compressor, has moved towards lower mass flow rates.

The CFD model analyzed here therefore appears to be wrong. To attempt identifying the cause of this error, an investigation of the trend followed by other significant parameters is fundamental. The first step consists in trying to understand which of the three main components of the compressor, i.e. impeller, diffuser and volute, mostly affects the prediction of the compressor stage performance. Good indications are provided by the total-to-static efficiencies calculated at the outlet interfaces of each of the three components, i.e. $\eta_{wh,ts}$ for the impeller, $\eta_{wh/diff,ts}$ for impeller and diffuser, $\eta_{wh/diff/vol,ts}$ for impeller, diffuser and volute. These efficiencies can be defined as follows:

$$\eta_{wh,ts} = \frac{h_{2,is} - h_1^0}{h_2^0 - h_1^0} = \frac{(p_2/p_1^0)^{\frac{\gamma-1}{\gamma}} - 1}{T_2^0/T_1^0 - 1} \quad (5.2)$$

$$\eta_{wh/diff,ts} = \frac{h_{3,is} - h_1^0}{h_3^0 - h_1^0} = \frac{(p_3/p_1^0)^{\frac{\gamma-1}{\gamma}} - 1}{T_3^0/T_1^0 - 1} \quad (5.3)$$

$$\eta_{wh/diff/vol,ts} = \frac{h_{4,is} - h_1^0}{h_4^0 - h_1^0} = \frac{(p_4/p_1^0)^{\frac{\gamma-1}{\gamma}} - 1}{T_4^0/T_1^0 - 1} \quad (5.4)$$

where the indices correspond to the locations defined in [Figure 2.1](#).

The results, compared with the corresponding experimental ones, are illustrated in [Figure 5.2](#). The graph on the left clearly shows that the efficiency of the wheel is overestimated as the surge regime is approached: this statement holds mainly for the speedline at 51100 rev/min, while the effect is attenuated at higher angular velocities and disappears almost entirely at 110000 rev/min. At intermediate and high mass flow rates, however, efficiency predictions are quite correct, although slightly underestimated.

Different considerations should be made for the diffuser: it is here, in fact, that the compressor experiences the shift of the design point over the speedline at 90400 rev/min and the drastic reduction in efficiency in comparison with the experimental data. This reduction reaches its peak ($\Delta\eta/\eta > 10\%$) under design conditions and intermediate mass flow rates.

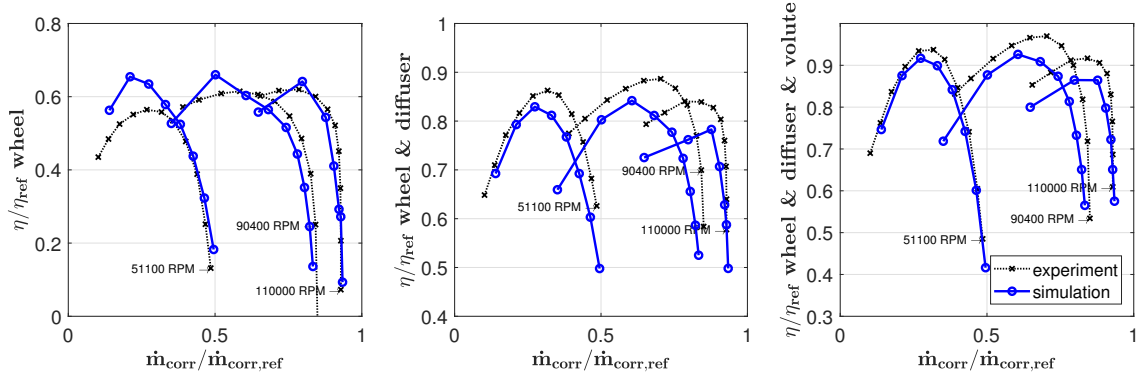


Figure 5.2: Total-to-static efficiency calculated at different interfaces with regards to the outlet static pressure evaluation.

Regarding the volute, the efficiency follows, as expected, the same trend of the stage one already shown in Figure 5.1. Nevertheless, compared to the stage efficiency ones, the curves appear shifted upwards and a better agreement with the experimental data can be observed. This difference is due to the fact that the outlet pipe, in the experimental case, is not perfectly cylindrical as is the case in the CFD simulations, but shows a slight divergence of the walls in the outwards direction: the measured static pressure at the outlet, therefore, is slightly greater than the estimation provided by the numerical simulation where the section of the pipe is cylindrical. It is thus necessary to take this difference into account during the analysis of the stage efficiency. Using total-to-total parameters would be a solution since the flow at the outlet pipe can be modeled as isentropic and total pressure is conserved. Measures of the total variables, however, are not provided by the experiment.

The main component to blame for the poor prediction of performance in the CFD simulation is the diffuser. This statement seems to be confirmed by the graphs of Figure 5.4. These graphs illustrate the pressure growth along the compressor on the basis of measurements obtained experimentally by means of static pressure probes placed on strategic positions of the compressor which were replicated (as far as possible) in the CFD simulation. The positions of the various probes are shown in Figure 5.3: in particular, three probes are positioned at the inlet section of the compressor, two at the diffuser entrance, three at the diffuser outlet and another three at the outlet section of the volute. The measurements provided by the probes are reported with black crosses in Figure 5.4: the corresponding value calculated through CFD simulation is reported instead with blue squares. The pressure profile is obtained in the following ways:

- experiment: an average value of the pressure measurements at each of the four locations is calculated. The pressure profile is simply the connection of these four values;

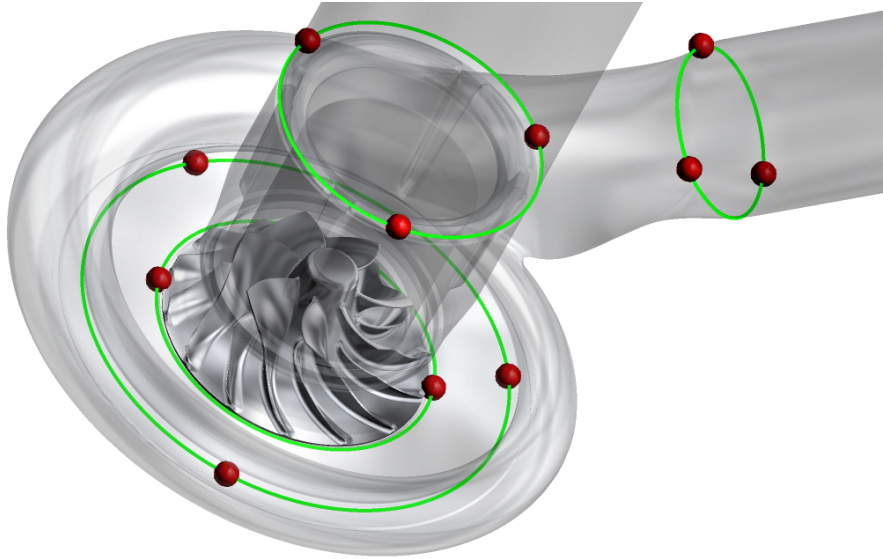


Figure 5.3: Position of the pressure probes on the HT compressor.

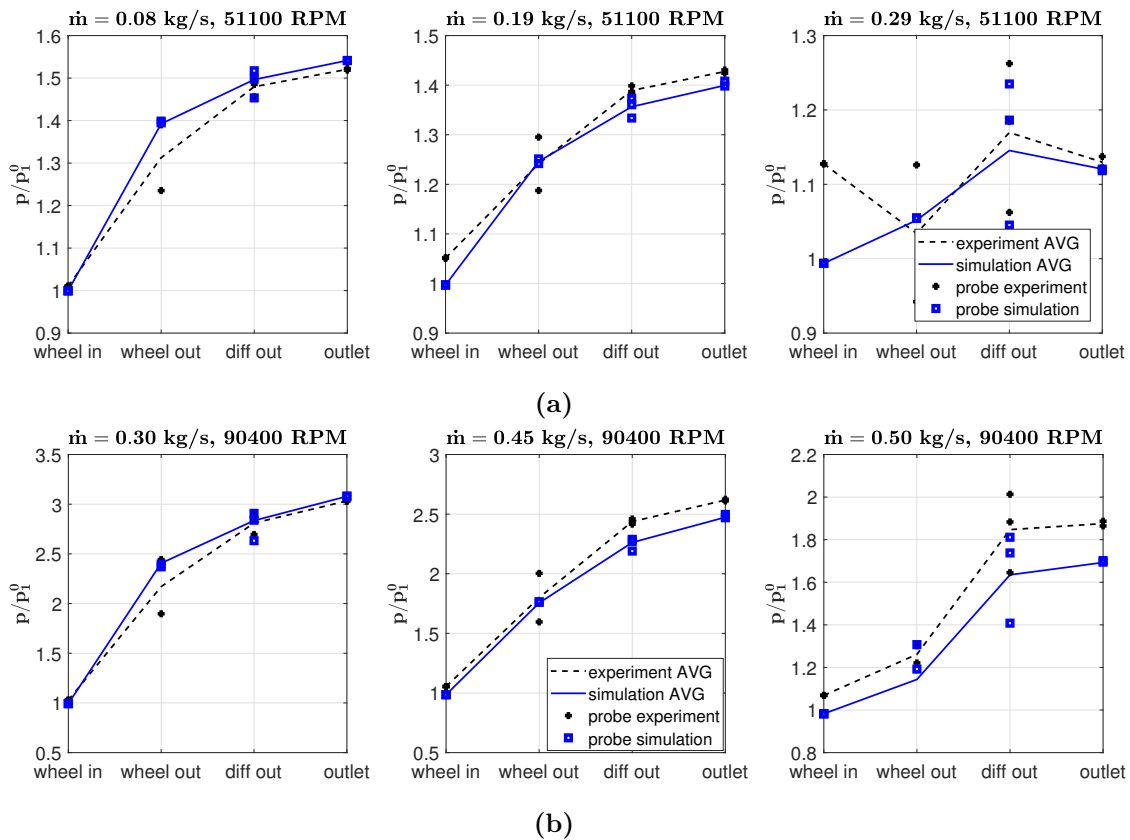


Figure 5.4: Pressure rise over the compressor at different operational conditions. Pressure evaluations are normalized with the inlet total pressure p_0^0 to smear flow unevenness on the experiment.

- simulation: the average value at each location is the result of an average along the circumferences where the probes are positioned (see [Figure 5.3](#)).

Also in this case there is a slight overestimation of the pressure increase over the impeller. The pressure rise over the diffuser, however, is largely underestimated by the numerical solution. Although quite clear, these findings must be taken with caution: the scatter in the experimental points is high, in particular at the impeller outlet due to the high complexity of the flow in that area. The scatter becomes very pronounced as one approaches choke conditions: the results provided by the graph at the top right (0,29 kg/s and 51100 rev/min), for example, are not reliable.

Fields

The analysis of the results continues with the observation of the various fields computed by the CFD simulations. [Figure 5.5](#) shows the velocity fields in terms of relative Mach number along the impeller. By looking at the streamlines, it is immediately noticeable that they appear more uniform at design conditions and follow the blade surface without separating. At lower mass flow rates, the fluid hits the blade leading edge with a high angle of attack, increasing the chances of stall over the suction side. The separation is particularly strong on the splitter blades, where the divergence of the streamlines from the surface is quite pronounced. The reason for this trend of the impeller streamlines can be explained in the following way: the blockage induced by the separated flow over the blades disturbs the inlet flow upstream of the inducer which is in turn forced to hit the blade leading edge with a direction that is not the optimal one. The high angle of attack at the blade leading edge, therefore, induces separation.

Higher speeds are reached at design conditions due to the lower pressure gradient between inlet and outlet of the compressor. The high rotational speeds at the blade tip cause the onset of transonic flow with shock waves: they appear at both design and surge conditions in proximity of the leading edge of the main blades. At design conditions, additional shock waves arise on the splitter blades. The positions of these shock waves are not fixed along the blade profile, but change according to the fluctuations in the state variables measured upstream of the flow discontinuity. Such fluctuations can not be adequately predicted by steady-state RANS models. Firstly, these models can capture the large (inviscid) scales of the flow but not the interaction between shock waves and boundary layer since they are mostly recommended for wall-bounded flows. A second effect produced by the use of steady-state RANS is the introduction of numerical dissipation which damps all gradients and contributes to the poor accuracy on the position of the shock front. In addition, the presence of shock waves can cause flow separation: the entity of the separation changes depending on the fluctuations of the state variables and the position of the shock

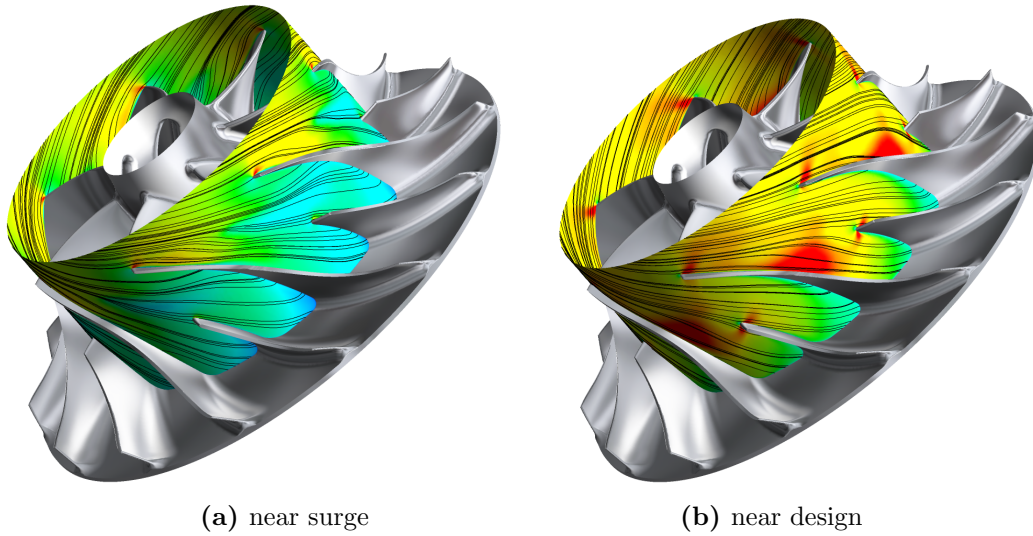


Figure 5.5: Contour of the Mach number on the relative reference frame at near surge (90400 rev/min, 0,3 kg/s) and design conditions (90400 rev/min, 0,45 kg/s). Flow direction is provided through streamlines.

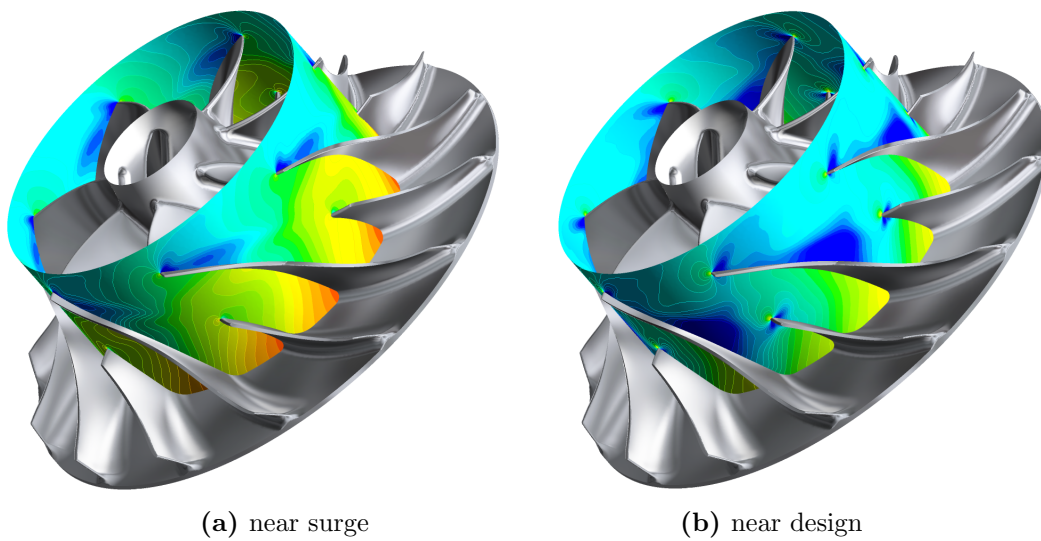


Figure 5.6: Contour of the pressure at near surge (90400 rev/min, 0,3 kg/s) and design conditions (90400 rev/min, 0,45 kg/s).

front. By neglecting any flow time-dependency, steady-state models fail to predict the size of the recirculation bubbles over the blades.

Shock waves can also be visualized on the static pressure fields of [Figure 5.6](#). The discontinuity on the suction side immediately downstream of the main blades leading edge identifies the position of the shock wave. The latter grows in intensity when, at fixed rotational speed, the mass flow is increased. Downstream of the

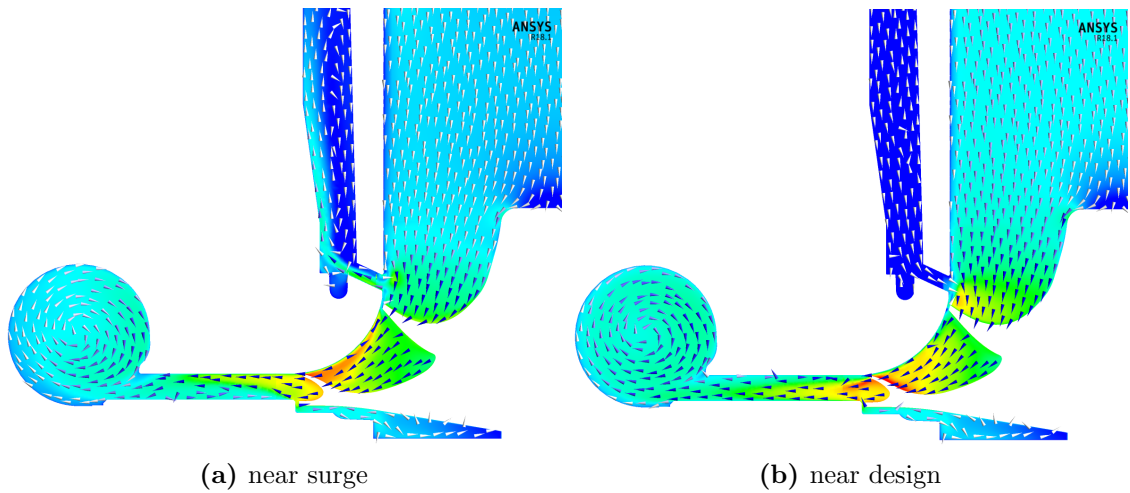


Figure 5.7: Meridional velocity calculated on the stationary reference frame at near surge (90400 rev/min, 0,3 kg/s) and design conditions (90400 rev/min, 0,45 kg/s). The vectors indicate only the flow direction, the magnitude of the velocity, in terms of Mach number, is given by the contours plot.

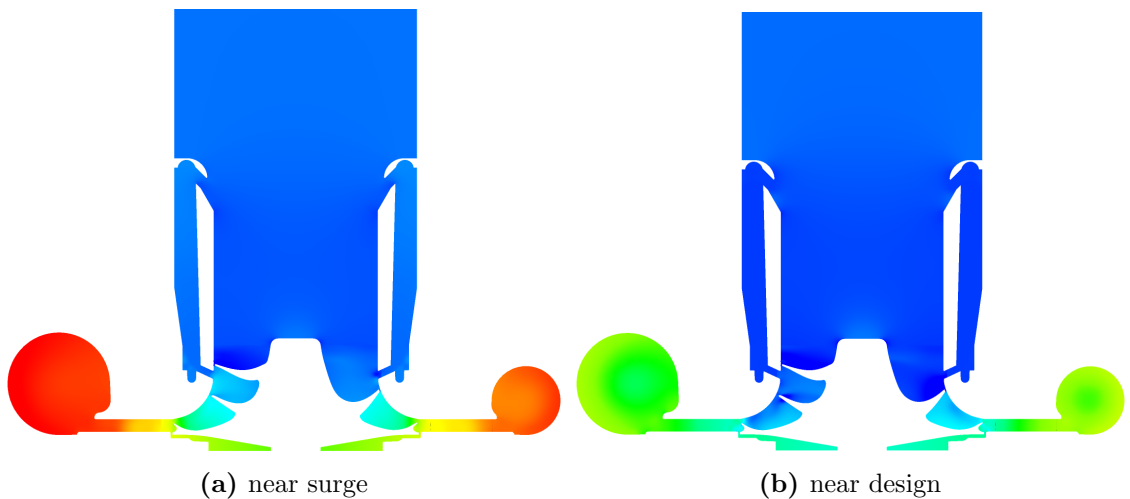


Figure 5.8: Pressure field on the meridional plane at near surge (90400 rev/min, 0,3 kg/s) and design conditions (90400 rev/min, 0,45 kg/s).

shock, the pressure decreases along the suction side. At the same time, the pressure builds up over the impeller due to the flow displacement along the radial direction. The pressure gradient along the end of the impeller increases as one moves from design to surge conditions over a speed line: consequently, pressure recovery along the terminal part of the blade suction side is not sufficient to overcome the strong gradient downstream of the impeller and the flow separates from the blades.

Velocity and static pressure fields over the meridional plane XZ are reported

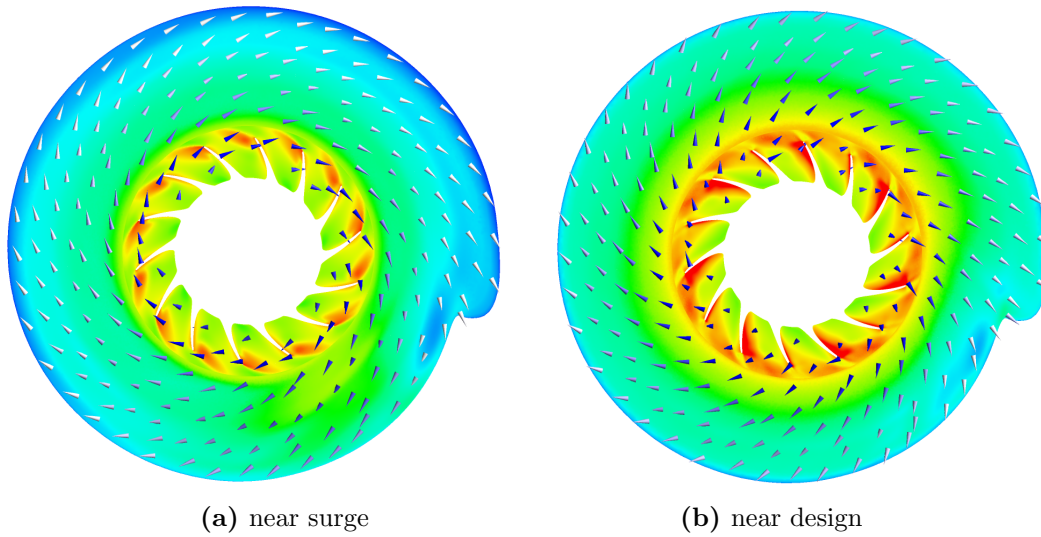


Figure 5.9: Mach number variation on the diffuser at near surge (90400 rev/min, 0,3 kg/s) and design conditions (90400 rev/min, 0,45 kg/s). The vectors are indicative of the flow direction, the magnitude of the velocity, in terms of Mach number, is provided by the contour plot.

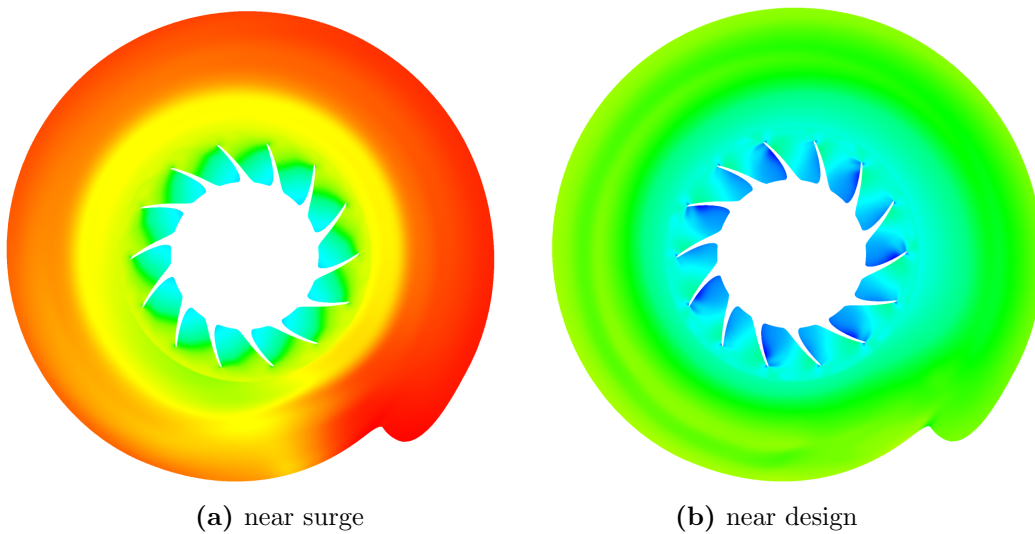


Figure 5.10: Pressure field in the diffuser at near surge (90400 rev/min, 0,3 kg/s) and design conditions (90400 rev/min, 0,45 kg/s).

in [Figure 5.7](#) and [Figure 5.8](#). At design conditions, the fluid recirculating in the ported shroud cavity is not enough to considerably affect compressor performance. A separation bubble appears on the upper surface of the diffuser: the extent of this separation is probably overestimated by the simulations, and that could explain why the pressure growth along the diffuser has been drastically underestimated by the graphs of [Figure 5.2](#).

The recirculation is much more pronounced near surge: the low momentum flow separating from the blades is ventilated into the cavity and pushed towards the inlet pipe by the favorable pressure gradient. With regard to the static pressure, a higher compression over the stage is noticeable at low mass flow rates, in line with the trends reported on the compressor map.

Finally, the same variables are visualized on a horizontal plane placed along the diffuser mid-surface (Figure 5.9 and Figure 5.10). The first thing that catches the eye is the discontinuity over the wheel-to-diffuser interface. The velocity, in fact, is averaged along the interface surface: the unevenness in the flow field at the impeller outlet produced by the jet/wake-like structures is therefore lost.

The angle α (see subsection 2.3.2) of the flow spiral along the diffuser is lower near surge due to the lower radial velocity at the exit of the impeller. The streamlines, therefore, hit the tongue at an angle different from the optimal one, creating a high-pressure stagnation region in its vicinity. This phenomenon is less pronounced at design conditions because the flow enters the volute with a better alignment with respect to the pipe walls.

The velocity does not show axial-symmetry over the diffuser at near surge conditions: the presence of the tongue causes an acceleration of the flow along the 5 o'clock direction. This effect disappears almost completely at design conditions.

5.2.2 Summary

The study on performance and the visualization of both velocity and pressure fields have clearly demonstrated that the model fails to correctly capture the flow inside the compressor as soon as it moves towards high rotational speeds; moreover, the error in performance calculated at design point is quite significant and the main component to blame is the diffuser. The underestimation of diffuser's performance could be attributed to several factors:

- high sensitivity of the model to small variations on the geometry; in particular, the distance between the shroud and the blade tip, the so-called tip-clearance, can significantly influence the performance. If the dimensional tolerances defined in the CAD model are not adequately followed during the production process or, conversely, the geometry scan is not performed correctly, experimental results would differ considerably from the numerical ones. In this case, the flow exiting the impeller would differ from the one actually observed during an experiment leading to erroneous estimation of the diffuser performance;
- the stage/mixing-plane model for the interfaces between rotating and stationary domains does not capture the gradients of the main variables (\vec{u} , p , T , etc.) along the tangential direction on the diffuser. A frozen rotor model could give better results;

- RANS models are not suitable for simulating the flow inside centrifugal compressors at high rotational speeds. It is known, in fact, that velocity fluctuations and other time-dependent phenomena are not adequately captured by these time-averaged models since they are calibrated for statistically steady flows. Major problems arise near surge: velocity fluctuations, in fact, play an important role in these regimes. On the other hand, steady-state cannot be relied on the analysis of the transonic regime: the position of the shock waves fluctuates along the blade profile and transient simulations are required to capture this variation. Advanced models like Large Eddy Simulations (LES) could allow more accurate estimates of the performances: nevertheless, LES models require more computational resources than RANS and are usually utilized mainly in research.

The first two points are analyzed in the following sections. In particular, a study on the tip-clearance will be carried out in order to understand its impact on performance. Then, stage/mixing-plane and frozen rotor models for the interfaces will be compared in order to understand which of the two could provide better results. Regarding compressor performance analysis through LES simulations, please refer to the literature, e.g. [14][17][34][35].

5.2.3 Effect of the axial tip-clearance

The expression "tip-clearance" identifies the gap between the inner surface of the shroud and the blade tip at the exducer: this space is conventionally measured along the axial direction, i.e. the Z axis.

It is well known from literature and experiments that the tip clearance between shroud and blades plays a crucial effect on compressor performance. The most common empirical formulas developed in literature (Ref. [12]) relate the change in stage efficiency to the change in tip clearance scaled with the blade height. Although convenient, this geometric scaling does not take into account the proper fluid mechanics of the flow developing around the impeller: only phenomena happening in proximity of the blade tip are significant for this analysis.

The most used formula in turbomachinery applications is due to Senoo and Ishida [12]; by denoting the tip clearance with t_2 and the height of the blade at the impeller outlet with b_2 , the relative loss in efficiency with respect to the theoretical zero-tip-clearance case can be determined through the following formula:

$$\frac{\Delta\eta}{\eta} = \kappa \frac{t_2}{b_2} \quad (5.5)$$

where κ is a factor whose value ranges between 0.25 and 0.35, as reported by Hill and Peterson [10]. Senoo and Ishida suggest $\kappa = 0.3$, and this value will be used in the following.

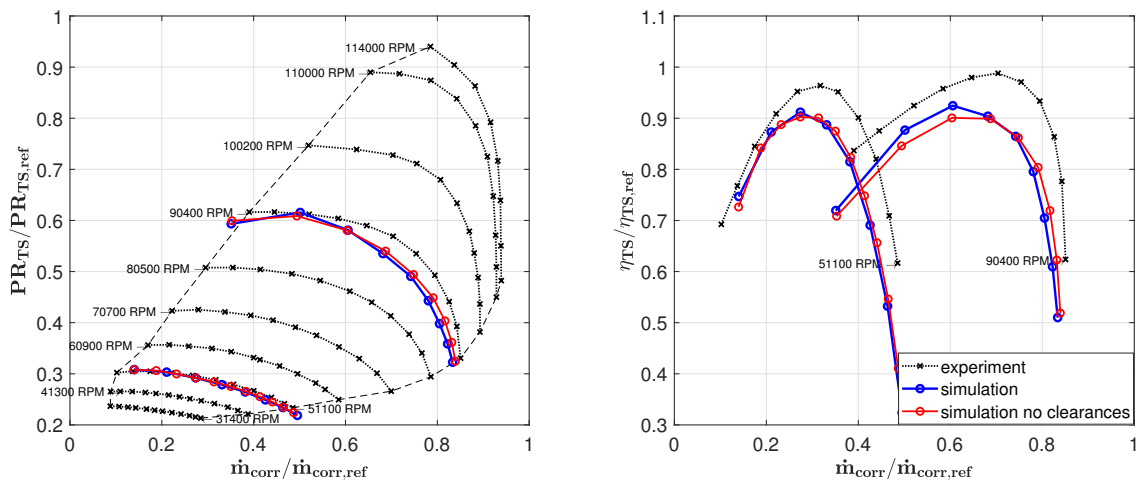


Figure 5.11: Compressor map and total-to-static efficiency for two different speedlines. Results for the case with zero tip clearance are colored in red.

The flow passage through the tip-clearances is highly dissipative: due to the high rotational speed of the impeller and the difference in pressure between the two sides of the blade, the flow tends to flow over the clearances and recirculates over the suction side.

In order to analyze the effect of the tip-clearance, several steady-state simulations with the same setup of [section 5.1](#) were performed on a modified geometry of the HT compressor. For this study, the impeller has been displaced upwards along the axial direction in order to reduce the tip-clearance at the blade trailing edge to $t = 5 \cdot 10^{-5}$, i.e. the minimum size beyond which the local quality of the mesh falls below the suggested values of skewness in [section 4.2](#).

The aim of this study is to investigate the sensitivity of the compressor stage performance to a change in axial tip-clearance at the blade trailing edge. On the actual compressor all clearances are measured on a cold, stationary geometry. During its operation, however, the material with which the impeller is built (aluminum, for this case) expands due to the high temperatures locally reached by the flow, while the high inertial forces can bend the blades: the actual value of the clearance can thus change.

The compressor map and corresponding total-to-static efficiency curves are shown in [Figure 5.11](#); the solution of the nominal case is also reported for completeness. Variations are small for both pressure ratio and efficiency. In particular, a slight increase at high mass flow rates for the two speed lines at 51100 rev/min and 90400 rev/min is observed; on the other hand, a slight decrease is observed at low mass flow rates. Variations at design conditions are instead negligible. Nevertheless, the point at maximum efficiency computed by the simulation, i.e. the desired design

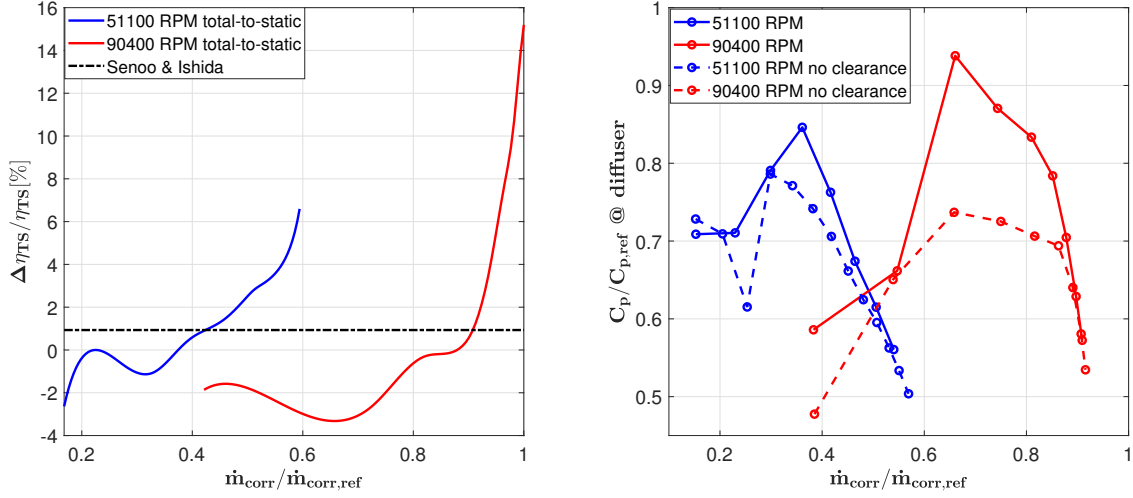


Figure 5.12: Left: percentage variation of the total-to-static efficiency of the stage between the two simulations. Reference value from Senoo and Ishida [12] is plotted in dashed lines. Right: $C_{p,diff}$ evaluated for two different speedlines. The case with zero tip-clearance is plotted in dashed lines.

point, is placed at the same mass flow conditions of the experimental one.

The percentage difference in efficiency between the two simulations is shown in the left graph of Figure 5.12 for both speed lines. The theoretical value of $\Delta\eta/\eta$ obtained through Equation 5.5 is also reported as a dashed line. The theoretical value matches the numerical solution only for the design point at 51100 rev/min, while it diverges significantly in all other operational conditions. The divergence from the theoretical value grows exponentially as soon as the choke regime is approached: the slope of the curves $\eta(\dot{m}_{corr})$ at high mass flow rates is in fact almost vertical and the differences are consequently amplified.

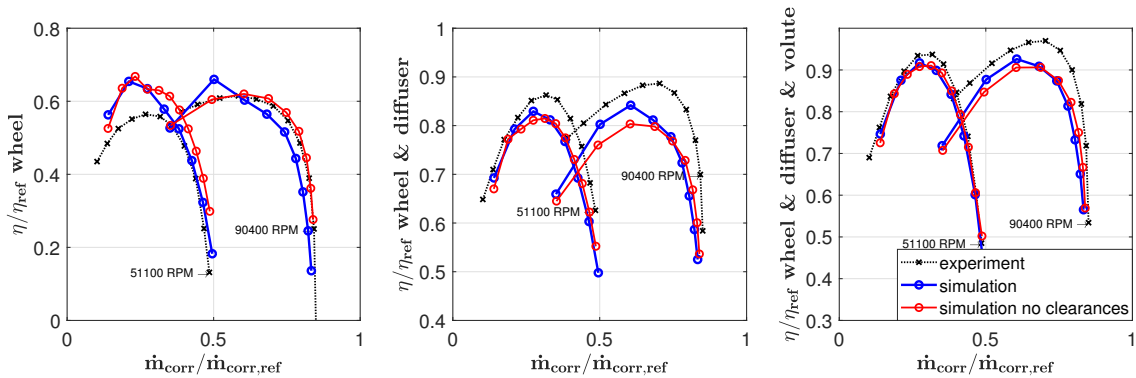


Figure 5.13: Total-to-static efficiency calculated at different interfaces with regard to the outlet static pressure evaluation. Results for the case with zero tip clearance are colored in red.

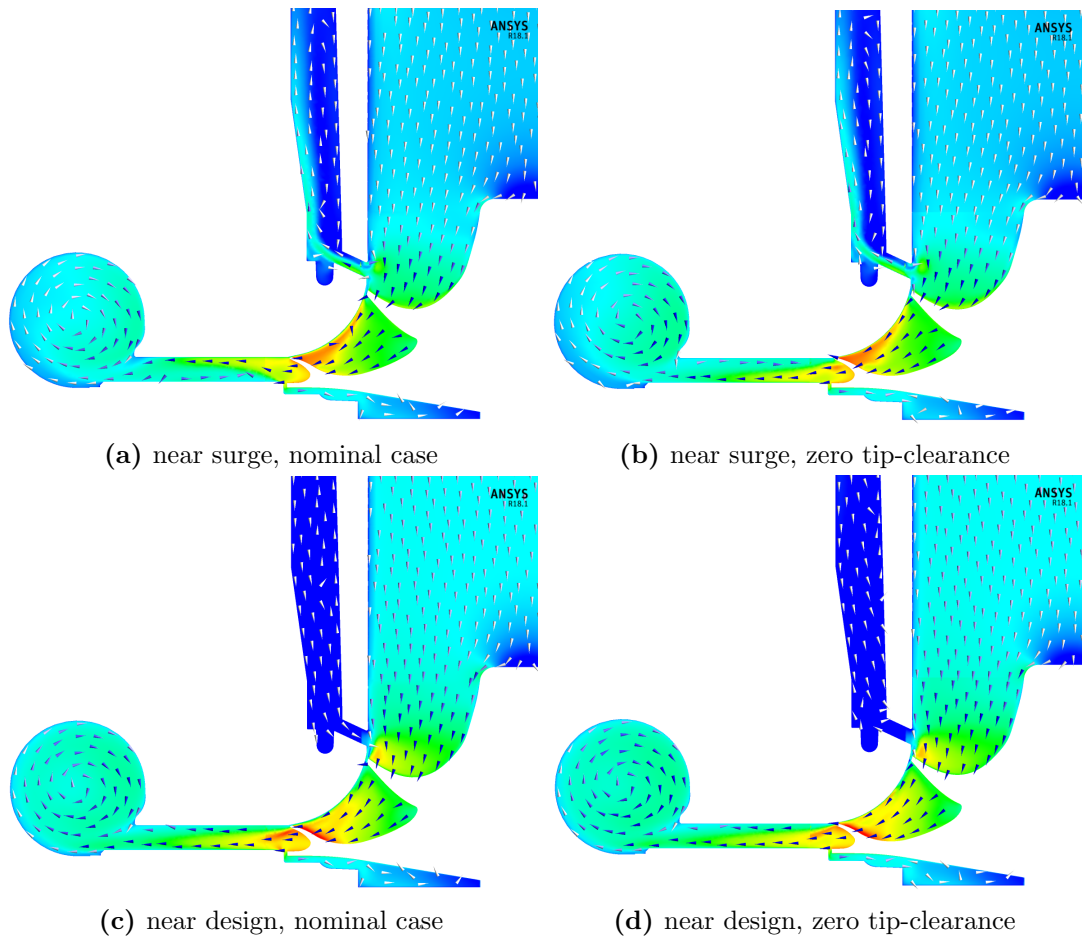


Figure 5.14: Meridional velocity calculated on the stationary reference frame at near surge (90400 rev/min, 0,3 kg/s) and design conditions (90400 rev/min, 0,45 kg/s). The vectors indicate only the flow direction, the magnitude of the velocity, in terms of Mach number, is given by the contour plot.

The lack of agreement between theoretical and numerical value of $\Delta\eta/\eta$ at 90400 rev/min may be due to the onset of shock waves over the blades surface. As discussed later in the chapter, some caution is needed when solving transonic flows with RANS models.

Efficiencies calculated at the outlet interface of the various components have been reported also for this case. Results are shown in [Figure 5.13](#). The general trend is similar to what observed in [subsection 5.2.1](#): only a slight increase at high mass flow rates and a slight reduction at low ones are highlighted by the graphs, in line with the conclusions drawn for the compressor stage efficiency. It is interesting to note that the impeller efficiency at 90400 rev/min matches the experimental ones with a high degree of accuracy: it should however be reminded that this agreement is the outcome of a simplified computational model which overestimates the losses

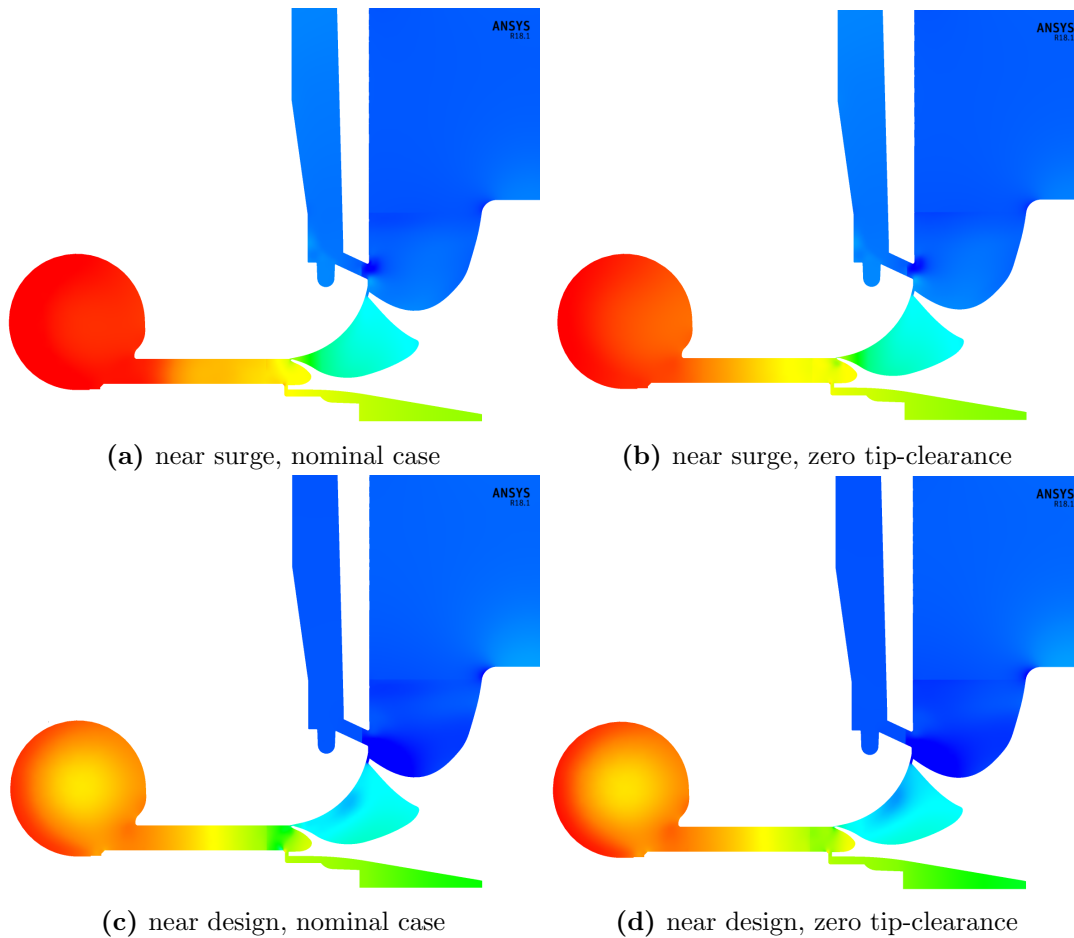


Figure 5.15: Pressure on the meridional plane at near surge (90400 rev/min, 0,3 kg/s) and design conditions (90400 rev/min, 0,45 kg/s).

and underestimates performance at almost all operational conditions.

In the right graph of Figure 5.12 the values of the pressure coefficient $C_{p,diff}$ of the diffuser for both speed lines are also reported. It can be noted that in both cases the maximum value is not reached at the design point, but at slightly lower mass flow rates. After this maximum, $C_{p,diff}$ decreases rapidly with the mass flow rate. Apart from regimes near the surge characterized by high instability in the flow, and therefore difficult to model through steady-state simulations, the zero-tip clearance case is globally characterized by lower values of $C_{p,diff}$. Moreover, at all operational points, $C_{p,diff}$ never reaches the suggested value, for a vaneless diffuser, of 0.5 : this confirms what has been widely discussed about the bad performance of the diffuser.

Fields

Velocity and static pressure fields of the new configuration are now compared with the nominal case. [Figure 5.14](#) shows the velocity field in terms of Mach number in the stationary frame at design and near surge condition for the case $\omega = 90400$ rev/min.

The differences due to the tip-clearance reduction are minimal. At design, a slight increase in flow recirculation and a decrease in local velocity near the exducer can be observed. A slightly more conspicuous effect appears instead when approaching the surge limit: flow separation does no longer occur on the upper surface of the diffuser, but rather on the lower one. This change can theoretically explain the reason for the differences in efficiency measured for the two cases.

Few changes are observable even in pressure fields ([Figure 5.15](#)): the only qualitatively remarkable effect is the increase in static pressure at the exducer due to the lower local flow velocity.

5.2.4 Position of the wheel-to-diffuser interface

The third parameter taken into account in an attempt to improve the accuracy of the CFD model for the HT compressor is the type of interface between rotating and stationary components.

In the previous cases, only the stage/mixing-plane model has been implemented for inlet-to-wheel, ported shroud-to-wheel and wheel-to-diffuser interfaces; the study of performance and flow evolution with a frozen rotor model becomes interesting in order to highlight any potential weakness or strength. In the following, the attention is mostly focused on the wheel-to-diffuser interface since it is the most critical one. When considering steady-state simulations, both methods show weaknesses and strengths. Although it allows to capture the wakes drawn by the flow coming out from the impeller, the frozen rotor interface does not take into account the mixing produced by the high rotational speed of the impeller: a non-homogeneous flow therefore characterizes the diffuser and a clear distinction between high and low speed zones is visible, in contrast to the real case where all gradients along the circumferential direction are damped. On the other hand, the stage/mixing-plane interface replaces the local values of flow properties with an average calculated along the circumference, canceling velocity gradients created by the jet-wake type of flow exiting the impeller. The resulting representation of the flow pattern adheres more to the experimental observation, but the simplification implemented for the transition of the flow through the interface is rather drastic.

In any case, the angle at which the flow reaches the volute can change according to the position and type of interface used, implying also a possible variation in the overall performance of the compressor.

A parametric study of the position of the wheel-to-diffuser interface was carried out in order to highlight the trends of pressure ratio and efficiency. This study is

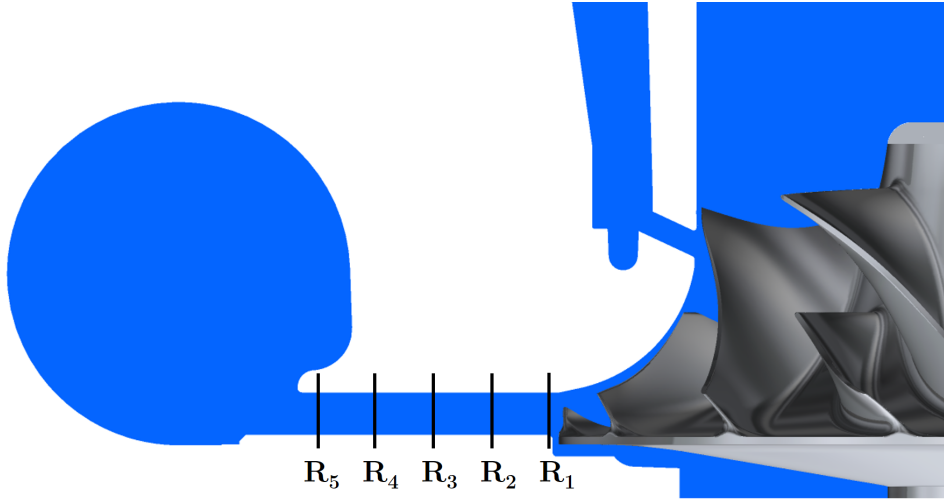


Figure 5.16: Positions of the wheel-to-diffuser interface along the diffuser.

replicated for both interface models: the same model is applied on each of the three interfaces defined on the HT compressor. The position of the above interface has been gradually moved along the diffuser starting from an area close to the exducer up to the entrance of the volute. The five setups considered are shown in [Figure 5.16](#); the corresponding numerical values, instead, are indicated in [Table 5.2](#).

All the simulations were launched by setting the boundary conditions in such a way to simulate design conditions, i.e. 90400 rev/min and $\dot{m}_{corr} = 0.42$ kg/s.

Table 5.2: Radius of the wheel-to-diffuser interface along the diffuser.

| | R_1 | R_2 | R_3 | R_4 | R_5 |
|-----------------------|-------|-------|-------|-------|-------|
| interface radius [mm] | 52 | 59 | 66 | 73 | 77 |

At the same time, the same setup was used to launch simulations on a modified HT compressor design without back-plate. The space between the lower surface of the diffuser and the impeller is closed by a stationary wall in this new configuration. Due to the strong velocity gradients arising on the very small gap between the stationary back-plate and the rotating impeller, large losses due to shear stress can be observed in this area. The highest temperatures of the flow can be measured at the back-plate as a consequence of the high shear stress that develops in the region. An accurate CFD model for the flow underneath the wheel could therefore improve the predictions of the overall performance of the compressor.

Results for the parametric study of the position of the wheel-to-diffuser interface are shown in [Figure 5.17](#). The dashed-lines refer to the design without back-plate; the corresponding experimental values of the performance parameters, i.e. pressure and efficiency, are plotted in black.

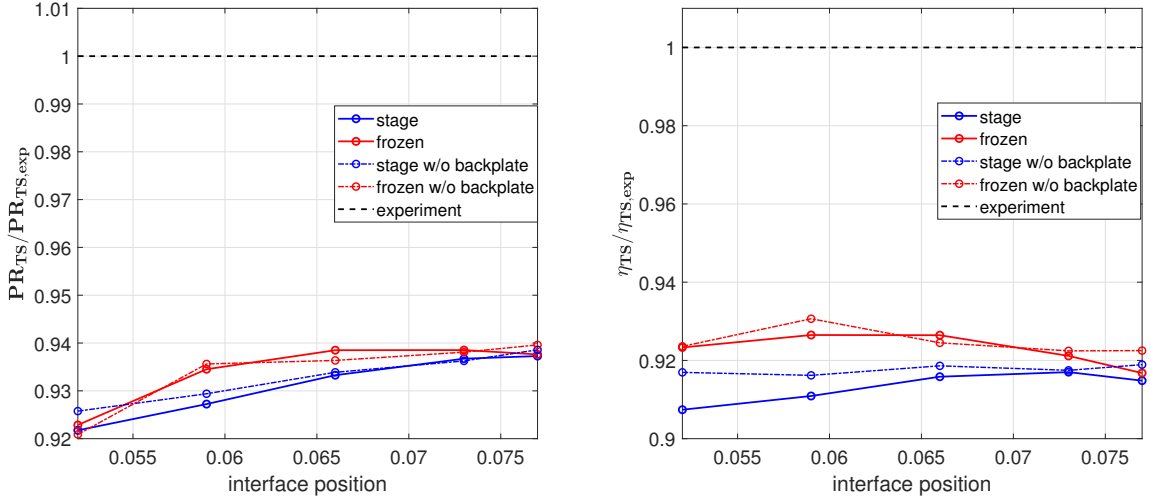


Figure 5.17: Variation of pressure ratio and efficiency values for different positions of the wheel-to-diffuser interface

The removal of the back-plate does not involve major changes in the performance parameters for both stage/mixing-plane and frozen rotor interface. It should be remembered that the amount of fluid trapped in the cavity between the back plate and the impeller is very low and the effects due to high stress shear, which can be translated into a considerable increase in temperature, occur only locally, without significantly affecting compressor performance.

Similarly, the improvement in performance prediction given by the frozen rotor interface is minimal ($< 2\%$ for both pressure ratio and total-to-static efficiency) in comparison with the stage/mixing-plane one. Neither model shows appreciable improvements in performance as the interface position changes. However, it is possible to identify for both models an optimal case at R_3 , i.e. in the case of an interface positioned at a radius of 66 mm. To analyze whether this slight improvement also affects other operational points or not, steady-state simulations were run for two speedlines at 51100 rev/min and 90400 rev/min.

The results are shown in [Figure 5.18](#) and are compared with the nominal case of [subsection 5.2.1](#); for the purposes of this analysis, the data of the latter case correspond to those obtained with a stage/mixing-plane interface placed at R_1 . At high rotational speeds, the pressure ratio values are very close to the experimental ones. However, the difference to the experimental data remains remarkable if one looks at the efficiency: a slight increase compared to the case with stage mixing-plane interfaces can be observed along both speedlines, but the overall effect is very limited. The position of the design point along the horizontal axis, however, is accurately predicted by the simulations using a frozen rotor interface.

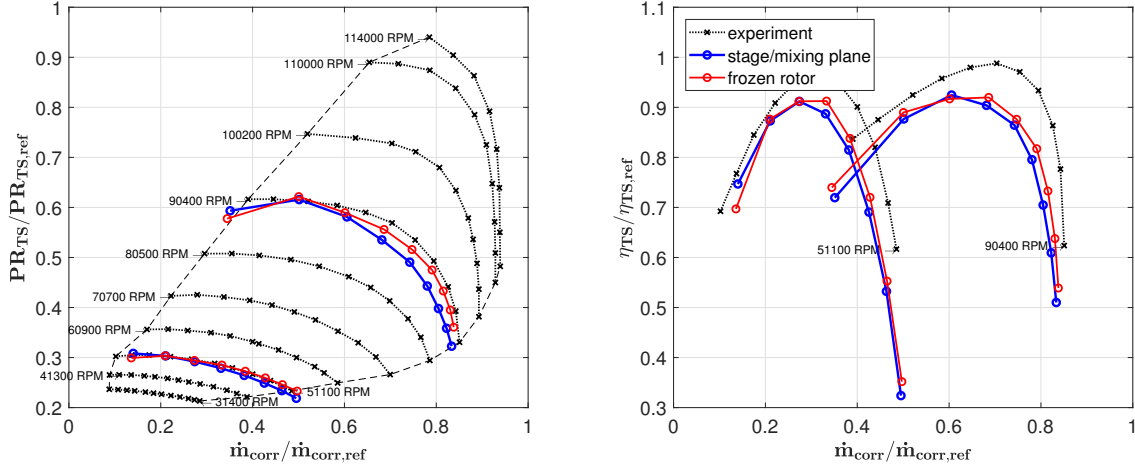


Figure 5.18: Compressor map and total-to-static efficiency for two different speedlines. Results for the case with frozen rotor interfaces are colored in red.

Fields

The comparison between stage/mixing-plane model with the interface positioned at R_1 and frozen rotor model with the interface placed at R_3 continues with the analysis of the velocity field inside the compressor. This analysis aims to highlight the differences brought by the shift of the interface position and the implementation of a frozen rotor model.

The velocity field along the diffuser mid-plane is illustrated in [Figure 5.19](#): on the row above the fields at conditions close to surge are shown for both models of the interfaces; on the row below, instead, those at design conditions are reported. Wakes are visible only in the case of the frozen rotor: the shift of the interface position in direction of the volute enables the visualization of the flow structures generated at the impeller outlet. In addition, wakes and velocity changes along the diffuser circumference are preserved even once the frozen rotor interface is passed. On the other hand, a stage/mixing-plane interface placed at the exducer erases all the structures as the flow passes through it.

This effect is highlighted in [Figure 5.20](#): all velocity gradients along the circumference of the interface imposed by the jet-wake pattern of the flow exiting the impeller are replaced with an average. In the two graphs on the right, instead, it is possible to observe the alternating high and low speed structures which characterizes the jet-wake model. Structures are less pronounced at design conditions because of the higher speeds reached by the flow.

Coming back to [Figure 5.19](#), the size of the stagnation zone in proximity of the tongue is smaller for the case of frozen rotor interfaces: this effect is magnified near surge conditions, while it is less pronounced at design conditions. Moreover, at surge

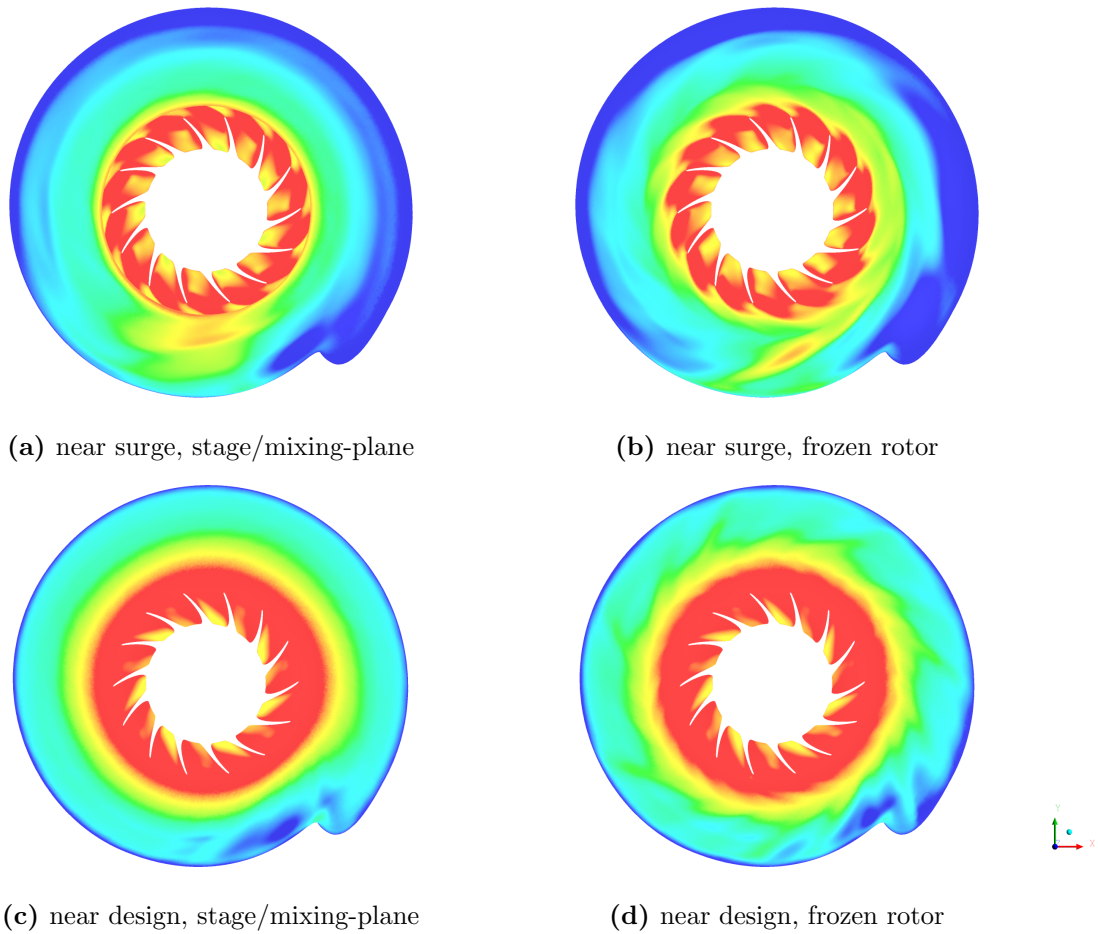


Figure 5.19: Mach number inside the diffuser at near surge (90400 rev/min, 0,3 kg/s) and design conditions (90400 rev/min, 0,45 kg/s).

conditions the high-speed zone observable at 6 o'clock appears to be wider when a stage/mixing-plane interface is utilized. The extent of this region is limited to a single fluid wake in the case of frozen rotor interface.

5.3 Concluding remarks

Steady-state RANS simulations analyzed in this chapter highlighted the difficulties encountered in predicting the performance of the HT compressor. In particular, speedlines calculated by means of CFD simulations diverge considerably from the experimental ones for higher the rotational speed of the impeller. On the other hand, total-to-static efficiency is drastically underestimated at every operational condition of the compressor: in particular, the efficiency of the diffuser is wrongly predicted. Although the prediction of the pressure ratio improves with the use of

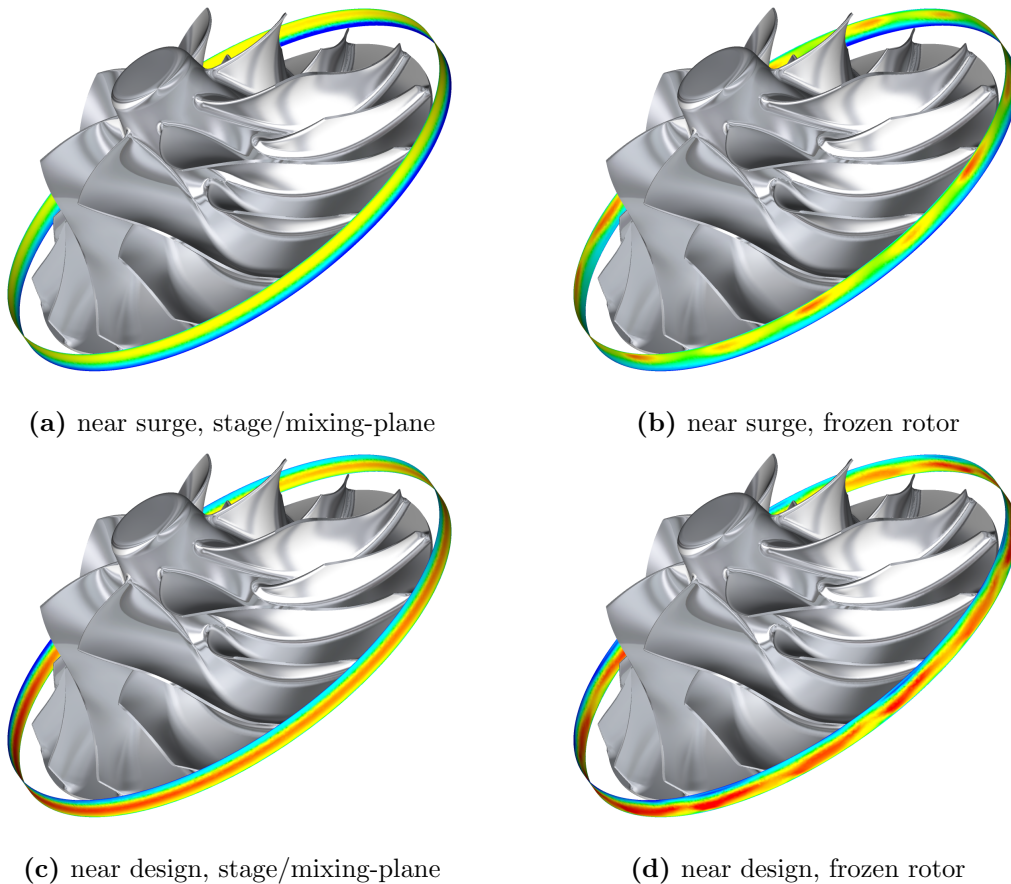


Figure 5.20: Velocity field in proximity of the exducer at near surge (90400 rev/min, 0,3 kg/s) and design conditions (90400 rev/min, 0,45 kg/s).

frozen rotor interfaces, the mismatch between simulation and experiment remains consistent with regards to the compressor stage efficiency. The divergence observed in the compressor map may be due to the inability of the model to capture the interaction between shock waves and boundary layer: at high rotational speeds, in fact, the flow becomes transonic and several shock waves appear over the surface of the blades.

Anyway, the study of the effect of the axial tip-clearance has shown that small variations in the geometry of the impeller can lead to (small) changes in performance. The slight divergence of the compressor outlet pipe in the experimental apparatus increases the divergence in total-to-static efficiency curves between experiment and CFD simulation. This effect could be mitigated by the use of total-to-total parameters for the analysis of experimental data, but it would require the placement of directional Pitot tubes over the compressor that must be parallel to the incoming flow. Due to the small size of the HT compressor and the high swirling flow, this kind of analysis would be prohibitive.

The frozen rotor interface allows a slight improvement in the prediction of the performance, in particular with regard to the pressure ratio. The parameteric study of the wheel-to-diffuser interface allowed identification of the an optimal position which optimizes the performance prediction, but the improvements on the efficiency curves are minimal.

The main limitation of this analysis is that the results obtained can not be universally extended to other centrifugal compressor geometries for automotive turbochargers. Whenever one attempts to evaluate the accuracy of the CFD simulations by means of comparison with experimental data, it is always necessary to investigate the causes of possible mismatches in the results.

Finally, the study of the position of the wheel-to-diffuser interface and the differences between stage / mixing-plane and frozen rotor model for the interfaces is suggested every time the analysis of the performance of a new compressor is started.

Chapter 6

Design optimization

6.1 Design of Experiments (DoE)

The Design of Experiments (DoE) approach is very useful in order to optimize the setup of an experiment or the performance of a component. DoE is a widely used tool in engineering which provides a structured way to change multiple settings in order to understand their impact on the final result. Moreover, by manipulating multiple inputs at the same time, DoE can also identify important interactions between all the parameters under analysis.

When planning and performing an experiment, the first thing to do is to try to figure out what are the most important factors that can affect the evolution of the process. The input conditions ("input variables" or "predictor variables" in statistics) are then manipulated in order to see whether the output parameters ("output variables" or "response variables") under analysis have changed or not, and whether there is a clear dependency that relates the input to the output.

The process just described is quite straightforward when the input consists of only one parameter, but turns out to be very difficult when multiple factors affect the process.

One can also define "control variables" which must be held constant to prevent external factors from affecting the results and "random variables" which are not controlled and are free to change randomly. DoE involves not only the selection of input, output, control and random variables, but also planning the experiment in the best possible way in terms of resource consumption.

The simplest approach that can be used when multiple input variables are available is the so-called one factor at a time (OFAT) method [36]. It consists in varying only one input variable at a time while keeping others fixed. In particular, once the optimal value for one parameter has been found, the latter is kept constant and the following one is varied. The procedure is iterated until all parameters are sequentially optimized. Although very simple, this method has serious drawbacks.

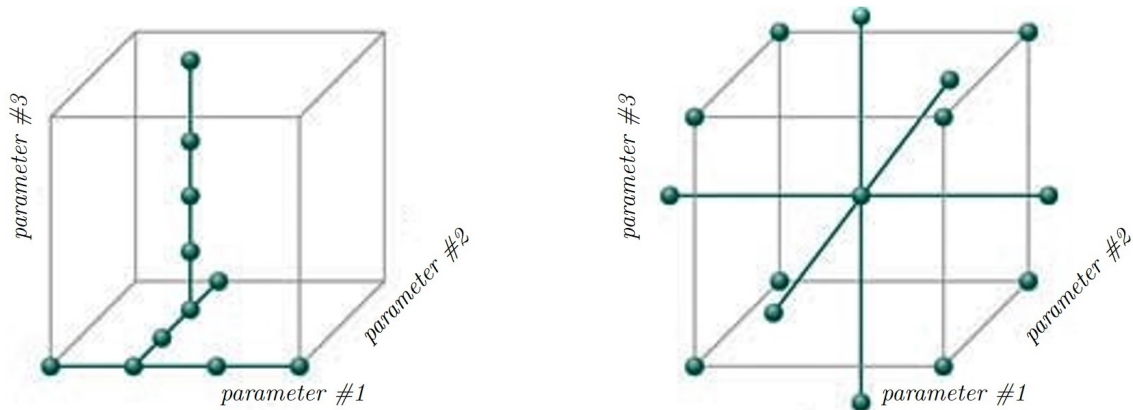


Figure 6.1: Comparison between one factor at-a-time (left) and DoE (right) approaches.

First of all, this method is not precise: although the obtained solution can appear at first glance the best available one, OFAT methods are not able to take into account the dependency between two or more parameters. In particular, OFAT methods contemplate a hit-and-miss scattershot sequence of experiments from which it may not always be possible to estimate interactions between the variables. Moreover, OFAT methods are not able to "explore" the entire design field: changing only one parameter at a time means that the variations are captured only along preferential directions and not across the whole domain.

In order to understand why OFAT methods are not reliable, let us look at [Figure 6.1](#): the two plots refer to a very simple 11-runs experiment in which two input variables are varied during each run; each of the variables can assume four different discrete values. If an OFAT approach is adopted, parameter #1 is varied first while parameter #2 and #3 are kept constant; once the optimal value of parameter #1 which maximizes the output is found, the latter and parameter #3 are fixed and parameter #2 is varied until a new optimal condition is found; same procedure for the variation of parameter #3. This procedure requires time and can lead to wrong results since it ignores what can happen when more parameters are modified simultaneously. In other words, OFAT approach does not give a full idea of the response when more factors are changed at the same time. DoE methods, instead, allow to change multiple variables at once: the 5-runs of the experiment can thus be prepared in a better-organized scheme which covers a bigger part of the design field and is able to predict the optimal conditions more accurately. Statistical methods can then be used to analyze the trend of the various solutions and identify which combination of input variables can optimize the output.

Design of Experiments has been extensively studied in the literature and still represents an interesting field for research. Usually, the values that each variable can assume are organized into different discrete levels and range from a minimum

to a maximum. Levels and parameters are then manipulated at the same time to create the so-called DoE matrices. Different design methods are available to construct the DoE matrices: they are rigorously defined by statistical methods and their implementation can be done through computational algorithms. The aim of this section is to give a brief description of the most used DoE methods in the industry.

6.1.1 Design methods

In deciding which DoE scheme to use, the goal is to cover the design field as much as possible in order to gain as much information as possible about the output parameters with the lowest possible experimental effort. An additional requirement is that the set of points sampled provide a representative picture of the entire design space. Different DoE methods have been developed to fulfill these requirements. The choice about which to use depends on different variables such as time, computational resources available, how much is already known about the problem, etc.

It is not easy to classify all the DoE design methods since different theoretical approaches have been used for their formulation. It is however possible to define two major categories: orthogonal designs and random designs [37]. Orthogonal design require that the input variables are statistically independent: in other words, each input variable is uncorrelated to the others and can be varied independently. Among orthogonal designs, the most important ones are:

- full factorial designs: they take into account every possible combination between the input parameters. The total number of sampling points can be obtained as the product of the number of discrete levels of each input variable. In the case of [Figure 6.1](#), for example, where each input variable is discretized into four levels a full factorial design would require $4 \times 4 \times 4 = 4^3 = 64$ different experiments. Full factorial designs are very reliable since they basically cover the entire design space. Nevertheless, the high number of sampling points requires an enormous amount of experiments which, in the majority of the cases, cannot be performed;
- fractional factorial designs: only a fraction of the sampling points produced by the full factorial design is used. The sampling points are chosen in such a way that they are able to provide information about the most important features of the problem studied. Fractional factorial design reduces the amount of experiment runs, but only the most important correlation between output parameters are captured: it is therefore less reliable than the full factorial design;
- Response surface methods (RSM): the goal of the RSM approach is to develop a statistical second-order model that describes a continuous curve or

Table 6.1: Overview of the most adopted DoE schemes in engineering applications.

| response surface methodology | factorial design |
|-------------------------------------|---------------------------|
| Box-Behnken | full factorial |
| central composite | fractional factorial |
| random design | Taguchi design |
| orthogonal array | Taguchi orthogonal arrays |
| latin hypercube | |

surface which connects the measured data (the output variables) taken at strategically important places in the experimental window, i.e. at important combinations of the input parameters values. In other words, RSM consists in performing sequential experiments to reach an optimum, using only some important variables selected after a preliminary screening design. After the DoE is performed, linear regression is used, sometimes iteratively, to obtain results. Among RSM methods, one can mention Central Composite design and Box-Behnken design.

- Taguchi orthogonal arrays: this design method consists in testing pairs of combinations of the input variables. This allows for collection of the necessary data to determine which factors affect the output with a minimum amount of experimentation. The Taguchi method is best used when there are few interactions between variables, and when only a few variables contribute significantly to the output.

On the other hand, in random designs the choice of the sampling points is based on a random process, which is another widely used DOE method. The most used random DOE method is the Latin Hypercube Design (LHD).

Latin hypercube sampling is a statistical method for generating a sample of plausible collections of parameter values from a multidimensional distribution. In statistical sampling, a square grid containing sample positions is a Latin square only if there is one sample in each row and each column. A Latin hypercube is the generalization of this concept to an arbitrary number of dimensions, whereby each sample is the only one in each axis-aligned hyperplane containing it. When sampling a function of N variables, the range of each variable is divided into M equally probable intervals. M sample points are then placed to satisfy the Latin hypercube requirements; this forces the number of divisions, M , to be equal for each variable. This sampling scheme does not require more samples for more dimensions (variables); this independence is one of the main advantages of this sampling scheme. Another advantage is that random samples can be taken one at a time, remembering which samples were taken so far.

The main advantages of the DoE approach have been discussed in this section. Giving a detailed description of the methodology and the statistical approach behind each design method goes beyond the scope of the thesis. More information can however be found in Ref.[38].

6.2 Gear shift and surge

In order to understand the onset of compressor surge during a gear shift, consider a turbocharged gasoline engine. When a turbocharged engine is operating at design conditions, the engine is taking in a certain amount of airflow and the turbocharger is raising the pressure level of the flow (boost). That means that the turbocharger is working in proximity of design conditions, at the desired mass flow and pressure ratio. Once the throttle plate is closed, the turbine wheel is kept rotating at high rotational speed due to the high inertia of its components: the compressor, thus, continues spinning and continues compressing air. The air mass flow, however, has been abruptly decreased due to the obstruction created by the closed throttle plate. The compressor compresses thus airflow that can not be fed into the engine: this causes an increase in pressure across the engine intake manifold upstream the throttle plate. This condition of high pressure and low mass flow inside the turbocharger favors the onset of surge: the most critical condition is reached during a gear shift because the airflow towards the engine cylinders is stopped for a small fraction of a second. During this small amount of time, the excess flow is obstructed by the presence of the closed throttle plate and is reversed back to the compressor intake. A schematic overview of the phenomenon is shown in [Figure 6.2](#).

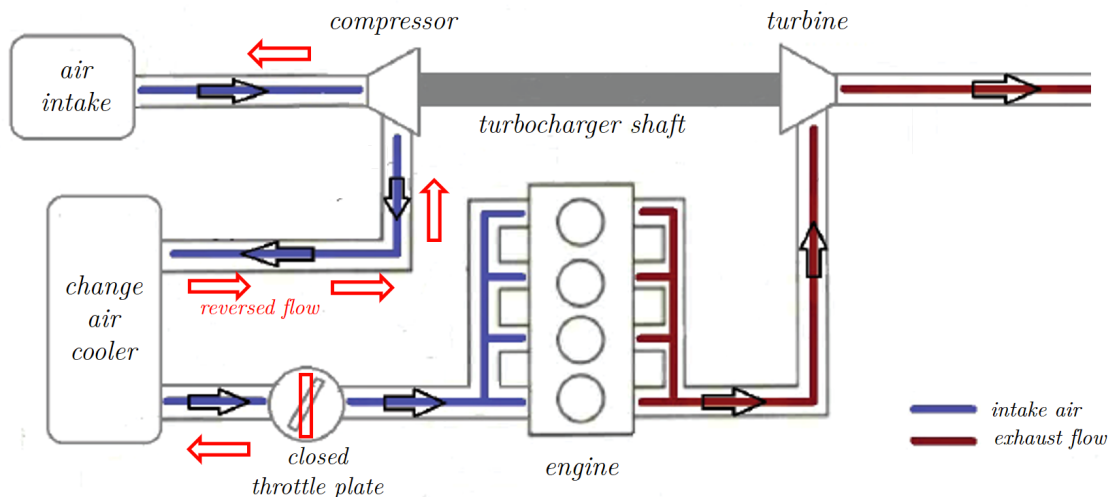


Figure 6.2: Compressor surge, also known as "turbo flutter", during a rapid gear shift on a gasoline engine.

The phenomenon here described is also known as turbo-flutter among the automotive enthusiasts [39]. When the compressor approaches surge, the flow separates from the impeller blades other than reversing back to the compressor intake. This creates a "fluttering" sound which can be clearly heard by the driver anytime he is performing a gear shift or he is rapidly decelerating.

Compressor surge is not a benign phenomenon for the engine. Flow instabilities and vibrations connected with flow stall and reversal can deteriorate the integrity of the turbocharger components: bearings and rotating components, in particular, can be seriously damaged.

This discussion is strictly valid only for gasoline engines. Diesel engine vehicles, in fact, are not equipped with a throttle plate: the power output is controlled through a regulation of the amount of fuel injected into the combustion chambers. Gear shift, however, remains a critical condition for the onset of compressor surge due to the abrupt changes in pressure and mass flow across the engine intake manifolds.

During a gear shift, the gas pedal is released for a short time lapse. As a consequence, the fuel rate into the engine cylinders is quickly ramped from the nominal value to zero, causing also a rapid decrease in engine torque. After the gear has been shifted, the fuel rate returns to its nominal value.

During this short Δt , both turbine power and rotational speed decrease due to the reduction in temperature and mass flow rate of the air/fuel mixture exhausted by the engine. Being the compressor driven by the rotation of the turbine, a gradual shift from design point to lower mass flows and pressure ratio can be observed on the compressor map. If the process is not adequately controlled, the surge limit can be overcome and the compressor can encounter surge. Furthermore, the timescale required for emptying the inlet manifolds and pipes between compressor and engine cylinders is lower than the one which characterizes the fuel ramp: a higher back pressure than the one measurable during steady operation of the turbine can thus be observed.

6.2.1 Blow-off valves

Blow-off valves (BOV) are used on gasoline engines to avoid the onset of surge during a rapid release of the accelerator, i.e. during a gear shift. Its operating principle is simple and it is shown in [Figure 6.3](#). They are fitted between the turbocharger and the throttle body. The closer to the throttle body, the better, as it will increase the response to mitigate surge.

Basically, they act as pressure relief valves. The BOV valve, represented by a spring-piston system in [Figure 6.3](#), is connected to the section downstream the throttle plate by a vacuum hose. Once the throttle plate is closed, the pressure difference between the zone downstream and upstream the throttle plate becomes very high: the resulting pressure differential moves the blow-off valve and allows the

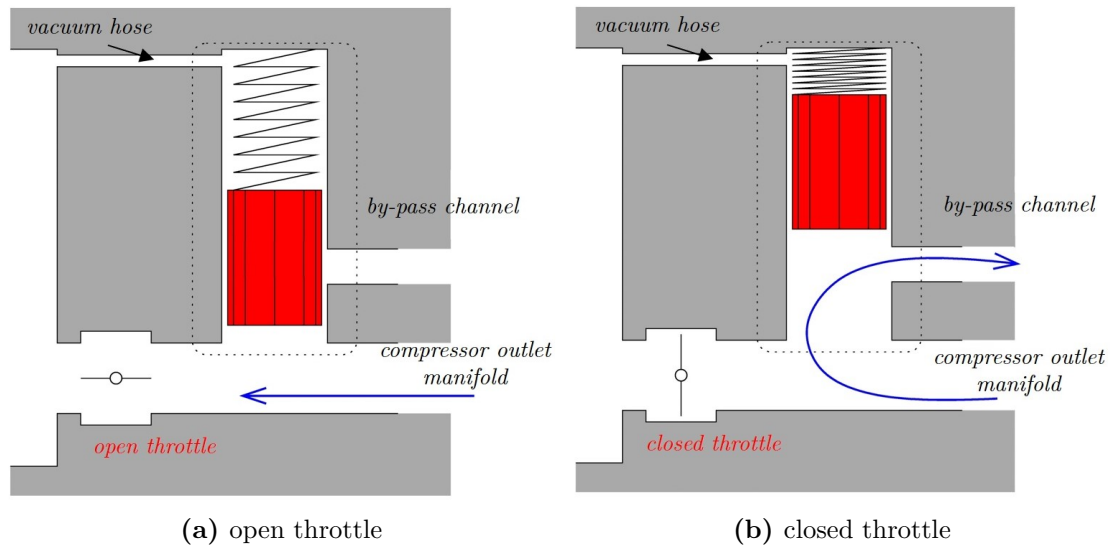


Figure 6.3: Working principle of a blow-off valve.

flow to deviate into a bypass channel. The excess flow from the compressor is thus either vented into the atmosphere or recirculated into the intake upstream of the compressor intake.

Every blow-off valve should be able to quickly open the channel as soon as the throttle pedal is released and, at the same time, to close and seal quickly when the throttle is open again after the gear change has been performed.

6.2.2 Ported shroud

It has already been discussed ([chapter 5](#)) that the ported shroud is implemented on modern turbocharger configurations to mitigate the effects of flow reversal during surge and extend the operational range of the compressor beyond the surge line.

On a conventional car or truck, ported shroud compressor covers can be used to mitigate both turbo-flutter and the onset of flow reversal during a gear shift. In particular, the shroud cavity can be used to collect the reversed flow and redirect in the direction of the main intake flow.

Unlike blow-off valves, whose design is more suitable for gasoline engines, ported shroud configurations can be adopted also on Diesel turbocharged engines.

6.3 Ported shroud design optimization

As discussed in the previous paragraphs, the best way to mitigate the effects of surge and to delay its onset as far as possible is to optimize the compressor design. In particular, on ported shroud configurations, the design optimization of the ported

shroud cavity becomes of fundamental importance to avoid turbo-flutter during a rapid gear shift. Ported shroud cavities are usually characterized by a complex design where lots of geometrical parameters come into action: small changes in the axial position of the ported shroud slot, for example, can significantly affect the performance of the compressor near the surge line.

Given the high number of geometrical parameters defining a ported shroud design, a systematic approach must therefore be followed when coming to geometry optimization. The best available way to optimize the design of engine components is to create different prototypes of the component under analysis: in each prototype, the value of one or more parameters has changed within a well defined range of values. These parameters may be, for example, the axial length of the recirculation cavity for a compressor with ported shroud or the length in radial direction of the diffuser.

The development and test phases of these prototypes obviously require a high cost. It is therefore necessary to make the optimization process as efficient as possible, either by choosing the most important parameters for analysis, or by trying to develop various prototypes capable of capturing both the best and worst scenarios.

6.3.1 Experimental setup

The DoE approach, widely spread in engineering, is used by big automotive companies to optimize the design of the most critical components. This philosophy has also been adopted in Scania CV AB for various projects. For the purposes of the thesis, the analysis of the experimental work carried out by the NMGG group about the optimization of the ported shroud geometry offers lots of interesting insights [40]. The DOE philosophy has been used to create 13 different covers for the C292 compressor, each presenting a different ported shroud geometry. The C292 compressor is different from both the compressors analyzed in this report, even if its geometry resembles the Scania one.

Three geometrical parameters characterizing the ported shroud design have been changed for the creation of the 13 covers. They are, namely:

- height of the cavity slot in the vicinity of the impeller blades;
- axial position of the ported shroud in relation to the lower wall of the compressor shroud;
- angle of the cavity slot in the vicinity of the impeller blades.

A schematic representation of these three parameters is illustrated in [Figure 6.4](#). The picture refer to a modified design of the Scania compressor, but it is also representative of the case here under analysis.

The DoE setup was based on a Box Behnken method. The three aforementioned parameters have been varied to create 13 different covers with different ported shroud geometries. Each cover has then been mounted on a 650 hp engine driven truck in order to test its response to surge.

6.3.2 Experiment and results

The aim of the experiment is the evaluation of surge occurrence during a gear downshift. As already described extensively, surge can arise every time the throttle pedal is released. Downshift can be a critical situation for heavy trucks when driving uphill at full engine load. If the truck cannot hold the vehicle speed, engine speed will start to drop. In order to preserve power and fuel, the driver perform a downshift: the reduction in engine speed can be so rapid to alter both pressure distribution and mass flow rate inside the engine manifolds. Compressor surge can arise and eventually damage both compressor bearings and impeller.

In order to choose the best design for the ported shroud, each geometry has been tested. The experiment consisted in four phases, each of them repeated for different engine shaft speeds and for all the 13 prototypes:

1. acceleration of the truck up to 12th gear;
2. application of the retarder¹ at full throttle; engine speed starts to decrease;
3. after an evaluation of the engine shaft speed, the gear is shifted down. If the fluttering sound that always accompains surge is detected, the engine torque ramp is decreased.
4. repeat the 3rd step until no surge can be detected.

The results showed that the best surge design is when the ported shroud slot is positioned at the corresponding position of the blade leading edge along the z-axis. The optimal slot width has been found to be about 3 mm.

In addition, this design is the best one in terms of gear change time, but still higher than the desired one of 0.2 s.

¹ The retarder is a deceleration system used to generate a resistant torque above a certain number of revolutions. It is usually implemented on trucks to guarantee a constant speed while driving down a hill or slow them down.

6.4 Numerical DoE

Results of the experiment performed in Scania CV AB showed that it is possible to optimize the ported shroud design in order to improve the response of the compressor to the surge. As highlighted in the former section, the experiment focused on observing the behavior of the compressor during a gear change. This experience, although fruitful, is however expensive, and repeating it for every different design of the compressor would require a huge amount of resources in terms of both time and money.

The attention therefore moves towards the field of Computational Fluid Dynamics: the development of a similar experience by numerical means would allow the obtaining of a reliable solution in the face of a considerable reduction in costs. The CFD approach, however, requires a certain amount of simplifications: it is not possible to meticulously replicate the experience of [section 6.3](#) since a simulation on the entire powertrain system would require enormous computational resources.

The aim of the next section will thus be to investigate whether is possible or not to develop a simple CFD model for the compressor which can predict the best design of the ported shroud cover in terms of surge response. Furthermore, results will be analyzed in order to see whether or not it is possible to observe similar trends to the experimental ones. In detail, this study represents a further assessment about the effectiveness of the Menter SST $k-\omega$ RANS model to predict compressor performance during surge and to provide useful information for design optimization.

6.4.1 Geometry

CFD simulations have been performed on the Scania compressor. Although different, its design resembles the C292 one. The original version of the Scania compressor does not provide for the recirculation cavity in the shroud. The compressor design has therefore been modified with the insertion of a ported shroud whose design is parameterized in order to allow a study of the effect of a change in geometry on performance, in line with what was done in the experiment of [section 6.3](#). Ansys Design Modeler has been used for the design modifications. The resulting design is shown in [Figure 6.4](#). The figure also highlights the three geometric parameters that can be modified during simulation setup. These parameters correspond exactly to those that have been varied to generate the 13 covers of the experiment, i.e. height of the cavity, axial position of the ported shroud inlet and angle of the cavity. The value assumed by each parameter can be easily controlled on both Ansys Design Modeler and the parameter set window of Ansys Workbench. The addition of the ported shroud increases slightly the total number of mesh cells for the compressor in relation to what discussed in [chapter 4](#). The cell number increase can be estimated in approximately 5 millions, depending on the ported shroud design.

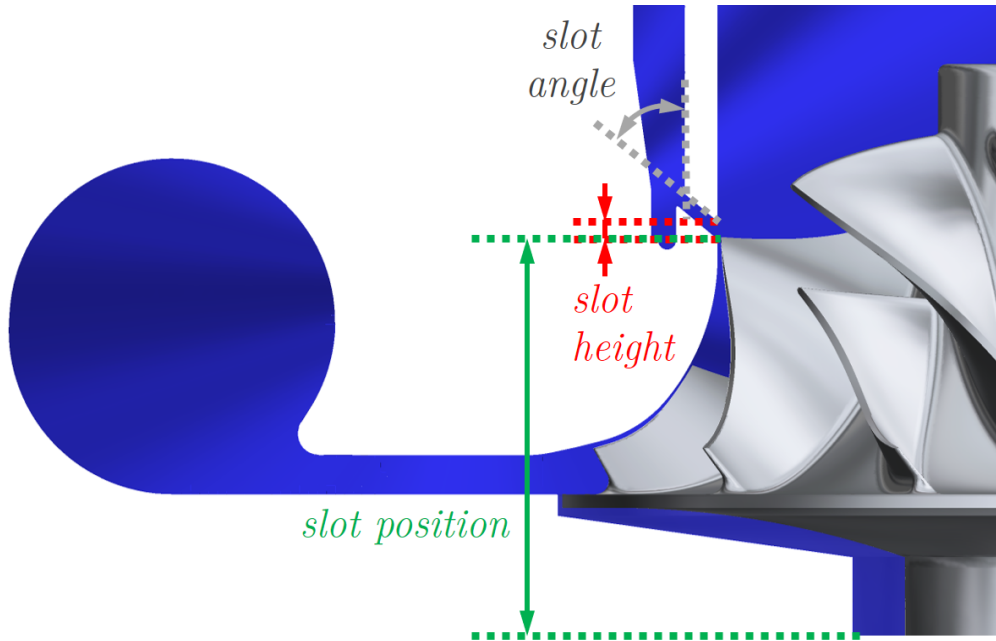


Figure 6.4: Detail of the parametric ported shroud design.

6.4.2 Steady state simulations

Steady state simulation have been run in order to initialize the problem and identify variables and trends which could be useful for monitoring the transient simulations and the outcome of the numerical DoE experiment. Due to the variability of the ported shroud geometry, steady state simulations were performed only on the actual Scania compressor geometry (no ported shroud).

Boundary conditions are specified in [Table 6.2](#). Simulations were run for three different speedlines (50000, 70000 and 90000 rev/min); the lowest value of the outlet corrected mass flow has been set to 0.06 kg/s in order to capture also the deep surge field. Inlet total pressure and temperature values match the reference standard atmosphere ones: actual and corrected mass flow assume thus the same value for these simulations.

Turbulence model adopted for the solution is the Menter SST $k - \omega$ model. The walls are assumed to be adiabatic and the no-slip condition, i.e. $\vec{u}|_{wall} = \vec{0}$, is valid throughout the domain. Interfaces between moving and fixed domains are modeled through the stage/mixing-plane model, general connection model is instead used for the diffuser-to-volute interface. High resolution scheme is used to calculate the advection terms in the discrete finite volume equations, while the advection scheme adopted for the turbulence model equations is of the first-order type. The maximum number of iterations used for each design point is 250, and the 10^{-4} target for the convergence of the residuals is met for almost all design points. Anyway, when the

Table 6.2: Boundary conditions for steady state simulations

| | |
|----------------------------|-------------------|
| inlet total temperature | 298,15 K |
| inlet total pressure | 100 kPa |
| outlet corrected mass flow | 0.06 to 0.36 kg/s |
| impeller wheel speed | 50000 rev/min |
| | 70000 rev/min |
| | 90000 rev/min |

convergence criteria is not met, residuals do not go over 5×10^{-3} .

Surge indicators

Although not able to predict the correct behavior of the flow when surge is approaching, steady state simulation provide good indicators about the onset of surge and, in particular, deep surge. Unlike the on-truck experience, in fact, it is not possible to detect surge by human ear when dealing with numerical simulations: other parameters must thus be investigated. Deep surge involves flow reversal towards the direction of the inlet. The reversed flow, whose pressure level has been previously increased, has also raised its temperature level.

This implies that the average temperature T_1 over the area of the inlet-to-wheel

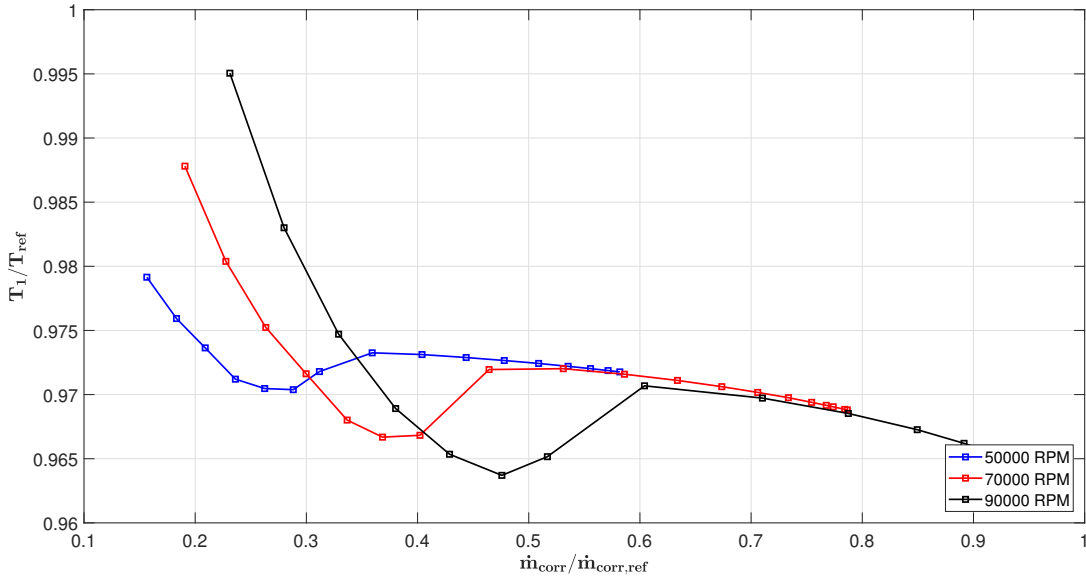


Figure 6.5: Temperature variation at the inlet-to-wheel interface in function of the inlet corrected mass flow.

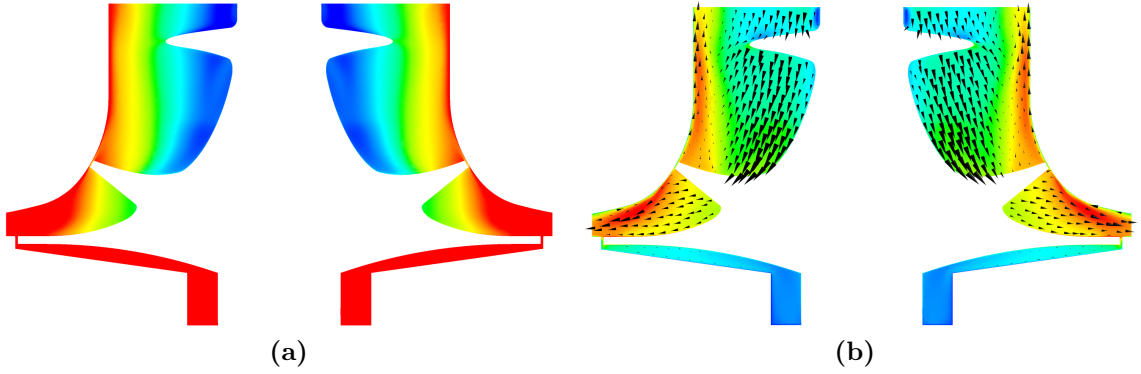


Figure 6.6: Temperature **a)** and Mach number (stationary frame) **b)** fields evaluated at 50000 rev/min and $\dot{m}_{corr,out} = 0.06$ kg/s over the wheel domain. The backflow recirculates in proximity of the inlet pipe wall.

interface, i.e. in proximity of the inducer, should increase considerably due to the interaction between the mainstream flow and the reversed one, which is warmer. The higher the raise in temperature is, the greater the drawbacks related to surge will be.

This behavior is clearly visible in [Figure 6.5](#) which shows the trend of the average temperature measured at the inlet-to-wheel interface in function of the corrected mass flow for three different impeller rotational speeds. In both cases, the temperature raises at very low mass flow rates, which is a clear evidence that the compressor is experiencing deep surge. The temperature, however, does not immediately increase as soon as the compressor encounters surge, but a slight decrease can be initially observed as the mass flow rate decreases; only after a minimum temperature is reached, the temperature starts rising. In addition, this behavior becomes more perceptible at high rotational speeds.

Due to this non-monotonic trend at decreasing mass flow rates, inlet-to-wheel temperature T_1 does not represent a good parameter for evaluating the onset of surge. Better indications can be retrieved by looking at the temperature field on the meridional XZ plane for a near-surge design point, as shown in [Figure 6.6a](#). It can be noticed that the high-temperature reversed flow generates recirculation zones in proximity of the inducer section which extends from a certain percentage of the inlet-to-wheel interface radius up to the inlet pipe wall. The blockage induced by these recirculation zones restricts the flow passage, generating a nozzle-like streamtube: the mainstream flow is thus accelerated ([Figure 6.6b](#)) and both pressure and temperature decrease. At moderate mass flow rates below the surge line, recirculation is small and the acceleration of the mainstream flow prevails over the temperature increase induced by the reversed flow: that explains why T_1 initially decreases with decreasing mass flow. Once the mass flow is further decreased, the recirculation zone expands over a larger fraction of the inlet-to-wheel radius and the average temperature raises

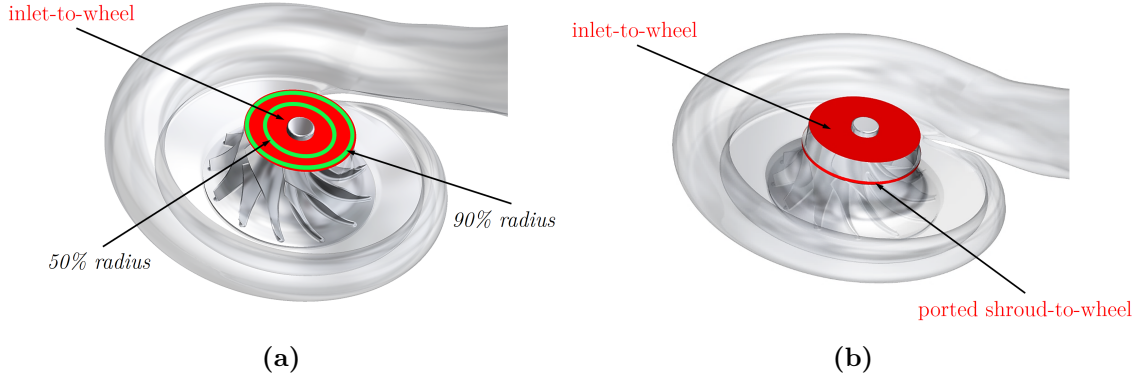


Figure 6.7: **a)** location of the temperature evaluations at the inlet-to-wheel interface; **b)** location of the interfaces for the calculation of the T_{PS}/T_1 ratio.

over the section.

These observations are summarized in Figure 6.8. On the left graph, temperature is evaluated as a length average along two circumferences at 50% and 90% of the inlet-to-wheel interface radius for all three rotational speeds, as shown in Figure 6.7a. At 50% of the radius, the temperature initially decreases with decreasing mass flow rate and reaches a maximum after which the flow slightly heats up for very small mass flows. At 90% of the radius, instead, the average temperature increases rapidly.

The ratio between the two temperatures $T_{90\%}/T_{50\%}$ provides thus a good parameter with regards to surge prediction, as highlighted on the right graph of Figure 6.8. The ratio immediately raises up once the reversed flow reaches the inducer: the higher the ratio, the worse in terms of surge severity.

Similar conclusions can be reached whenever the compressor design is changed with the addition of a ported shroud recirculation cavity. In this case, the largest part of the hot reversed flow recirculates in the shroud cavity and it is reintroduced in the inlet pipe immediately afterwards: an equivalent surge indicator to $T_{90\%}/T_{50\%}$ becomes thus T_{PS}/T_1 , i.e. the ratio between the averaged temperature measured at the ported shroud-to-wheel interface and at the inlet-to-wheel one (see Figure 6.7b).

If a ported shroud design is considered, a second surge indicator can be introduced: basically, it is the ratio between the mass flow evaluated at the ported shroud-to-wheel interface and the one evaluated at the inlet-to-wheel interface. Once the reversed flow reaches the ported shroud cavity, the velocity measured at the ported shroud-to-wheel interface progressively decreases and changes its direction. Conventionally, the mass flow rate ($\dot{m} = \rho \vec{u} \cdot \vec{n} A$, where A is the area) is considered positive when concordant with the direction indicated by the unit vector orthogonal to the surface, negative otherwise. Flow reversal can thus be easily estimated by looking at the sign of the mass flow: in particular, being the mainstream flow directed always in the same direction, the change in the sign of the mass flow ratio

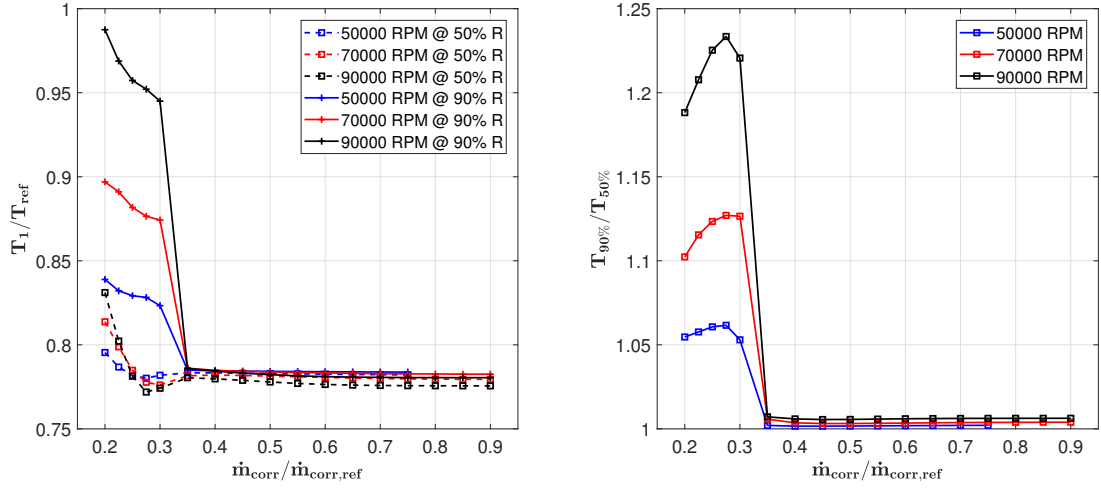


Figure 6.8: a): variation of temperature at two different radial locations of the inlet-to-wheel interface; b): ratio of temperature averaged along two different radial locations of the inlet-to-wheel interface.

previously defined can be a good estimation for surge.

6.4.3 Numerical DoE setup

The parametric design of the shroud recirculation cavity has been used to create 16 different covers. The Design of Experiment approach has been adopted to create the different geometries: the three geometrical parameters introduced in section 6.3 are thus varied at the same time to maximize the coverage of the design field.

Dakota DDACE package [41] has been used for the generation of the sampling points across the design field²: in particular, a Latin Hypercube sampling method has been adopted.

The final result, comprehensive of the design field, is shown in Figure 6.9. The edges of the cube on the upper-left figure identify the design field: each of the three parameters, in fact, ranges from a minimum to a maximum value. Minima and maxima for all design parameters cover larger ranges of variability with respect to the DoE setup used for the experiment of section 6.3.

All the 16 sets of parameters have then been introduced on the Parameter set window of Ansys Workbench for the pre-generation of the new geometries via Ansys Design modeler.

²I thank Scania NXPS group for the help provided on the DoE setup.

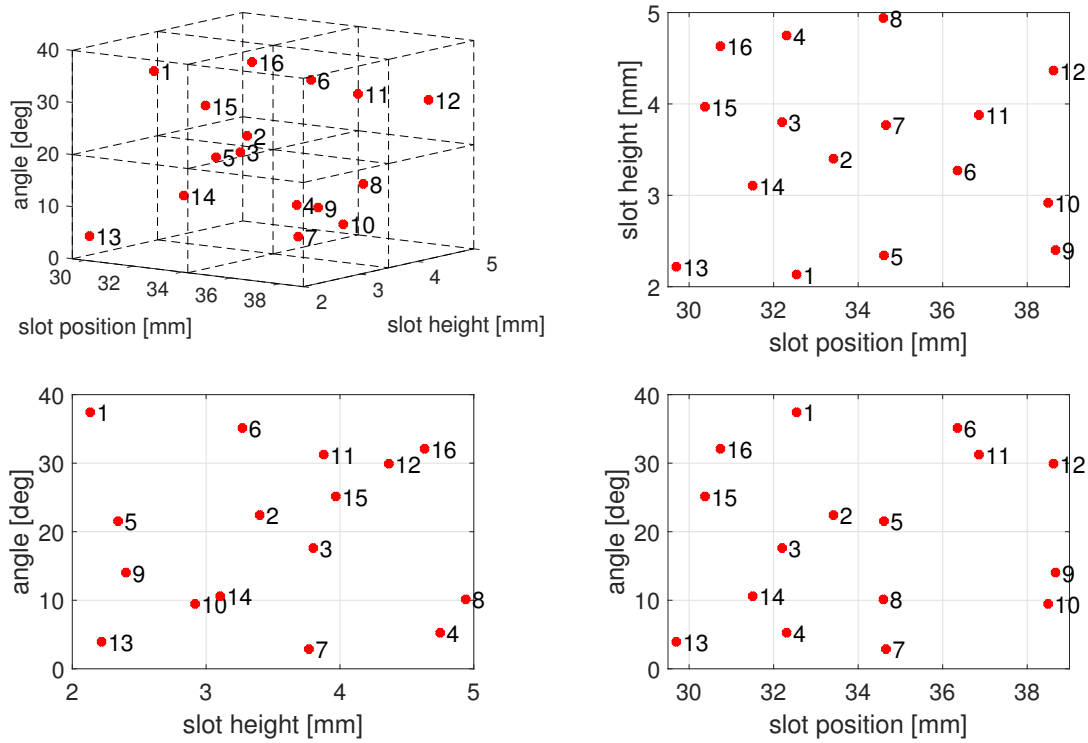


Figure 6.9: Sampling points for the numerical DoE analysis.

6.4.4 Transient simulations

Transient simulations were performed for each of the 16 different ported shroud geometries of the Scania compressor. General settings are kept constant for all simulations, only input geometries and meshes are changed. Since the simulations are limited to the compressor only, it is not easy to develop an appropriate set of boundary conditions in order to emulate the flow conditions inside the turbocharger unit during a gear shift.

The solution adopted for the case under analysis is illustrated in [Figure 6.10](#): it involves a linear reduction in both outlet corrected mass flow and wheel speed from initial design conditions, i.e. 0.26 kg/s and 90000 rev/min. Initial conditions are kept constant during the first 400 iterations. After a ramp of 0.2 s, both outlet corrected mass flow and wheel speed are stabilized to a constant value for further 400 iterations.

A constant time step has been used for all simulations: its value has been fixed to $6.7 \cdot 10^{-5}$ s, corresponding to approximately 36° of wheel rotation per iteration at 90000 rev/min. Such choice leads to high Courant numbers ($Co \simeq 114$) due to the high local velocity reached by the flow over some parts of the domain and the small

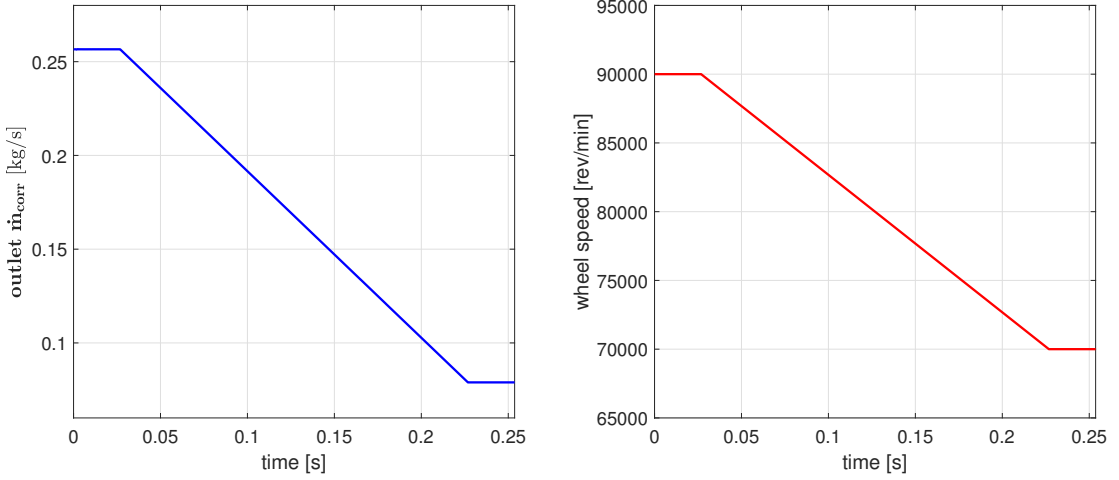


Figure 6.10: Time variation for the transient simulations. **a)**: ramp for the outlet corrected mass flow; **b)**: ramp for the impeller wheel speed.

average length of the mesh cells. Since Ansys CFX is an implicit solver, it is not strictly required to have a small Courant number (order of unity) for stability, as is needed with explicit solvers. Using smaller Courant number is however suggested to accurately resolve transient details. The reason behind the choice of a so large time step lies on time requirements and the limited amount of computational resources available. Smaller time steps, in fact, would enormously increase the total time required to perform a simulation.

For example, a stage interfaces MRF transient simulation for the modified Scania compressor geometry here analyzed would require approximately one day and a half to be terminated if run on 128 nodes of a Scania cluster with the time step above introduced. Months can therefore be needed to run an entire series of 16 transient simulations, as done for the DoE work here analyzed, with a smaller time step.

The total time for the simulation is 0.2536 s; the time evolution for both outlet corrected mass flow and wheel speed can be summarized as follows:

| | t_0 | t_1 | t_2 | t_3 |
|-----------------------------|-------|--------|--------|--------|
| time [s] | 0 | 0,0268 | 0,2268 | 0,2536 |
| $\dot{m}_{corr,out}$ [kg/s] | 0,26 | 0,26 | 0,08 | 0,08 |
| ω [rev/min] | 90000 | 90000 | 70000 | 70000 |

Boundary conditions are specified at the inlet section in terms of total pressure ($p_0^0 = 100$ kPa) and total temperature ($T_0^0 = 298.15$ K): corrected quantities match thus the actual one since both p_0^0 and T_0^0 match the corresponding reference values for standard atmosphere. An implicit second order backward-Euler scheme is adopted for time discretization. Advective terms are instead discretized through a high resolution scheme. The convergence at each time step is defined by a target on the

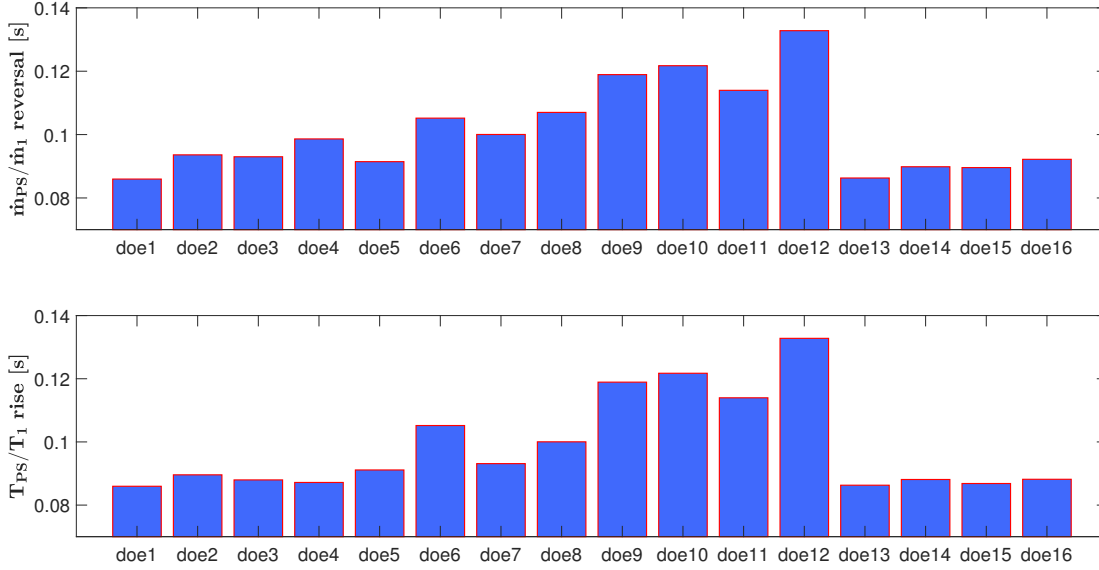


Figure 6.11: Reversal time for different DoE sampling points calculated by means of: **a)**: ratio of mass flow rates, **b)**: ratio of temperature.

maximum RMS value of the residuals. The threshold is set at 10^{-4} : once RMS residuals dropped below this value, the simulation has converged. The maximum amount of inner loop iterations for each time step is set to 10.

Regarding the fluid-fluid interfaces between static and rotating domains, i.e. inlet-to-wheel, ported shroud-to-wheel and wheel-to-diffuser, the stage/mixing plane model offer the best compromise in terms of accuracy of the results and computational time and is therefore utilized in this analysis. Running sliding mesh simulations with the transient rotor-stator interface model would raise the amount of computational resources needed to finish a simulation within a reasonable time.

6.4.5 Results

Surge indicators, i.e. the two ratios T_{PS}/T_1 and \dot{m}_{PS}/\dot{m}_1 , have been investigated for all the different ported shroud geometries. The aim is to evaluate which cover shows the best "resistance" to surge: in order words, the best design would delay surge inception as far as possible and, if possible, avoid flow reversal. The methodology differs from the one described in [section 6.3](#), but the goal remains the same: to find the best design able to delay or mitigate surge.

The bar diagrams of [Figure 6.11](#) illustrate a comparison between the different geometries in terms of flow reversal start time. The number of the sample along the horizontal axis refers to the nomenclature of [Figure 6.9](#). Reversal time is defined in two different ways on each graph. On the diagram above, the reversal time $t_{\dot{m}}$

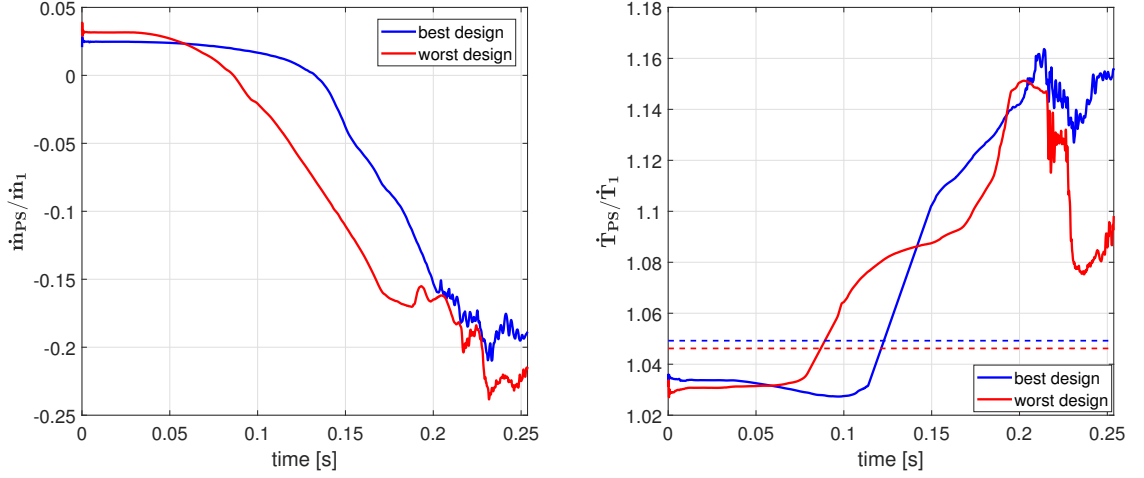


Figure 6.12: Variation of both surge parameters in function of simulation time for design n°12 (best design) and design n°13 (worst design). Oscillations can be observed after the end of the ramp: the flow has not the time to reach a stable condition during the 400 timesteps of the simulation. In addition, instabilities arise due to deep surge.

is defined as the time of the simulation at which the ratio \dot{m}_{PS}/\dot{m}_1 changes sign. Regarding the graph below, reversal occurs at the time t_T when the ratio T_{PS}/T_1 overcomes the value of the same parameter measured before the ramp and raised by 1.5%. In formulas, these two relation can be expressed as follows:

$$t_{\dot{m}} = \left\{ t : \frac{\dot{m}_{PS}}{\dot{m}_1} = 0 \right\} \quad (6.1)$$

$$t_T = \left\{ t : \frac{T_{PS}}{T_1} = (1 + 0.015) \cdot \frac{T_{PS}}{T_1} \Big|_{in} \right\} \quad (6.2)$$

where the subscript *in* denotes the initial conditions before the start of the ramp. The graphs clearly highlight that in both cases flow reversal is delayed when design n°12 for the ported shroud is adopted: both $t_{\dot{m}}$ and t_T , in fact, reach a maximum and flow reversal is delayed. On the other hand, design n°13 leads to the minimum values for both $t_{\dot{m}}$ and t_T , and could thus be assumed to be the worst design possible among the ones covered by this DoE evaluation. For the reasons just explained, design n°12 will be referred as the "best design" and design n°13 as the "worst design" in the following discussion.

Figure 6.13 shows the trend of both surge indicators for the two extreme designs: it is clearly visible that the "best design" delays drastically the decrease of the \dot{m}_{PS}/\dot{m}_1 ratio and the increase of the T_{PS}/T_1 one in comparison with the "worst design". It is interesting to notice that the initial value of the \dot{m}_{PS}/\dot{m}_1 ratio is higher for the "worst design" than for the "best" one. Being the geometry of the inlet pipe the same for all the DoE covers, \dot{m}_1 does not show huge variations from

case to case: this means that the mass flow rate \dot{m}_{PS} through the ported shroud at design conditions depends on the geometry of the latter. A possible explanation may relate to the volume of the recirculation cavity which changes depending on the considered design: long and voluminous designs of the cavity (like the n°13 one) will allow more fluid to flow through it, raising thus the \dot{m}_{PS}/\dot{m}_1 ratio.

Spearman’s correlation coefficient

The analysis of $t_{\dot{m}}$ and t_T shows that it is possible to design an optimal geometry of the ported shroud cavity which can improve the compressor response to surge. In particular, by comparing designs n°12 and n°13, i.e. the ”best” and the ”worst” one, it can be observed how the onset of flow reversal during deep surge regimes is drastically delayed if the inlet position of the cavity is moved towards the inlet of the compressor. In particular, if the cavity inlet is positioned in front of the impeller inducer, both $t_{\dot{m}}$ and t_T are maximized. The results therefore seem to confirm what was observed during the Scania gear shift test. However, it is necessary to generalize what has just been written by taking into account all 16 different designs and analyzing which of the three geometric parameters has the largest impact on the solution.

Spearman’s correlation coefficient r_s , also known as Spearman’s rho [42], facilitates this type of analysis. It represents a nonparametric measure of the statistical dependence between the rankings of two different variables. In other words, it assesses how well the relationship between two variables can be described using a monotonic function. This parameter becomes useful when the distribution of X_i and Y_i , i.e. the variables in consideration, is not normal or when the subpopulations of either X_i or Y_i do not have the same variance.

Spearman’s rho can assume values which range between -1 and $+1$. Sign and value of this parameter indicate respectively type and strength of the correlation: the plus sign indicates a direct proportional correlation, the minus sign indicates an inverse proportional correlation; values of r_s close to unity indicate a perfect correlation, while values close to 0 implicate a negligible correlation.

If a sample of n observations is considered, the n variables X_i and Y_i are used to calculate the Spearman’s rho in the following way:

$$r_s = \frac{\text{Cov} [\text{rg}(X_i), \text{rg}(Y_i)]}{\sigma_{\text{rg}(X_i)} \sigma_{\text{rg}(Y_i)}} \quad (6.3)$$

where $\text{rg}(X_i)$ and $\text{rg}(Y_i)$ are the ranks of X_i and Y_i , $\text{Cov} [\text{rg}(X_i), \text{rg}(Y_i)]$ is the covariance of the rank variables, $\sigma_{\text{rg}(X_i)}$ and $\sigma_{\text{rg}(Y_i)}$ are the standard deviations of the rank variables. If all n ranks are distinct integers, r_s can instead be calculated with

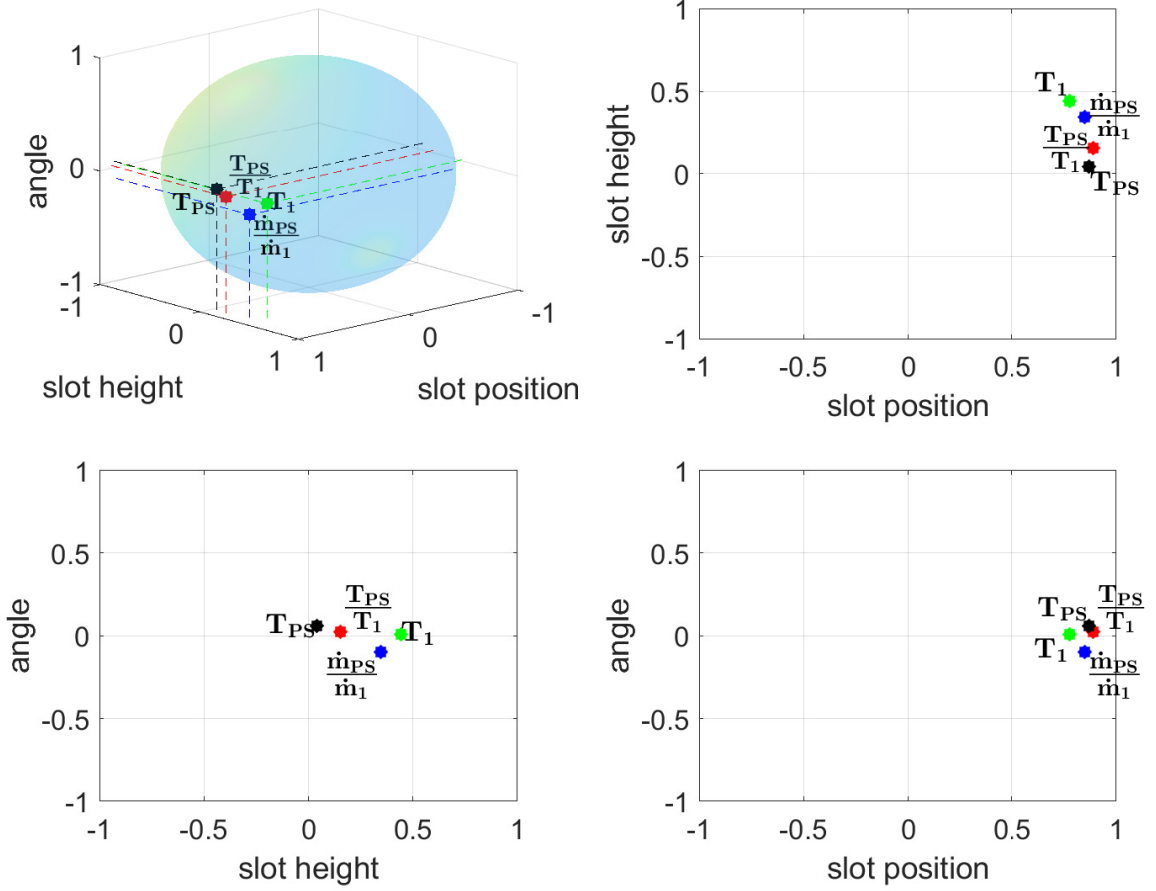


Figure 6.13: Correlation between reversal times ($t_{\dot{m}}$, t_T , t_{PS} and t_{w2i}) and design variables calculated by means of Spearman's rho r_s . Each of the three coordinates in the above-left figure identify the correlation coefficient evaluated for one of the three design variables. 2D dimensional views are provided for ease of read.

this expression:

$$r_s = 1 - \frac{6 \sum_{i=1}^n d_i^2}{n(n^2 - 1)} \quad (6.4)$$

where d_i is the difference between the two ranks of each observation.

For this numerical DoE study, the total number of observation is 16, X_i defines the values assumed by each of the three ported shroud geometry parameters depending on the cover design and Y_i the reversal time (either $t_{\dot{m}}$ or t_T) for each cover design.

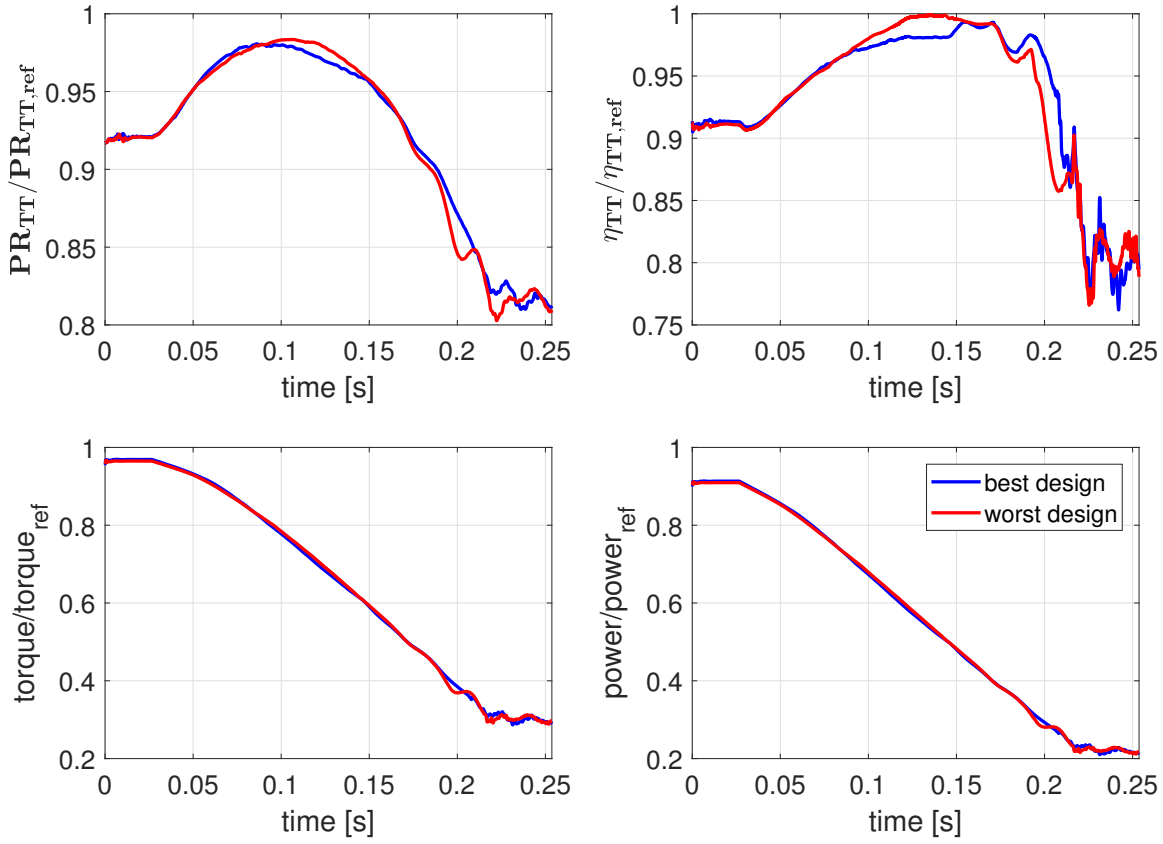


Figure 6.14: Variation in compressor performance during the ramp. On the row above: pressure ratio (left) and total-to-total efficiency (right). On the row below: compressor torque (left) and power (right)

Results of the correlation evaluation are shown in [Figure 6.13](#). Each axis identifies the values of the Spearman’s correlation coefficient depending on the set of variables used as X_i : for instance, the value of r_s which correlates the time t_m to the position of the ported shroud cavity is marked by a point along the ”slot position” axis. The same procedure is then repeated for the other two sets of variables, i.e. ”slot height” and ”slot angle”: the three obtained values of r_s identify therefore a point on the 3D space shown in the above-left graph of [Figure 6.13](#).

Together with t_m and t_T , other two parameters, t_{PS} and t_{w2i} have been investigated. They are defined in the same way of t_T , but they refer, respectively, to the temperature measured at the inlet of the ported shroud cavity (t_{PS}) and at the inlet-to-wheel interface (t_{w2i}). In formulas, they can be expressed as:

$$t_{PS} = \{ t : T_{PS} = (1 + 0.015) \cdot T_{PS}|_{in} \} \quad (6.5)$$

$$t_{w2i} = \{ t : T_1 = (1 + 0.015) \cdot T_1|_{in} \} \quad (6.6)$$

All the analyzed parameters show a strong positive correlation with the axial position of the inlet of the recirculation cavity: in particular, Spearman's rho reach a value close to 0.9 for both the two surge indicators $t_{\dot{m}}$ and t_T . This confirms what stated above: the position of the inlet of the cavity plays an important role in delaying the flow reversal and mitigating the effects of surge. The angle of the inlet section of the recirculation cavity has a negligible impact on the design: r_s is in fact close to zero for all four parameters. Weak correlation can be evaluated, instead, between surge indicators and the height of the inlet section of the cavity. In detail, only t_{w2i} and $t_{\dot{m}}$ show a perceptible dependence with this design variable: in any case, r_s settles on values lower than 0.5.

"Best" and "worst" designs have been further investigated in terms of performance. Figure 6.14 shows the trends of the main performance indicators during the ramp. None of them appears to be sensitive to the geometry of the ported shroud cavity: torque and power, in particular, decrease monotonically during the ramp and start showing appreciable oscillations before the end of it due (probably) to the incoming deep surge. The same behaviour can also be seen on pressure ratio and total-to-total efficiency³.

6.4.6 Fields

In Figure 6.15, the variation of the Courant number over the whole compressor stage is illustrated; the fields are shown both at the beginning and at the end of the ramp. The analysis is carried out only for the best design of the ported shroud, i.e. design n° 12: since the geometric changes between one design and the others are minimal, the considerations that will be drawn can be extended to the other DoE points.

As an implicit code, Ansys CFX does not require the Courant number to be small for stability. However, for transient calculations, one may need the Courant number to be small in order to accurately resolve transient details. In the case under analysis, Courant number reaches small values ($Co_{avg} \sim 60 \div 80$ over the domain) only at the end of the ramp. Higher values ($Co_{avg} \sim 100 \div 150$) can be calculated at the beginning of the ramp due to the higher flow velocity and impeller rotational speed. A gradual decrease in the average Courant number Co_{avg} could be expected as far as the ramp proceeds in time. In both cases, maximum Courant numbers can be evaluated along the blades contours, in particular the tip, because of the high local velocity and the accentuated local mesh refinement.

³Efficiency is defined for a well defined operating point of the compressor: thermodynamic variables are in fact utilized for its definition. In principle, to look at time variation of efficiency would not be physically correct.

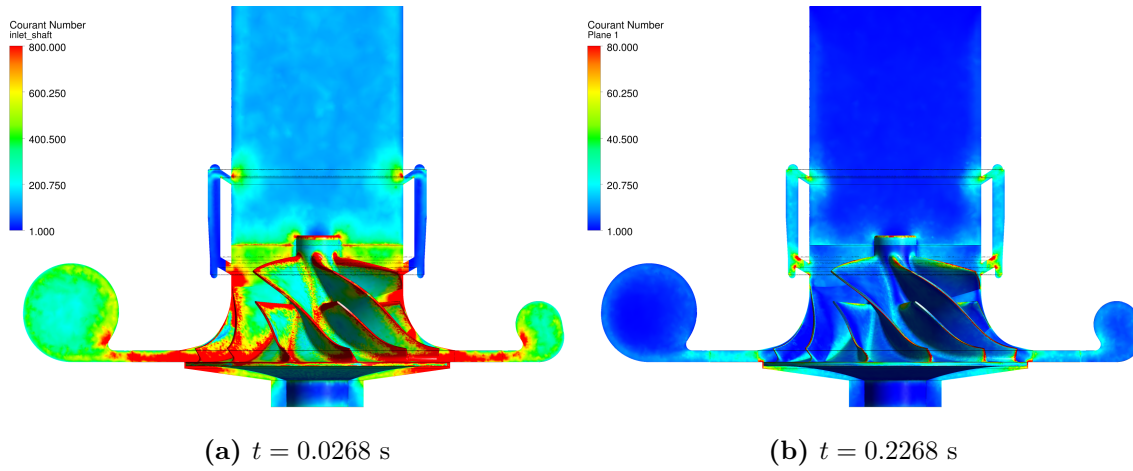


Figure 6.15: Courant number distribution over the computational domain at ramp start (a) and termination (b).

For this analysis, high values of the Courant number can be accepted since the focus is mainly on deep surge and backflow. More detailed surge evaluation would probably require lower Co_{avg} , a requisite that could be easily achieved by either decreasing the timestep or implementing an adaptive timestep. The drawback, of course, is the increased computational time required for the completion of each simulation.

Temperature and velocity fields along the meridional plane at $t = 0.1206$, that is at the time when the backflow enters the ported shroud cavity of the best design, are shown in Figure 6.16. The fields are shown for both best and worst design, i.e. for design n°12 and n°13.

By looking at the temperature field of Figure 6.16a and Figure 6.16b, one can notice that when the recirculation of the flow along the cavity for the best design starts, the latter has already been completed in the worst design. A proof of this lies in the higher flow temperature measured in the cavity of the worst design at $t = 0.1206$. The recirculation advance is also observable in the velocity fields at the same time instant. For the best design case (Figure 6.16c), the flow velocity is almost zero in magnitude and is oriented along the main flow direction; for the worst design case (Figure 6.16d), instead, higher velocity can be measured along the cavity in the opposite direction to that of the undisturbed flow. Furthermore, in the latter case, the backflow is returned to the mainstream flow and flows along the walls of the inlet pipe. This small amount of flow, highly turbulent and slower than the bulk one from the inlet, hits the tip of the blades, possibly anticipating the onset of stall.

The influence of the reflux on the flow field over the impeller can be observed in Figure 6.17 for both the best and worst design of the ported shroud. At the

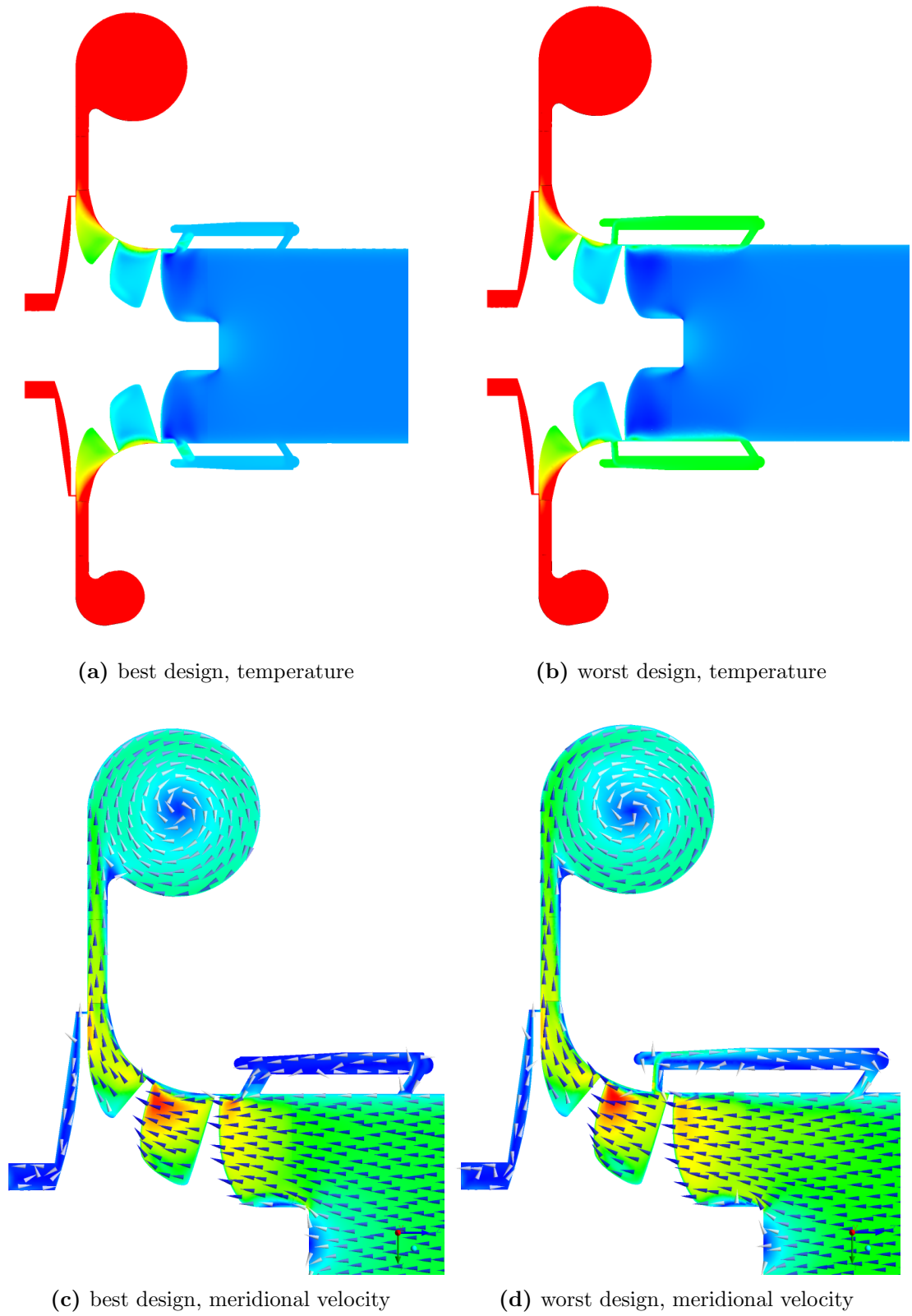
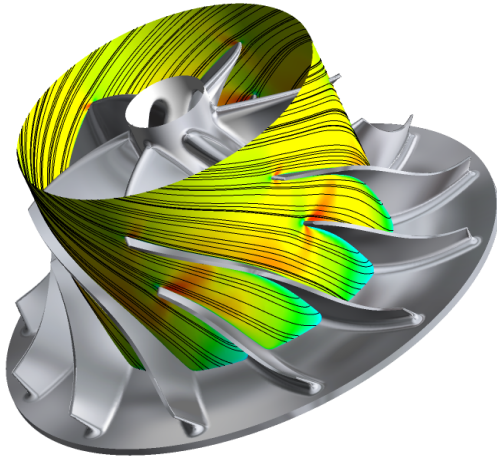
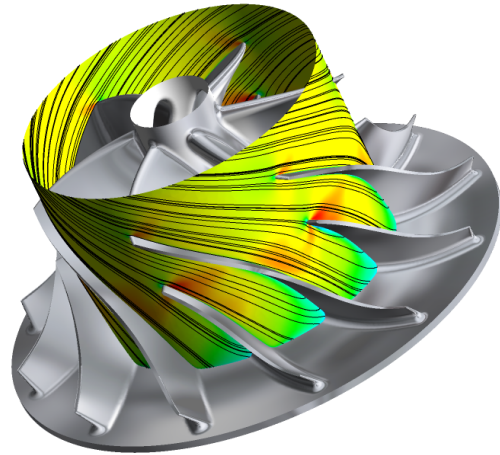


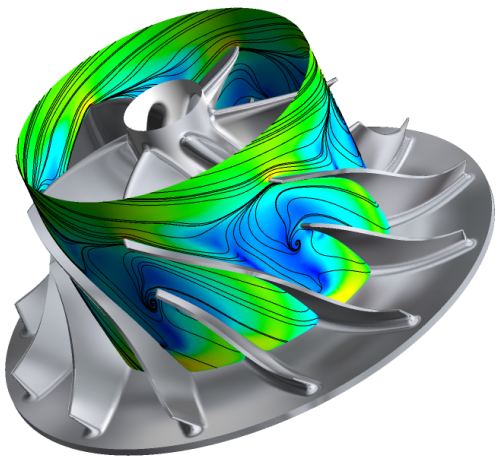
Figure 6.16: Temperature and velocity fields on the meridional plane at backflow inception for the best design ($t = 0.1206$ s).



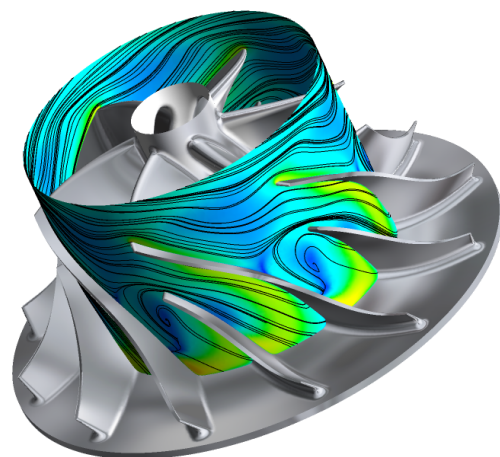
(a) $t = 0.0268$ s, best design



(b) $t = 0.0268$ s, worst design



(c) $t = 0.2077$ s, best design



(d) $t = 0.2077$ s, worst design

Figure 6.17: Velocity field and streamlines over the impeller at important time instants for both best and worst designs of the ported shroud cavity.

beginning of the ramp (Figure 6.17a and Figure 6.17b), the compressor is at near-design conditions and the streamlines are aligned with the surface of the blades. At the time $t = 0.2077$ s, streamlines diverge and are no longer aligned along the blades, as illustrated in Figure 6.17c and Figure 6.17d. The slowdown of the flow due to the decrease in the value of outlet \dot{m}_{corr} causes the angle of incidence at the blades leading edge to diverge from the optimal one, causing separation along the blades. In the worst design case, however, the deceleration happening upstream of the blades leading edge is much more pronounced. Although already started in both designs, the recirculation along the ported cavity is already at an advanced stage for the worst design case: the backflow, once re-introduced in the inlet pipe, reaches the blades increasing the entity of local flow instability and the extent of the stalled regions over the blades.

6.5 Concluding remarks

The DoE analysis showed that the most important geometrical feature to investigate for optimizing the design of the ported shroud cavity is the position of the inlet slot along the longitudinal axis of the compressor. The results were confirmed by the study of the correlation between geometrical design of the cavity and delay in the onset of backflow.

The optimal design of the ported shroud cavity requires the inlet slot to be positioned in correspondence of the leading edge of the impeller main blades: with such a design, deep surge is delayed and the backflow starts later to recirculate into the cavity.

These results matched the observations of the Scania on-track experiment: the optimization of the position of the inlet slot allows an improvement in surge response and gear shift time.

Finally, surge indicators T_{PS}/T_1 and \dot{m}_{PS}/\dot{m}_1 proved to be reliable enough to predict the onset of deep surge and backflow.

Chapter 7

Final remarks

In [chapter 5](#) the focus was on trying to identify the causes of the mismatch between performance obtained both by CFD simulations and by gas-stand experiments in terms of compressor map and efficiency curves for the HT compressor. The different setups there analyzed did not lead to a consistent reduction of the mismatch, especially with regards to efficiency. The investigation carried out in this thesis, however, can be seen as the starting point for future investigations on the performances of centrifugal compressors and on the optimization of the currently available CFD model.

Although the results of [chapter 5](#) may suggest the opposite, the possibility of using steady-state RANS simulations for predicting compressor performance is not to be discarded since other parameters here not investigated (resolution of the boundary layer mesh, for example) can affect the results. Future analysis would therefore be aimed at identifying those parameters or phenomena that may lead to an incorrect estimate of the performance and quantifying their effect on the results.

On the other hand, transient RANS simulations are useful to provide a qualitative idea of the backflow which appears in proximity of the impeller at deep surge conditions. These simulations also allow to carry out simple design optimization studies for identifying design parameters of the compressor able to delay the recirculation of the reflux inside the cavity of the ported shroud. In particular, the results of the DoE analysis carried out in [chapter 6](#) allowed the identification of an optimal design of the ported shroud cavity able to delay the onset of deep surge: the results of this study matched the experimental observations available in Scania CV AB.

CFD thus provides excellent tools which can be utilized to improve the understanding of the flow field developing inside the compressor and, in general, the turbocharger unit. The main problem related to CFD is the computational time required for the completion of each simulation: in addition to solving the appropriate balance equations on a discretized domain, the solver must also take care of compressing, extracting, sending and saving on disk the huge amount of produced

data. [Table 7.1](#) summarizes, in terms of computational time, the computational effort required by the clusters for successfully running each simulation: the first two lines refer to evaluations done on the HT compressor, the other two to the Scania compressor. All reported values refer to simulations performed on 120 cores on a Scania CV AB cluster.

By analyzing the reported values, it is clearly noticeable that the computational time required for the completion of each simulation constituted a considerable limitation to the smooth development of this thesis work: due to time restrictions, further planned investigations were not performed.

Table 7.1: Computational time for each type of simulation performed for this thesis work.

| | |
|-------------------------------|-----------------|
| steady-state simulations | 45 min - 1 hour |
| compressor map (3 speedlines) | 24 - 36 hours |
| transient MRF simulations | 36 - 48 hours |
| DoE (16 sampling points) | ~ 1 month |

Chapter 8

Limitations and future work

The results analyzed and discussed in this thesis are intended to be the starting point for future investigations on compressor performance and transient surge phenomena. Different limitations have however affected the outcome of the analysis: these are reported and discussed in the following paragraphs.

Steady-state simulations for performance analysis

The first limitation emerges from the use of total-to-static quantities for the evaluation of compressor performance. Although total pressure probes are hard to place in a gas-stand setup, it is highly suggested to conduct future investigations by using total-to-total quantities which are less sensitive to geometry variations, such as convergence/divergence of the outlet pipe, etc.

Steady-state simulations on the HT compressor highlighted that unsteady fluctuations in the flow variables can lead to wrong estimations of the separation zones over the impeller blades. Performing transient simulations at different operation points would be interesting in order to estimate how these fluctuations affect the compressor stage performance. For these simulations, the aim would be to monitor performance parameters during a small number of wheel revolutions at constant rotational speed and boundary conditions and evaluate whether the mismatch with experimental observations decreases or not. The use of Transient rotor-stator interfaces is highly suggested.

For the analysis on the HT compressor, the attention has been mainly focused on pressure and velocity fields. Isentropic stage efficiency, however, is strongly dependent on the temperature evolution over the compressor, as clearly highlighted in [Equation 2.9](#) and [Equation 2.8](#). Further studies should thus be done about the temperature field inside the compressor. In particular, removing the adiabatic wall assumption can drastically change the flow field inside the compressor and can lead to different outcomes from the one here obtained.

Final recommendations suggest to check accurately the correctness of the CAD

geometry imported in Design Modeler so that it matches as much as possible the actual geometry utilized in the gas stand and to rely, if possible, also on high-fidelity approaches like Large Eddy Simulations (LES) or Detached Eddy simulations (DES).

Transient surge investigation

The main limitation of the transient surge analysis on the Scania compressor was the use of stage/mixing-plane interfaces instead of a full sliding mesh approach. By doing so, all transient effects at the interface are lost and all circumferential gradients are mixed out and averaged. On the other hand, it would have been prohibitive to perform the ported shroud design optimization with a transient rotor-stator approach since it would have required enormous computational resources for the completion of each simulation. As a consequence, the analysis has been limited to the backflow that appears at deep surge regimes: pressure fluctuations and mass flow oscillations which characterize surge regimes have not been considered.

Secondly, the analysis here conducted has not been replicated experimentally yet. The next step would involve a comparison between the results of this numerical DoE analysis and experimental observations obtained from gas stand tests with the same setup utilized for the CFD simulation.

Finally, it would also be suggested to enlarge the DoE field: moving the axial position of the ported shroud slot further upstream, for example, could possibly delay the backflow and improve compressor stability in deep surge regimes. Other geometrical features of the ported shroud (length or volume of the cavity, for example) could also affect the final results: a new DoE study which covers also these parameters could lead to new interesting results.

Bibliography

- [1] Cox P. M., Betts R. A., Jones C. D., Spall S. A., Totterdell I. J. *Acceleration of global warming due to carbon cycle feedbacks in a coupled climate model*, Nature 408, 184–187, November 2000
- [2] Cox P. M., Pearson D., Booth B.B., Friedlingstein P., Huntingford C., Jones C.D., Luke C.M. *Sensitivity of tropical carbon to climate change constrained by carbon dioxide variability*, Nature 494, 341–344, February 2013
- [3] ACEA 2016, *European automobile manufactures association: Consolidated registrations - by country*
- [4] ACEA 2016, *European automobile manufactures association: Alternative fuel vehicle registrations*
- [5] European Commission, *Communication from the Commission to the European Parliament, the Council, the European Economic and Social Committee and the Committee of the Regions: A European Strategy for Low-Emission Mobility*, UE regulation, July 2016
- [6] Fraser N., Blaxill H., Lumsden G., Bassett M., *Challenges for Increased Efficiency through Gasoline Engine Downsizing*, SAE Int. J. Engines 2(1):991-1008, 2009, <https://doi.org/10.4271/2009-01-1053>
- [7] Shahed S., Bauer K., *Parametric Studies of the Impact of Turbocharging on Gasoline Engine Downsizing*, SAE Int. J. Engines 2(1):1347-1358, January 2009, <https://doi.org/10.4271/2009-01-1472>
- [8] Hoag K., Primus R.J., *Turbocharging for Fuel Economy and Emissions*, web seminar, SAE International, February 2012
- [9] Anderson J.D., *Computational Fluid Dynamics, the basics with applications*, McGraw-Hill, ISBN-13: 978-0070016859, 1995.
- [10] Hill P.G, Peterson C., *Mechanics and thermodynamics of propulsion*, Reading, Mass., Addison-Wesley Pub. Co., 1965
- [11] Pavesi G., Cavazzini G., Santolin A., Ardizzon G., Lorenzi R., *Using splitter blades to improve suction performance of centrifugal impeller pumps*, Proceedings of the Institution of Mechanical Engineers, Part A, Journal of Power and Energy, 229. . 10.1177/0957650914563364, December 2014
- [12] Cumpsty N. A., *Compressor Aerodynamics*, New York: Wiley, 1989.
- [13] Kerres B., *On Stability and Surge in Turbocharger Compressors*, PhD thesis,

- KTH School of Industrial Engineering and Management (ITM), Machine Design (Dept.), Competence Center for Gas Exchange (CCGEx), 2017
- [14] Sundström E., *Flow instabilities in centrifugal compressors at low mass flow rate*, PhD thesis, Competence Center for Gas Exchange (CCGEx), KTH Mechanics, Royal Institute of Technology, December 2017
- [15] Dean R., Senoo Y., *Rotating wakes in vaneless diffusers*, Journal of Basic Engineering, 82(3):563–570, 1960
- [16] Gancedo M., Guillou E., Gutmark E., Mohamed A., *Dynamic Features and their Propagation in a Centrifugal Compressor Housing with Ported Shroud*, SAE Technical Paper, doi:10.4271/2012-01-0706, 2012
- [17] Semlitsch B., Jyothish K.V., Mihaescu M., Fuchs L. et al., *Numerical Flow Analysis of a Centrifugal Compressor with Ported and without Ported Shroud*, SAE Technical Paper, doi:10.4271/2014-01-1655, 2014
- [18] Johansson A.V., Wallin S., *An introduction to turbulence*, KTH Department of Mechanics, 2015
- [19] Menter F. R., *Two-Equation Eddy-Viscosity Turbulence Models for Engineering Applications*, AIAA Journal, vol. 32, no 8. pp. 1598-1605, 1994
- [20] Saadati E., *Introductory FLUENT Training, Chapter 6*, Sharif University of Technology, Ansys Inc, 2009. Available at: <http://slideplayer.com/slide/3872321/>
- [21] *Discretization of the Governing Equations*, Ansys CFX 18.1 documentation, paragraph 11.1.1.
- [22] *Numerical Errors*, Ansys CFX 18.1 documentation, paragraph 6.2.1.
- [23] Fisher F., *Application of Map Width Enhancement Devices to Turbocharger Compressor Stages*, SAE Technical Paper 880794, 1988, doi:10.4271/880794.
- [24] Xu C., Amano R.S., *Empirical Design Considerations for Industrial Centrifugal Compressors*, International Journal of Rotating Machinery, volume 2012, article ID 184061, doi:10.1155/2012/184061, April 2012
- [25] Dehner R., Selamat A., Steiger M., Miazgowicz K. et al., *The Effect of Ported Shroud Recirculating Casing Treatment on Turbocharger Centrifugal Compressor Acoustics*, SAE Int. J. Engines 10(4):2017, doi:10.4271/2017-01-1796.
- [26] *Measures of Mesh Quality*, Ansys CFX 18.1 documentation, paragraph 15.3.2.
- [27] Kuron M., *Criteria for Assessing CFD Convergence*, Engineering.com PLM/ERP articles, January 2015.
- [28] Mahaffy J., *Numerical Solutions Applied to Heat Transfer and Fluid Mechanics - Verification and Validation*, online resource, 2004, url: <http://www.personal.psu.edu/jhm/ME540/lectures/VandV/VandV.html>.
- [29] Roache P. J., *Verification of codes and calculations* AIAA journal, vol.36, no.5, pagg. 696 – 702, May 1998.
- [30] Celik I.B., Ghia U., Roache P.J., Freitas C.J., Coleman H., Raad P.E., *Procedure for Estimation and Reporting of Uncertainty Due to Discretization in CFD*

- Applications*, ASME Journal of Fluids Engineering, July 2008.
- [31] *Automatic Near-Wall Treatment for Omega-Based Models*, Ansys CFX 18.1 documentation, paragraph 4.2.3.
- [32] *Frame Change/Mixing Model*, Ansys CFX 18.1 documentation, paragraph 5.3.3.1.
- [33] Davy R., *Compressor Simulations for Turbo Applications*, Master's Degree Project, Scania CV AB, Linköping University, June 2016
- [34] Sundström E., Kerres B., Mihaescu M., *Evaluation of Centrifugal Compressor Performance Models using Large Eddy Simulation Data*, Competence Center for Gas Exchange (CCGEx), KTH Machine Design, ASME Technical paper, GT2016-57169, 2016
- [35] Sundström E., Semlitsch B., Mihaescu M., *Assessment of the 3D Flow in a Centrifugal compressor using Steady-State and Unsteady Flow Solvers*, Competence Center for Gas Exchange (CCGEx), KTH Machine Design, SAE Technical paper (2014-01-2856), 2014
- [36] Czitrom V., *One-Factor-at-a-Time Versus Designed Experiments*, The American Statistician, vol. 53, no. 2, May 1999
- [37] Jenkins B., *Latin hypercubes and all that: how DoE works*, Ora Research online resources, February 2015. Available at: <http://oraresearch.com/2015/02/latin-hypercubes-and-all-that/>
- [38] Cavazzuti M., *From Theory to Design Scientific and Technological Aspects in Mechanics*, chap. 2, *Design of Experiments*, Springer, ISBN 978-3-642-31187-1, 2013
- [39] *Flutter/Compressor surge*, TurboSmart.com online resource, 2017. Available at: <http://www.turbosmart.com/technical-articles/flutter-compressor-surge/>
- [40] Johansson P., *Evaluation surge behaviour of different compressor covers in vehicle, DU 650 hp*, Scania technical report, August 2017
- [41] Adams B.M., Ebeida M.S., Eldred M.S., Geraci G. *et al.*, *Dakota, A Multi-level Parallel Object-Oriented Framework for Design Optimization, Parameter Estimation, Uncertainty Quantification, and Sensitivity Analysis*, Version 6.7 User's Manual, SAND2014-4633, unlimited release, July 2014. Available at: <https://dakota.sandia.gov/content/manuals>
- [42] McDonald J.H., *Spearman rank correlation*, Handbook of Biological Statistics (3rd ed.), online resource available at: <http://www.biostathandbook.com/spearman.html>

Appendix A

Removal of the ported shroud cavity

In this appendix a qualitative study about the impact of ported shroud cavity on the HT compressor is described. The results of [subsection 5.2.1](#) are compared with those obtained on a modified CAD geometry where the ported shroud cavity is removed. A qualitative illustration is shown in [Figure A.1](#). The setup adopted is the same one described in [section 5.1](#): what changes is the mesh, whose dimensions are slightly reduced due to the removal of the ported shroud cavity.

Compressor map and efficiency curves for the two speed lines at 51100 rev/min and 90400 rev/min are shown in [Figure A.2](#). Removing the recirculation cavity drastically reduces the operating range of the compressor: the compressor map clearly highlights the performance decay at low and high mass flow rates, a result that can be translated into a shift surge and choke limits in the direction of the design conditions. On the other hand, at intermediate mass flows and near design conditions, an increase in performance is measured, both in terms of pressure ratio

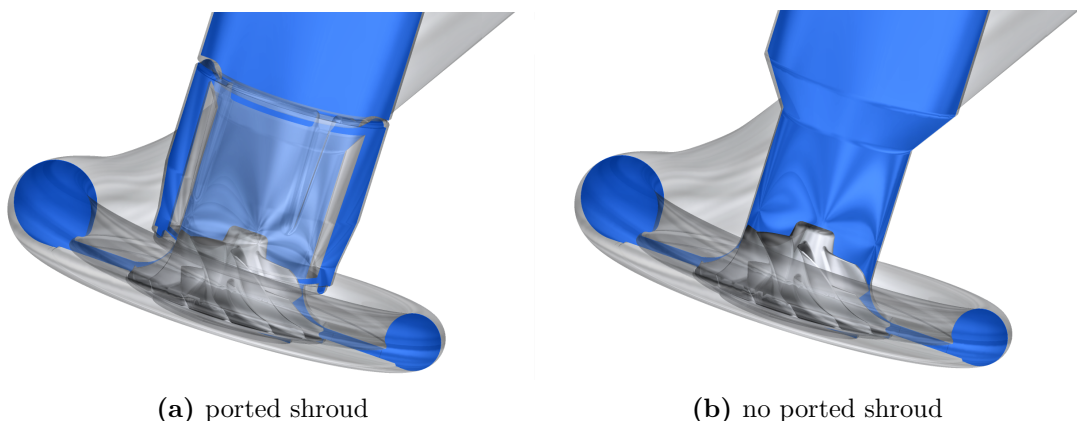


Figure A.1: Design with (a) and without (b) ported shroud.

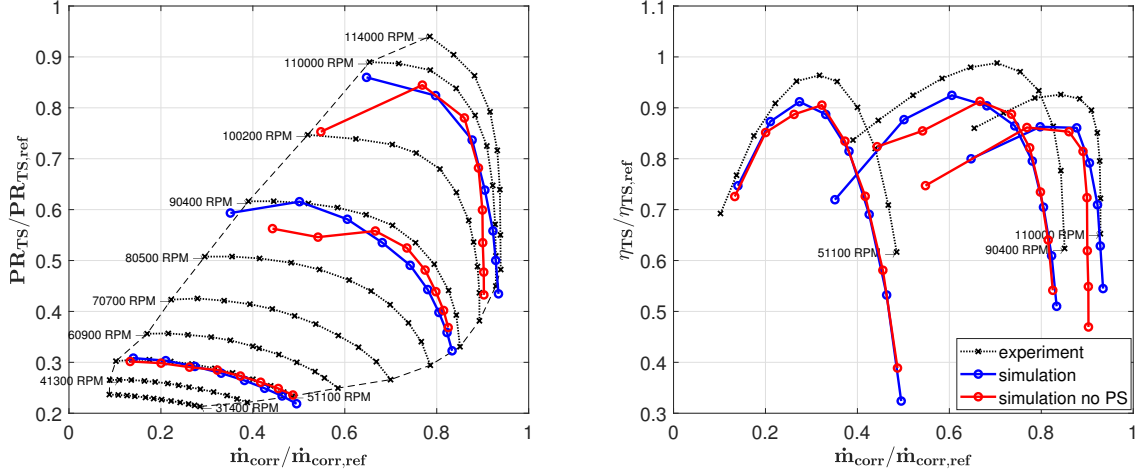


Figure A.2: Compressor map and total-to-static efficiency for two different speedlines. Results for the case without ported shroud are colored in red.

and efficiency (approximately 3%): the beneficial effect of the ported shroud is therefore slightly penalised at design conditions.

A.1 Flow visualizations

The ported shroud allows the ventilation of the low-momentum flow stuck on the blades at low mass flow conditions. A comparison between the cases with and without ported shroud is reported in [Figure A.3](#) in terms of velocity and temperature fields at off-design conditions.

The benefit brought by the ported shroud is immediately visible on the velocity fields: the reverse flow, instead of stagnating along the walls of the inlet pipe and obstructing the passage to the incoming flow, is ventilated in the cavity and reintroduced in the main flow. The flow over the blades is therefore more uniform, an effect which translates into higher efficiency at low mass flow rates.

Furthermore, the backflow is warmer because of the compression it has undergone; the temperature inside the cavity therefore increases as it reaches and exceeds the surge limit. In the absence of the recirculation cavity, hot flow is blocked near the tip of the blades, damaging them and compromising their performance.

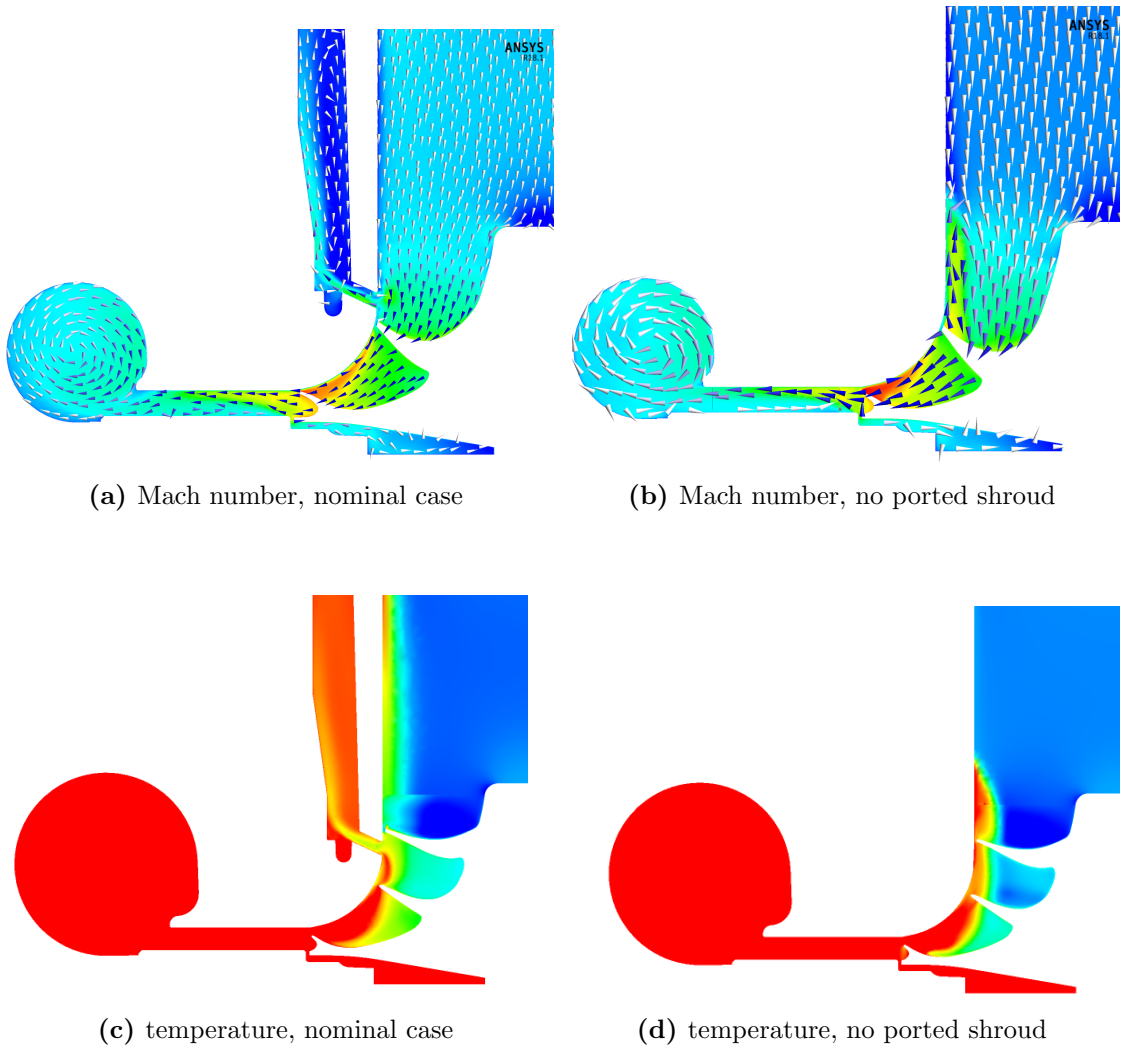


Figure A.3: Velocity and temperature field on the meridional plane at near surge conditions (90400 rev/min, 0,3 kg/s) for the cases with and without ported shroud.